

1 **Primary nasal viral infection rewires the tissue-scale memory response**

2 Samuel W. Kazer^{1,2,3,4*}, Colette Matysiak Match^{3,4*}, Erica M. Langan^{1,2}, Thomas J. LaSalle^{2,5},
3 Jessica Marbourg⁶, Katherine Naughton⁷, Elise O’Leary³, Ulrich H. von Andrian^{3,4,#}, Jose
4 Ordovas-Montanes^{1,2,4,8,9,#,^}

5 ¹Division of Gastroenterology, Hepatology, and Nutrition, Boston Children’s Hospital,
6 Boston, MA, USA;

7 ²Broad Institute of MIT and Harvard, Cambridge, MA, USA;

8 ³Department of Immunology, Harvard Medical School, Boston, MA, USA;

9 ⁴Ragon Institute of MGH, MIT and Harvard, Cambridge, MA, USA;

10 ⁵Program in Health Sciences and Technology, Harvard Medical School & Massachusetts
11 Institute of Technology, Boston, MA, USA;

12 ⁶AbbVie Cambridge Research Center, Cambridge, MA, USA;

13 ⁷AbbVie Genomics Research Center, North Chicago, IL, USA;

14 ⁸Program in Immunology, Harvard Medical School, Boston, MA 02115, USA;

15 ⁹Harvard Stem Cell Institute, Harvard University, Cambridge, MA, USA.
16

17 * These authors contributed equally to the work.

18 # These senior authors contributed equally to the work

19 ^ Lead contact

20 Correspondence to Jose Ordovas-Montanes; jose.ordovas-montanes@childrens.harvard.edu

21

22 **ABSTRACT**

23 The nasal mucosa is frequently the initial site of respiratory viral infection, replication, and
24 transmission. Recent work has started to clarify the independent responses of epithelial, myeloid,
25 and lymphoid cells to viral infection in the nasal mucosa, but their spatiotemporal coordination
26 and relative importance remain unclear. Furthermore, understanding whether and how primary
27 infection shapes tissue-scale memory responses to secondary challenge is critical for the rational
28 design of nasal-targeting therapeutics and vaccines. Here, we generated a single-cell RNA-
29 sequencing (scRNA-seq) atlas of the murine nasal mucosa sampling three distinct regions before
30 and during primary and secondary influenza infection. Primary infection was largely restricted to
31 respiratory mucosa and induced stepwise changes in cell type, subset, and state composition
32 over time. Interferon (IFN)-responsive neutrophils appeared 2 days post infection (dpi) and
33 preceded transient IFN-responsive/cycling epithelial cell responses 5 dpi, which coincided with
34 broader antiviral monocyte and NK cell accumulation. By 8 dpi, monocyte-derived macrophages
35 expressing *Cxcl9* and *Cxcl16* arose alongside effector cytotoxic CD8 and *Ifng*-expressing CD4 T
36 cells. Following viral clearance (14 dpi), rare, previously undescribed *Meg3+MHC-II+* epithelial
37 cells and **Krt13+ nasal immune-interacting floor epithelial (KNIIFE)** cells expressing multiple
38 genes with immune communication potential increased concurrently with tissue-resident memory
39 T (T_{RM})-like cells and IgG+/IgA+ plasma cells. Proportionality analysis coupled with cell-cell
40 communication inference underscored the CXCL16–CXCR6 signaling axis in effector CD8 T cell
41 and T_{RM} cell formation in the nasal mucosa. Secondary influenza challenge administered 60 dpi
42 induced an accelerated and coordinated myeloid and lymphoid response with reduced IFN-
43 responsive epithelial activity, illustrating how tissue-scale memory to natural infection engages
44 both myeloid and lymphoid cells without broad epithelial inflammation. Together, this atlas serves
45 as a reference for viral infection in the upper respiratory tract and highlights the efficacy of local
46 coordinated memory responses upon rechallenge.

47

48 **INTRODUCTION**

49 As the primary passage to the lower airway, the nasal mucosa balances the complex roles
50 of olfaction, filtration and conditioning of inhaled air, and host defense. To accomplish these
51 diverse functions, the nose contains distinct anatomical structures, harbors a varied yet organized
52 cellular composition, and secretes a multitude of proteins with distinct and complementary roles
53 (Harkema et al., 2006). In the face of pathogens, the nasal mucosa is thought to mount a variety
54 of incompletely understood defense mechanisms to protect against infection and limit spread to
55 the lower respiratory tract (Bosch et al., 2013). Nevertheless, many respiratory pathogens
56 manage to infect or colonize the upper airways and disseminate into the lungs, causing millions
57 of cases of severe disease, hospitalizations, and deaths annually (Clark, 2020; Roth et al., 2018;
58 Shinya et al., 2006).

59 There is a growing appreciation for how the inflammatory state of nasal tissue affects
60 respiratory viral infection outcome. The COVID-19 pandemic has helped accelerate research to
61 understand the roles of interferons (IFNs) in nasal protection and disease trajectory, with studies
62 highlighting the importance of sample timing and location, viral burden, and strain (Bastard et al.,
63 2022; Kim and Shin, 2021; Park and Iwasaki, 2020; Sposito et al., 2021). Study of the human
64 nasopharynx during SARS-CoV-2 infection showed muted IFN-response in epithelial cells from
65 individuals who went on to develop severe disease when compared with mild cases (Ziegler et
66 al., 2021). Expression of specific IFN stimulated genes (ISGs) like *OAS1* associate with protection
67 from severe COVID-19 and may even drive viral mutations to overcome host protection
68 (Wickenhagen et al., 2021). More generally, evidence of a recent prior infection in children
69 receiving a live-attenuated influenza vaccine was associated with enhanced ISG signaling and
70 lower viral shedding (Costa-Martins et al., 2021). Collectively, this suggests that the present nasal
71 state, cellular composition, and antiviral signaling capacity, as informed by the cumulative history
72 of environmental exposures, may drive disease outcomes (Bastard et al., 2020; Habibi et al.,
73 2020; Ordovas-Montanes et al., 2020; Weisberg et al., 2021; Zhang et al., 2020).

74 Following viral infection or intranasal (i.n.) vaccination, immune memory in the nasal
75 mucosa can provide long-term protection both systemically and at the mucosal barrier, reducing
76 pathology and infection burden in the lower airways and elsewhere (Johnson et al., 1986; Johnson
77 Jr. et al., 1985; Rutigliano et al., 2010). Local protection is afforded by both cellular and humoral
78 immune mechanisms. For example, CD8⁺ tissue-resident memory (T_{RM}) cells that form following
79 upper respiratory tract influenza A virus (IAV) infection correlate with enhanced protection against
80 heterologous IAV strain rechallenge (Pizzolla et al., 2017). Protective mucosal IgA producing
81 plasma cells, and antibodies capable of neutralizing virus, can be generated in the nasal mucosa

82 following IAV, vesicular stomatitis virus, respiratory syncytial virus, and SARS-CoV-2 infections
83 (Johnson Jr. et al., 1985; Liew et al., 2023; Sterlin et al., 2021; Wellford et al., 2022; Weltzin et
84 al., 1996). Even so, respiratory infections like IAV remain epidemic and kill up to 500,000 people
85 each year (Iuliano et al., 2018).

86 To develop protective, durable, and efficacious vaccines for respiratory viruses, we must
87 reach a deeper understanding of the establishment, timing, and cooperation of tissue-scale
88 memory following natural infection (Morens et al., 2023). Immune responses to pathogens often
89 occur in stepwise fashion: recognition of pathogen-associated molecular patterns by immune
90 and/or epithelial cells leads to cytokine production that broadly activates innate immune cells that
91 in turn recruit pathogen-specific effector lymphocytes, some of which will develop into circulating
92 and tissue-resident memory cells (Iwasaki and Medzhitov, 2015). Prior infection or vaccination,
93 however, has the capacity to re-order and even invert these circuits locally in the barrier tissues
94 that re-encounter infection (Kadoki et al., 2017; Kaufmann et al., 2018; Ols et al., 2020; Ordovas-
95 Montanes et al., 2020; Schenkel et al., 2014). During viral rechallenge, T_{RM} cells exhibit antiviral
96 effector functions and can act as sentinels that send antigen-specific inflammatory “alarms” to
97 local immune cells to activate multicellular anti-microbial responses at the site of infection (Ariotti
98 et al., 2014; McMaster et al., 2015; Schenkel et al., 2014; Steinbach et al., 2016). In mucosal
99 vaccination, $IFN-\gamma$ produced by antigen-specific T cells is sufficient to induce increased
100 inflammatory cytokine production by both distal (Bosch-Camós et al., 2022; Stary et al., 2015)
101 and local (Yao et al., 2018) antigen presenting cells, suggesting that recruited and/or tissue-
102 resident cells can contribute to rapid memory responses. Similarly, antibodies can directly
103 neutralize virus and also orchestrate a variety of antiviral effector functions through antibody Fc-
104 receptor mediated binding by NK cells, macrophages, and neutrophils (Boudreau and Alter,
105 2019). However, most of these studies to date have focused on the role of individual cell types or
106 limited interactions during a memory response.

107 Here, we present a tissue-scale single-cell RNA-sequencing (scRNA-seq) atlas of the
108 murine nasal mucosa before and during primary IAV infection and secondary rechallenge. By
109 sampling multiple regions, timepoints, and cell lineages, we develop a compositional landscape
110 of the tissue and reveal how the diversity of cell subsets and states dynamically changes in
111 response to infection and during a memory response. Primary IAV infection induced reproducible
112 stepwise shifts in cell composition starting with increased IFN-responsive neutrophil subsets
113 followed by broader antiviral/IFN-stimulated responses in epithelial, myeloid, and lymphoid
114 immune cells. Next, monocyte-derived macrophages (MDMs) accumulated along with effector
115 CD8 and CD4 T cells. Following viral resolution, T_{RM} cells and plasma cells are established

116 alongside increased frequencies of rare *Meg3+MHC-II+* epithelial cells and **Krt13+** nasal
117 immune-interacting floor epithelial (KNIIFE) cells expressing genes for several ligands and
118 receptors known to modulate immune cell activity. Learning cell cluster identity in samples
119 generated in memory and during IAV rechallenge, we demonstrate the applicability of our atlas to
120 inform newly generated data and show that the nasal memory response to IAV is accelerated and
121 coordinated compared to primary infection. Collectively, our spatial and temporal datasets
122 enumerate and characterize the diversity of cell types, states, and subsets in the murine nasal
123 mucosa and highlight those recruited and local cell subsets that exhibit memory and respond to
124 viral infection.

125

126 **RESULTS**

127 **Nasal mucosa infection with influenza virus and tissue processing**

128 We administered 10^4 plaque forming units (pfu) of IAV H1N1 strain PR8 i.n. to awake,
129 naïve mice in a small volume (5 μ l/nostril) to restrict infection to the upper respiratory tract
130 (Klinkhammer et al., 2018; Pizzolla et al., 2017), and collected and processed nasal mucosa
131 tissue (n=3 biological samples/timepoint) by scRNA-seq at 0, 2, 5, 8, and 14 days post infection
132 (dpi; “primary”). Later, additional samples were collected on 60 dpi and immediately following IAV
133 rechallenge with sample collection 2 and 5 days post rechallenge (dprc) during the memory
134 response (n=3/timepoint) (**Figure 1A**).

135 Anatomically, the murine nasal mucosa can be divided into several distinct morphological,
136 histological, and functional tissue regions (Harkema et al., 2006). We mapped the cellular and
137 structural diversity in the naïve nasal mucosa by immunofluorescence imaging, observing broad
138 heterogeneity in epithelial, immune, and neural distribution throughout the tissue (**Figure 1B**).
139 Thus, to capture region-specific changes in cell composition and response following IAV infection,
140 we micro-dissected the tissue and separated into three different regions: (1) respiratory mucosa
141 (RM), inclusive of the nasal and maxillary turbinates, septum, and vomeronasal organ; (2)
142 olfactory mucosa (OM), inclusive of the ethmoid turbinates; and (3) the lateral nasal gland (LNG),
143 which sits underneath the RM and OM in the maxillary sinus (see **Methods**).

144

145 **Single-cell spatiotemporal atlas of primary influenza infection in the nasal mucosa**

146 Across all primary infection timepoints, regions, and replicates (n=45), we collected
147 156,572 single-cell transcriptomes after filtering low-quality cell barcodes and hash-annotated cell
148 multiplets (**Methods**). Top-level clustering on the entire primary infection dataset captured dozens
149 of clusters belonging to neural, epithelial, immune, and stromal (endothelial, fibroblast, and

150 others) cell lineages demarcated by known lineage-restricted genes (**Figures 2A and S1A**). We
151 captured variable numbers of each cell type, with neurons and epithelial cells making up more
152 than half of the dataset (**Figure S1B**). Major cell types were found to be distributed differently
153 across nasal regions, with enrichment of neurons, granulocytes, B cells, and hematopoietic stem
154 cells (HSCs) in the OM and more epithelial cells, fibroblasts, myeloid cells, and T & NK cells in
155 the RM (**Figures 2B and S1C**). Since we collected bone (and thus bone marrow) along with the
156 mucosa, the relative enrichment of specific immune cell types — including HSCs and other
157 immune progenitors — in the OM can likely be attributed to cells localized to bone marrow (see
158 **Figure 1B**).

159 Sample replicates were called by demultiplexing oligo-hashtag count tables (Li et al.,
160 2020) and did not exhibit strong batch effects (**Figure S1D**). While clustering and differential
161 expression were performed on all singlets regardless of successful hash assignment, we counted
162 only those cells with annotated sample replicates for downstream compositional analyses.

163 To delineate the diversity of cell subsets and states present in the nasal mucosa, we split
164 the dataset by cell type and conducted new clustering analyses, yielding 9-to-28 subclusters per
165 cell type for a total of 127 clusters across the dataset (**Figure S1F and Supplementary Table 1**).
166 By counting the number of cells assigned to each cluster in each sample replicate and normalizing
167 across samples, we calculated cell cluster abundances to interrogate the relationship between
168 samples in cell compositional space (see **Methods**). Performing principal component analysis
169 (PCA) on samples over cell cluster abundances, we saw strong separation by region (**Figure 2C**),
170 reinforcing that the nasal mucosa contains distinct regions with specific functions. Examination of
171 the PCA loadings revealed that LNG is defined by higher abundances of odorant binding protein
172 (OBP)-expressing cells, serous cells, and capillary endothelial cells (**Figure S1G**). OM has
173 relatively more Schwann cells, sustentacular cells (Brann et al., 2020), and olfactory sensory
174 neurons, while RM is enriched for vomeronasal sensory neurons, chondrocytes, and resting basal
175 cells. Collectively, this atlas represents a high-resolution, comprehensive view of the mouse nasal
176 mucosa enabling characterization of the dynamic differences in cellular composition within and
177 between nasal regions during infection.

178
179 **Influenza infection is largely restricted to the RM and induces reproducible changes in**
180 **cellular composition**

181 While viral, immune cell, and epithelial cell dynamics following IAV infection of the lung
182 have been partially mapped (Bouvier and Lowen, 2010; Boyd et al., 2020; Manicassamy et al.,
183 2010; Matsuoka et al., 2009; Steuerman et al., 2018), responses in the nasal mucosa are less

184 studied. Viral titers of entire nasal mucosa showed robust infection 2 dpi that waned through 8 dpi
185 and was completely cleared by 14 dpi (**Figure 2D**), while data from lungs showed sporadic spread
186 of virus from the nasal mucosa only occurring between 5 and 8 dpi (**Figure S2A**). Aligning to a
187 joint IAV and mouse genome, we also captured viral transcripts by scRNA-seq and thus could
188 identify which cells may have been infected or contained virus. Individual genes like NP and HA
189 were detected most strongly in epithelial and myeloid cells (**Figure S2B**). We calculated a
190 summative IAV unique molecular identifier (UMI) count for every single cell to assess “positivity”
191 for IAV (**Figure 2E**). Infected cells producing large amounts of virus may not survive tissue
192 dissociation and processing, leading to lower-than-expected numbers of IAV+ cells. Looking
193 across time points and regions in epithelial and myeloid cells, we captured low, but reproducible
194 numbers of IAV+ cells 2, 5, and 8 dpi in the RM, but no positive cells in the OM, and only at 5 dpi
195 in the LNG (**Figures S2C-D**).

196 Staining for IAV NS2 and 5 dpi confirmed that infection was largely restricted to epithelial
197 cells in the RM (**Figures 2F and S2E**) and is consistent with expression of binding receptors
198 marked by α 2,3-linked sialic acid in mucous producing cells (Ibricevic et al., 2006). We performed
199 qPCR of total RM to validate an early response to infection and found robust upregulation of type
200 I and III IFNs 2 dpi, with even higher expression 5 dpi despite relatively lower viral titers (**Figure**
201 **S2G**). As expected, *Ifng* expression exhibited delayed kinetics peaking 8 dpi.

202 To understand how infection remodels each nasal region, we applied PCA to the sample
203 replicates within each region. In OM, 5 and 14 dpi samples separated from each other and the
204 other time points (**Figure S2H**). In LNG, only 14 dpi samples separated from the rest (**Figure**
205 **S2I**). Comparatively, PCA of RM samples showed clear separation between all timepoints in
206 chronological order across the first two PCs (**Figure 2G**) suggesting dynamic and linked
207 responses occur over the course of infection in this region. PCA loadings from RM highlight a shift
208 in composition from resting basal cells, fibroblasts, and ciliated cells in naïve mice and 2 dpi to
209 diverse activated myeloid and lymphoid clusters 5 and 8 dpi that gave way to specific
210 goblet/secretory cells, T_{RM}-like cells, and mature myeloid cells following viral resolution 14 dpi
211 (**Figure 2H**). Even though virus had been cleared by 14 dpi, we note that all three nasal regions
212 reached compositions distinct from naïve mice at this timepoint.

213

214 **Cataloging the epithelial subsets and states present in the murine nasal mucosa at**
215 **baseline and throughout infection**

216 *Cellular diversity of the nasal epithelium*

217 Having acquired high-level knowledge of how IAV infection broadly impacts the nasal
218 mucosa, we next sought to understand the variety of epithelial cells present across the tissue and
219 how they respond during infection as the main target of infection. Subclustering on all epithelial
220 cells yielded 28 clusters encompassing diverse differentiation states and functions (**Figures 3A**
221 **and S3A**). We categorized these clusters into broader subsets including basal (*Krt5*, *Krt14*),
222 ciliated (*Foxj1*, *Dnah5*), serous (*Ltf*, *Ccl9*), glandular (*Bpifb9b*, *Odam*), goblet/secretory (*Reg3g*,
223 *Selenom*, *Scgb1c1*, and mucin-encoding genes), ionocyte (*Cftr*, *Coch*), tuft (*Trpm5*, *Il25*), and
224 sustentacular cells (*Sec14l3*, *Cyp2g1*) (**Figure 3B**). In addition to known subsets, we also
225 identified unique clusters of epithelial cells potentially specific to the nasal mucosa and present in
226 naïve mice and throughout primary infection that separated distinctly in UMAP space: *Scgb-*
227 *b27+Cck+*, *Klk1+Fxyd2+*, *Meg3+MHC-II+*, and *Krt13+Il1a+* cells. Epithelial clusters were
228 differentially distributed across regions (**Figure 3C**): recently described nasal tuft cells, ionocytes,
229 and *Dclk1+* cells (Ualiyeva et al., 2022), as well as olfactory sensory neuron supportive
230 sustentacular cells (Brann et al., 2020), were enriched in OM, whereas serous and glandular cells
231 were specific to LNG.

232

233 *Cycling and IFN-responsive epithelial cells arise in the RM during infection*

234 To understand the impact of IAV infection on the nasal epithelial compartment, we first
235 determined which clusters harbored viral reads. Looking at the distribution of IAV UMIs across all
236 epithelial clusters, we found that IAV+ cells were most prevalent in the IFN-stimulated cluster
237 followed by cycling basal and ciliated cells (**Figure S3B**). The IFN-stimulated cluster, largely
238 restricted to the RM, exhibited high levels of *Krt5*, a basal cell marker, but also *Cxcl17*, which in
239 our dataset is expressed at steady state in serous cells in the LNG and some goblet/secretory
240 subsets. While infection was well-established at 2 dpi, we were surprised to see that IFN-
241 stimulated epithelial cells only arose starting at 5 dpi and made up ~20% of all RM epithelial cells
242 5 and 8 dpi (**Figure 3D**). We cannot rule out that the lack of IFN-responsive cells 2 dpi may have
243 been from loss of infected cells during processing, but host silencing mechanisms by IAV itself
244 may have contributed as well (Kochs et al., 2007). Comparing cells within the IFN-stimulated
245 cluster by presence of IAV transcripts, we found relatively higher levels of ISGs but lower
246 expression of transcription factors *Atf3*, *Egr1*, and *Junb* in IAV+ cells (**Figure S3C**), suggesting
247 dysregulation of epithelial cell state.

248 Cycling basal cells demonstrated a similar transient increase in abundance, peaking 5 dpi
249 (**Figure 3E**). Interestingly, differential expression across timepoints revealed many ISGs were
250 upregulated in these cells 5 dpi (**Figure S3D**). Given recent work demonstrating that the epithelial

251 IFN-response can impede proliferation and tissue repair in the lower airway (Broggi et al., 2020;
252 Major et al., 2020), we leveraged our single-cell resolution to assess if individual nasal basal cells
253 co-express pathways for cell cycle and IFN-response. Gene set analysis confirmed significant
254 enrichment for both cell cycle and IFN-response pathways in cycling basal cells. Additionally, a
255 largely mutually exclusive apoptosis pathway was also significant (**Figures S3E-F**). Pathway
256 module scoring showed that while the IFN α response score changed over time, the G2M
257 Checkpoint score was equally distributed across time points and independent of IFN α response
258 (**Figure 3F**). Thus, unlike their lower respiratory tract counterparts, nasal cycling basal cells
259 proliferate during primary infection and may concurrently support ISG expression alongside non-
260 proliferative IFN-stimulated basal cells.

261
262 *Rare unique epithelial cell subsets with lymphoid and myeloid communication potential*
263 *accumulate following viral clearance*

264 Looking at the compositional PCA, RM samples from 14 dpi separated from other
265 timepoints (**Figure 2F**). Among epithelial cells, two clusters, *Emp1+Ccdc3+* basal cells and
266 *Gp2+Lyz2+* goblet/secretory cells, accumulated to 9-12% of all epithelial cells following viral
267 clearance by 14 dpi (**Figure S3G**). In addition to *Gp2* and *Lyz2*, the goblet/secretory subset was
268 also enriched for *Il33*, *Muc1*, *Isg20*, and *Cd14* suggesting a potential shift in the epithelium toward
269 an antibacterial state. Additionally, two rare and transcriptionally distinct subsets of epithelial cells
270 (*Meg3+MHC-II+* and *Krt13+Il1a+*), each only making up ~1% of all RM epithelial cells prior to viral
271 clearance, accumulated at 14 dpi ($p=0.032$ and $p=0.067$, respectively). The *Meg3+MHC-II+*
272 subset expressed high levels of maternally imprinted Meg genes (*Meg3*, *Rian*) alongside *Cd74*,
273 H2 class II genes, *Wnt5a*, *Cxcl12*, and *Ccl25* (**Figure 3G**). They also uniquely expressed *Fezf2*,
274 a transcription factor studied in the context of thymic self-antigen expression and immune
275 tolerance induction by thymic epithelial cells (Takaba et al., 2015), but not *Aire*, which is necessary
276 in the thymus for presentation of autoantigens. Whether these cells can promote tolerance in the
277 upper respiratory tract, similar to their thymic counterparts, remains to be determined.

278 The *Krt13+Il1a+* subset uniquely expressed *Krt13* (93.8% expressing within cluster vs
279 0.6% expressing in other clusters), a keratin previously described on “hillock” cells in the trachea
280 with undetermined functions (Montoro et al., 2018). These nasal cells exhibited several of the
281 markers specific to tracheal hillock cells including *Lgals3*, *Ecm1*, and *Anxa1* but were not enriched
282 for *Cldn3* or club cell marker *Scgb1a1*. Unlike hillock cells, this nasal subset expressed genes for
283 several secreted and membrane bound immune cell regulatory factors including *Il1a*, *Tnf*, *Cd274*
284 (PD-L1), *Ifngr2*, and *Cxcl16* as well as secretory proteins like *Defb1*, *Muc4*, and *Muc1* (**Figure**

285 **3H**). Given the potential for these *Krt13*⁺ cells to communicate with immune cells, we stained the
286 mucosa for Krt13 to understand their distribution throughout the nasal cavity. We found the
287 strongest signal for Krt13 along the nasal floor in the anterior RM (**Figure 3I**) and more distally
288 where the nasal mucosa meets the oral mucosa (**Figure S3H**). Comparing samples from naïve
289 mice and 14 dpi, we saw increased Krt13 staining and colocalization with PD-L1 in the post-
290 infection samples (**Figure 3J**). Thus, following resolution of IAV infection, rare subsets of nasal
291 epithelial cells with immune communication potential accumulate in the RM.

292

293 **Neutrophils mature and activate in the RM immediately following IAV infection**

294 Neutrophil accumulation in IAV infected lung has largely been associated with severe
295 disease and poor prognosis (Brandes et al., 2013; Johansson and Kirsebom, 2021; Tang et al.,
296 2019), but their role in the nasal viral infection is unknown. Given recent work showing a
297 relationship between neutrophil activation in the nose prior to RSV infection and symptom
298 occurrence (Habibi et al., 2020), and intrigued by the large number of neutrophils and mast cells
299 captured across the nasal mucosa (n=7,987), we investigated the transcriptional programs and
300 change in frequency of granulocytes in the nasal mucosa. Subclustering and UMAP embedding
301 revealed a continuum of granulocyte development starting with granulocyte-myeloid precursor
302 like cells (*Elane*, *Mpo*), differentiating through immature states (*Camp*, *Mmp8*, *Retnlg*), and ending
303 with several clusters of mature neutrophils (*Il1b*, *H2-D1*, *Siglecf*) (**Figures 4A and S4A**). Mast
304 cells expressing *Il6*, *Gata2*, and *Il4* were also detected in small numbers. Most neutrophils
305 originated from OM samples (**Figures 2C and S4B**) and are likely present in high numbers in the
306 bone marrow. Pseudotime analysis across both the OM and RM recapitulated known maturation
307 gene expression patterns in the blood (Grieshaber-Bouyer et al., 2021) and systemically (Xie et
308 al., 2020) (**Figures 4B and S4C**), suggesting that precursors and immature neutrophils in OM
309 bone marrow may give rise to activated and mature subsets in the RM.

310 By 2 dpi, neutrophil composition in the RM transitioned into mature IFN-stimulated and
311 MHC-I-Hi states alongside an antimicrobial immature subset near the end of the pseudotime
312 development trajectory (**Figure 4C**). The accumulation of these neutrophil clusters is one of the
313 earliest changes in the RM following infection and may make up some of the earliest responses
314 to local IFN, with epithelial IFN-Stim responses in either infected or uninfected cells not arising
315 until 5 dpi. Interestingly, the OM exhibited increased frequencies of mast cells, progenitors, and
316 cycling immature granulocytes in 2-of-3 mice at 5 dpi, likely within bone marrow, indicating IAV
317 infection may induce changes to nearby hematopoiesis (**Figure S4D**). Thus, neutrophil activation

318 and maturation mark the earliest detectable responses using our sampling strategy in the nasal
319 mucosa to IAV infection.

320

321 **Recruited monocytes and monocyte-derived macrophages constitute the myeloid effector** 322 **response to IAV**

323 Next, we explored heterogeneity among non-granulocyte myeloid cells (**Figure 4D and**
324 **S5A**) — i.e., macrophages, monocytes, and dendritic cells (DCs). We captured a spectrum of
325 macrophage (*Cd74*, *C1qb*, *Ccl4*) clusters including a putative tissue-repair subset expressing
326 *Trem2*, *Fcrls*, and *Il1a*, an innate immune recruiting subset expressing *Ccl7*, *Ccl8*, and *Pf4*
327 (CXCL4), and a small cluster of osteoclasts (*Ctsk*, *Mmp9*). Monocytes clustered into classical
328 (*Ly6c2*, *Ccr2*, *Chil3*) and non-classical (*Ace*, *Ear2*, *Itgal*) subsets (Jung et al., 2022) alongside
329 IFN-stimulated monocytes and monocyte-derived macrophages (MDMs). DCs separated into
330 distinct clusters including Langerhans-like (*Epcam*, *Ccl17*, *Ccl22*), intraepithelial (*Cd103*, *Xcr1*,
331 *Tlr3*), migratory (*Ccr7*, *Ccl22*, *Cd274*), and a subset uniquely expressing *Cd209a* (DC-SIGN),
332 *Tnfsf9* (4-1BB), and *Klrd1*. We also captured plasmacytoid DCs (*Siglech*, *Irf8*; pDCs). Most
333 myeloid clusters were present in all nasal regions with some exceptions like the IFN-stimulated
334 monocytes and MDMs, which were restricted to the RM (**Figure S5B**).

335 While non-existent at baseline, upward of 30-40% of all myeloid cells belonged to these
336 antiviral monocyte and MDM clusters 5 and 8 dpi, respectively (**Figure 4E**). The appearance and
337 accumulation of monocytes and MDMs is concordant with lower frequencies of several tissue
338 macrophage clusters, likely reflecting an overall increase in the total number of myeloid cells in
339 the tissue as monocytes infiltrate from circulation. To understand the difference between the IFN-
340 stimulated monocytes and MDMs, we performed differential expression analysis between clusters
341 (**Figure 4F**). While the monocyte cluster had higher ISG expression than the MDM cluster, the
342 MDMs still had relatively high ISG expression when compared with resting tissue macrophages.
343 Notably, IFN-stimulated MDMs expressed higher levels of *Cxcl9* and *Cxcl16*, whose receptors
344 (CXCR3 and CXCR6, respectively) have been implicated in T_{RM} cell development in the lung
345 (Slütter et al., 2013; Wein et al., 2019). This cluster also had the largest number of IAV+ cells of
346 all myeloid cells (**Figure S5C**). Bystander analysis showed higher ISG expression in IAV+ myeloid
347 cells, like IAV+ epithelial cells (**Figure S5D**). However, IAV+ MDMs also had lower expression of
348 MHC-II genes and inflammatory cytokine genes *Ccl6* and *Cxcl9* suggesting reduced antigen
349 presentation and inflammatory signaling capacity, consistent with prior research in the lung
350 showing IAV suppresses myeloid cell activation and maturation (Moriyama et al., 2016; Zhang et
351 al., 2022a).

352 The rapid shift in the myeloid compartment from IFN-stimulated monocytes at 5 dpi to a
353 predominance of IFN-stimulated MDMs 3 days later (**Figure 4E**) suggested that recruited
354 monocytes differentiated into MDMs within the RM during this interval. To test this idea, we treated
355 mice daily with an anti-CCR2 antibody (Mack et al., 2001) to deplete circulating monocytes from
356 3 to 5 dpi (**Figure S5E**). We stained for differentiating monocytes in the nasal mucosa by flow
357 cytometry using MHC-II, CD11c, F4/80, CD64, and an intravascular CD45 stain to separate cells
358 that had extravasated into the tissue from those in circulation (**Figure S5F**). Ly6C⁺ and Ly6C⁺⁺
359 cells represent recently recruited monocytes with and without patrolling function; expression of
360 MHC-II, in addition to F4/80 and CD64, by monocytes reflects differentiation into MDMs.
361 Treatment with anti-CCR2 antibody reduced frequencies of Ly6C⁺ monocytes overall. Moreover,
362 the proportion and number of differentiated Ly6C⁺⁺ and Ly6C⁺ cells (i.e., MDMs) were
363 considerably lower, suggesting monocytes recruited after 7 dpi had not yet differentiated (**Figures**
364 **4G and S5G**). Together, these data show that IAV infection induces a large recruitment of antiviral
365 monocytes 5 dpi that differentiate into MDMs by 8 dpi in the RM.

366

367 **Antiviral NK cell responses precede transient effector T cells that are replaced by durable** 368 **T_{RM} cells following viral clearance**

369 Following the accumulation of inflammatory and chemokine secreting monocytes and
370 MDMs at 5 and 8 dpi, we anticipated a strong lymphocyte response during IAV infection. Thus,
371 we next further investigated NK and T cells, the latter of which have been shown to be essential
372 in clearing IAV infection in the lungs (Hufford et al., 2015) and nasal mucosa (Pizzolla et al., 2017).
373 Subclustering revealed NK cell subsets (*Klrb1c*, *Ncr1*), type 2 (*Areg*, *Il13*) and type 3 (*Il22*, *Rorc*)
374 innate lymphoid cells (ILC), $\gamma\delta$ T cells (*Trdc*, *Cd163l1*), and a spectrum of $\alpha\beta$ T cell subsets and
375 states including naïve/central memory CD8 (*Ccr7*, *Dapl1*), effector CD8 (*Gzmb*, *Gzmk*), T_{RM}-like
376 CD8 cells (*Itgae* [CD103]), resting CD4 (*Cd4*, *Tnfrsf4* [OX40]), Th1 CD4 (*Ifng*, *Cd200*), Th17
377 (*Cd40lg*, *Il17a*), and a cluster of Helios (*Ikzf2*) expressing cells (**Figures 5A and S6A**). Most T
378 and NK cell clusters were enriched or restricted to the RM, but *Ccr7*⁺ CD8 T cells, ILCs, and $\gamma\delta$ T
379 cells were also found in the OM and LNG (**Figure S6B**).

380 Looking at T and NK cell frequencies, we found that IFN-stimulated T and NK cells
381 accumulated 5 dpi alongside cytotoxic NK cells that remained elevated through 8 dpi (**Figure**
382 **S6C**). By 8 dpi, the T and NK cell compartment completely shifted towards effector antiviral T cell
383 subsets, with high abundances of *Gzmk*⁺ CD8, Th1-like *Ifng*⁺*Cd200*⁺ CD4, cycling, and Helios⁺
384 T cell clusters (**Figure 5B**). These effector responses were short-lived, however, and were
385 followed by increased frequencies of T_{RM} cells and resting CD4 T cells (**Figure 5C**). Notably, while

386 detectable infection was largely restricted to the RM, T_{RM} cells also increased in OM and LNG 14
387 dpi (**Figure S6D**), supporting the notion that even low levels of infection can result in T_{RM}
388 accumulation and development (Jiang et al., 2012).

389 To contextualize the T_{RM}-like cells that arise following IAV clearance, we examined two
390 recently published signatures separating resident memory from central/circulating memory. A
391 universal T_{RM} gene score (Milner et al., 2017) reasonably separated our T_{RM} cluster from effector
392 and naïve/memory CD8 T cells, but IFN-stimulated T cells also scored highly (**Figure 5D**).
393 Conversely, the T_{RM}-like cells also scored low for the associated circulating memory gene score,
394 while naïve/memory CD8 T cells scored highest (**Figure S6E**). Closer inspection of known
395 resident memory and central memory markers and transcription factors (Crowl et al., 2022)
396 confirmed restriction of *CD103* (*Itgae*) expression to our T_{RM} cluster, but *Cd69* was only highly
397 expressed in IFN-stimulated cells. *Runx3* was also most highly expressed in T_{RM}-like cells but
398 also at lower levels in effector CD8 T cells. The *Cd103*⁺ CD8 cluster lacked the known
399 naïve/central memory transcription factors *Klf2* and *Tcf7* (**Figure 5E**). In summary, effector T cell
400 responses in the RM 8 dpi are replaced by T_{RM}-like cells across all nasal mucosa regions following
401 viral clearance.

402

403 **Plasma cells populate throughout the NM following viral clearance**

404 Following IAV infection, local mucosal plasma cells and activated B cells produce and
405 secrete neutralizing soluble IgA into the airways (Rossen et al., 1970; Wellford et al., 2022; Woof
406 and Mestecky, 2005). In the lungs, resident memory B cells form after primary infection and can
407 be recruited upon secondary challenge to produce additional antibodies (MacLean et al., 2022),
408 suggesting infection can lead to long term changes in both local and distal B cell subsets.
409 Clustering of B cells in the nasal mucosa (**Figures S7A-B**) revealed mature subsets (*Ighd*, *Cd74*),
410 plasma cells (*Mki67*, *Ighg2b*, *Igha*), lambda-chain-high expressing cells (*Iglc1*, *Iglc2*), nucleoside
411 diphosphate kinase (NME) expressing cells (*Nme1*, *Nme2*) and, primarily in OM, developing
412 subsets including pro-B (*Dntt*, *Vpreb1*, *Rag1*), pre-B (*Bub1b*, *Mki67*, *Sox4*), and immature B cells
413 (*Ms4a1*, *Irf30*). The preponderance of precursor and developing B cell subsets in OM likely reflects
414 bone marrow cells, whereas IgG⁺/IgA⁺ plasma cells were found at highest frequency within LNG
415 tissue, but class-switched B cells were also detectable in RM and OM (**Figure S7C**).

416 Looking at changes in cluster frequency over the course of IAV infection, we found that
417 pro-B and pre-B cells collectively comprised up to 80-90% of all B cells in the OM 5 dpi increasing
418 from 5-15% at baseline, suggesting that IAV infection may induce local B cell proliferation and
419 differentiation in the bone marrow following infection and/or egress of mature B cells from this

420 region (**Figure S7D**). This increase in B cell precursor frequency in OM 5 dpi paralleled that of
421 granulocyte precursors (**Figure S4D**), supporting the notion of the activation of nasal bone
422 marrow. By 14 dpi, IgG+/IgA+ plasma cells were reliably detected in the RM in all three replicate
423 samples. However, plasma cell recovery was more variable in OM and LNG samples, which could
424 be due to biological variability and/or inconsistent cell capture. Indeed, imaging of the RM and
425 LNG at 30 dpi confirmed increased IgA+ cells in both regions when compared with naïve mice,
426 with the largest number of IgA-expressing cells localizing to the LNG (**Figure S7E**). Thus, B cells
427 may undergo proliferative development during acute IAV infection and plasma cells accumulate
428 in the RM and LNG following clearance.

429 430 **Proportionality guided cell-cell communication analysis highlights the CXCL16-CXCR6** 431 **signaling axis in effector and memory T cell responses**

432 To understand how compositional changes in the tissue during primary infection may be
433 coordinated across multiple cell subsets, we next characterized relationships between pairs of
434 cell clusters over time using our compositional data. We employed proportionality analysis (Lovell
435 et al., 2015), an alternative to correlation that avoids intra-sample abundance dependence
436 present in compositional data (Quinn et al., 2018), to find cell clusters with significantly similar
437 abundance trajectories (see **Methods**). Given that the RM was the major site of infection and
438 showed temporally structured changes in cell composition over time (**Figure 2G and H**), we
439 applied our proportionality analysis to all samples from this region. We discovered a highly
440 structured proportionality landscape with 101 significantly proportional cluster pairs (FDR < 0.05)
441 (**Figures 6A and S8A**). To understand coordination among larger groups of cell clusters, we built
442 a network of all significantly proportional cluster pairs (**Figure S8B**). The network revealed larger
443 groups of proportional responses made up of clusters from several different cell types and smaller
444 and single-pair groups with 1-2 contributing cell types. Next, to further characterize the
445 coordination among immune cells and between immune and epithelial cells, we investigated
446 subsets of clusters with high proportionalities by cell-cell communication analysis.

447 448 *IFN-stimulated MDMs – Gzmk+ CD8 T cells – Ifng+ Cd200+ CD4 T cells*

449 The strongest proportionality was observed among highly networked IFN-stimulated
450 clusters and effector T cell clusters (**Figure 6B**). Given the strong myeloid and T cell responses
451 8 dpi and the possibility that activated MDMs may function as APCs within the nasal mucosa, we
452 focused on the relationship between the IFN-stimulated MDM, *Gzmk+* CD8 T cell, and
453 *Ifng+ Cd200+* CD4 T cell clusters. Plotting abundance values confirmed overlapping trajectories

454 of these three clusters with transient accumulation starting 5 dpi, peaking at 8 dpi, and waning by
455 14 dpi (**Figure 6C**). We next assessed cell-cell communication potential using NICHES, an
456 approach that finds single-cell pairs with multiplicative high expression of known interacting
457 ligands and receptors (Raredon et al., 2023). Differential ligand-receptor expression between
458 groups of cell-pairs was then used to identify interactions specific to pairs of clusters (see
459 **Methods and Supplementary Table 2**). Applied to cells from these three clusters at 8 dpi, we
460 found several predicted interactions between the MDM cluster and both effector T cell clusters
461 including *Cd274–Pdc1* (PD-L1–PD-1), *Cd86–Ctla4*, and *Cxcl16–Cxcr6* (**Figure 6D**).

462

463 *Cd103+ DCs – Dusp2+Icam1+ mature neutrophils – Gp2+Lyz2+ goblet/secretory cells*

464 The second largest networked group included various myeloid, granulocyte, and epithelial
465 cell clusters. Intrigued by the inclusion of the late arising Gp2+Lyz2+ goblet/secretory cell cluster
466 (**Figure S3G**), we took a closer look at this cluster and the two clusters most proportional with it:
467 *Cd103+* DCs and *Dusp2+Icam1+* mature neutrophils. Plotting cluster abundances confirmed that
468 all three clusters peaked following viral clearance 14 dpi (**Figure S8C**). Closer inspection of
469 differentially expressed ligand-receptor pairs revealed potential pro-inflammatory signaling by
470 Gp2+Lyz2+ Gob/Sec cells to mature neutrophils via *Sftpd–Sirpa*, which blocks Cd47 binding
471 (Gardai et al., 2003), *Cirbp–Trem1* which has been shown to occur in sepsis (Denning et al.,
472 2020), and *Tgfb2–Tgfb1*. DC–neutrophil interactions included *Ccl2–Ccr1* and *Il18–Il18rap*
473 suggesting mutual immune recruitment/homeostasis (**Figure S8D**). These interactions suggest
474 that late arising Gp2+Lyz2+ goblet/secretory cells may recruit and regulate *Cd103+* DCs and
475 mature neutrophils in the RM following viral clearance.

476

477 *Krt13+Il1a+ epithelial cells express Cxcl16 and increase when T_{RM}-like cells accumulate*

478 Like IFN-stim MDMs producing *Cxcl16* 8 dpi in concert with abundant *Cxcr6* expressing
479 effector CD8 and CD4 T cells, the late arising *Krt13+Il1a+* epithelial cell subset expressed *Cxcl16*
480 alongside increasing frequencies of *Cxcr6+* T_{RM} and CD4 T cells 14 dpi (**Figures 6E-F**). Although
481 not significantly proportional over all time points ($\rho = 0.53, 0.32, 0.77$), we applied cell-cell
482 communication analysis to cells from 14 dpi in these three clusters given the role of CXCL16–
483 CXCR6 signaling in T_{RM} localization in the lower airways (Morgan et al., 2008; Wein et al., 2019).
484 In addition to discovering the *Cxcl16–Cxcr6* interaction, the analysis also captured additional
485 interactions like *Cd274–Pdc1*, *Timp2–Itgb1*, *Il18–Cd48*, *Alcam–Cd6*, and *Il16–Cd9* (**Figure 6G**).
486 RNAscope of the nasal floor 14 dpi confirmed expression of *Cd274* (PD-L1) and *Cxcl16* by *Krt13+*
487 cells in the vicinity of cells expressing *Cxcr6* (**Figures S8E and 6H**). Considering the

488 transcriptional programming and localization of these cells, we propose the name ***Krt13+*** nasal
489 immune-interacting floor epithelial (KNIIFE) cells. Notably, KNIIFE cells are a fraction of many
490 cells on the nasal floor expressing *Cxcl16* at 14 dpi, suggesting that this region of the nasal
491 mucosa may be important in instructing T_{RM} cells following viral clearance and/or tissue damage.

492 In summary, proportionality analysis coupled with cell-cell communication approaches
493 reveal temporally synced cell cluster abundance changes over the course of primary infection and
494 highlight potential cell-cell interactions contributing to T cell function and residual inflammation
495 following viral clearance.

496

497 **Learning the cellular composition of new scRNA-seq datasets of the nasal mucosa**

498 To assess the ability of our primary IAV infection atlas to contextualize and analyze new
499 scRNA-seq data generated from murine nasal mucosa, we utilized the replicate structure of our
500 dataset to test label transfer methods. Separating one RM replicate from each timepoint as a
501 query set, we compared Seurat's built-in weighted nearest neighbors method (Hao et al., 2021)
502 to the generative model approach used in single-cell Annotation using Variational Inference
503 (scANVI) (Xu et al., 2021). First trying cluster annotation on the entire RM query dataset, we found
504 poor accuracy in assigning correct cluster identity in both methods and several clusters were
505 completely lost in the predicted annotations (**Figure S9A**). Since the primary infection atlas
506 clusters were found following multiple rounds of clustering, we next applied the same stepwise
507 approach for label transfer: assign a cell type label and then split into cell types for cluster label
508 predictions (**Figure 7A**). Using this stepwise approach, we correctly labeled 99.66% cell types
509 using Seurat and 99.27% using scANVI (**Figure S9B**). Cluster identity calling, however, was more
510 accurate in Seurat with 89.11-95.19% of cells correctly annotated across cell types, whereas
511 scANVI had 69.33-92.31% properly labeled (**Figure S9C**). Moving forward with Seurat given its
512 superior predictions in this use case, we next validated the output by calculating cell cluster
513 abundances using the predicted cell cluster labels and projecting these "query" replicates into the
514 primary infection RM compositional PCA. Remarkably, the query replicates aligned very closely
515 to their real sample replicate counterparts in compositional space (**Figure S9D**). Thus, we
516 validated a label transfer approach to learn cell cluster identities and cellular composition of new
517 scRNA-seq data using our primary infection atlas as a reference.

518

519 **IAV rechallenge is characterized by accelerated and concurrent myeloid and lymphocyte** 520 **memory responses**

521 Having developed a tissue-scale response timeline of acute IAV infection in the nasal
522 mucosa, we next asked how a memory response differs from primary infection on cluster and
523 compositional levels. Thus, we applied our label transfer approach — using the primary infection
524 data as a reference — to new RM samples harvested from mice 60 dpi and 2- and 5-days post
525 rechallenge (dprc) with the same strain of IAV (**Figures 1A and 7A**). All cell types present in the
526 primary infection dataset were captured in the rechallenge samples (**Figure 7B**) and UMAP
527 projection showed strong overlap between the datasets (**Figure S10A**). Plaque assays detected
528 infectious virus in 1-of-5 mice in nasal mucosa, and in 0-of-6 mice in lung upon rechallenge,
529 suggesting immediate control of infection or baseline resistance (**Figure S10B**). If protection was
530 completely neutralizing antibody mediated, however, we would not expect to see large changes
531 in tissue composition. Surprisingly, despite this viral rechallenge paradigm with a matched strain
532 leading to barely any infectious viral shedding, we measured increased proportions of
533 granulocytes, T & NK cells, and B cells following rechallenge that were concordant with relatively
534 reduced proportions of epithelial, endothelial, and stromal cells, indicating immune cell
535 accumulation in the tissue (**Figures 7C and S10C**).

536 Following annotation, we compared changes in cluster abundance over time between the
537 primary and secondary responses to IAV infection (**Figures 7D and S10D**). Like primary infection,
538 IFN-Stim and MHC-I-Hi neutrophil subsets accumulated immediately and maintained elevated
539 levels through 5 dprc. Interestingly, IFN-stimulated MDMs rapidly accumulated while monocytes
540 only slightly increased. Given the total proportion of myeloid cells in the dataset was similar
541 between 60 dpi, 2 dprc, and 5 dprc, these data suggest that MDMs already inside the RM prior to
542 rechallenge quickly responded. Effector Th1 CD4 T cells were also elevated 2 dprc, but effector
543 CD8 T and T_{RM} cells were slower to accumulate. Interestingly, plasma cell abundances, though
544 variable, remained at similar levels between 60 dpi and 2 dprc; however, these abundances
545 decreased 5 dprc, concurrent with an overall reduction in B cell proportion. Cycling basal cells
546 showed no change in abundance following rechallenge, and the increase in IFN-responsive
547 epithelial cells was stunted. Notably, both the *Meg3+MHC-II+* subset and KNIIFE cells that arose
548 following viral clearance in primary infection remained at low levels throughout rechallenge. While
549 we do not yet understand whether their roles may be restricted to resolving primary infection,
550 there may be a necessary inflammation threshold for their expansion, or they may take longer to
551 increase in frequency than the relatively early sampling timepoints post re-challenge.

552 To understand if the quality of antiviral effector responses changed between primary and
553 secondary infection, we performed differential expression analysis within cell clusters (**Figure 7E**
554 **and Supplementary Table 3**). Compared to 8 dpi, *Gzmk+* CD8 T cells at 5dprc exhibited reduced

555 expression of cytotoxic and activation genes, but higher levels of cell survival genes *Birc5* and
556 *Selenoh*, and histone *H2afv*, suggesting induction of epigenetic modifications. T_{RM} cells had lost
557 some activation surface markers by 60 dpi; however, following rechallenge they showed similar
558 expression profiles to those that appeared 14 dpi. Interestingly, expression of *Cd103* and *Gzma*
559 were highest 5 dprc. *Ifng*+*Cd200*+ CD4 T cells may become more prone to cell death during a
560 memory response, with loss of *Mapkapk2*, *Bcl2l1*, and *Cd200*. However, they expressed higher
561 levels of *Itga1*, which has been shown to mark a subset of CD4 T cells that rapidly secrete IFN- γ
562 in the airways following IAV infection (Chapman and Topham, 2010). IFN-stimulated MDMs at 2
563 dprc compared to 8 dpi had lower expression of ISGs, *Ccl4*, and *Fcgr1*, but higher levels of
564 *Tnfaip2*, *Atp5k*, and ribosomal protein coding genes.

565 While changes in abundance or gene expression on an individual cell subset/state level
566 highlight specific differences between primary and secondary responses, we sought to
567 understand how the collective RM tissue-scale response differs. To contextualize on the
568 compositional level, we projected the memory and rechallenge sample replicates into the
569 previously derived compositional PC space for RM in primary infection (**Figure 7F**). The RM 60
570 dpi samples were separated from naïve samples and most resembled 2 dpi, suggesting that even
571 though IAV was cleared by 14 dpi, the nasal mucosa sustained significant changes in
572 composition. The first memory timepoint 2 dprc recapitulated the variance described by PC1, but
573 there was no significant shift along PC2 unlike in primary infection, suggesting increases in
574 effector immune responses but not broad antiviral activation across all cell types like those seen
575 5 dpi (i.e., IFN-Stim cluster) (**Figure 2G**). Notably, by 5 dprc, the tissue had almost returned to
576 “memory baseline” at 60 dpi in PC-space, indicating that responses had already largely resolved.
577 In case projection obscured important variation between the primary and secondary samples, we
578 also re-ran PCA with abundances from all timepoints and found that the first two PCs were
579 remarkably similar (**Figure S10E**). PC3 captured the differences between datasets, with specific
580 epithelial cell subsets higher in primary infection and chondrocytes, plasma cells, and T_{RM} cells
581 enriched in samples during and after rechallenge (**Figure S10F**).

582 To quantify the overall difference between timepoints, we calculated compositional
583 distances between all pairs of sample replicates (**Figure S10G**). In primary infection, RM
584 increasingly separated from the naïve state up through 8 dpi but then became closer as infection
585 is resolved (**Figure 7G**). Corroborating the PCA, the nasal mucosa 60 dpi was still distinct from
586 its naïve state. Upon rechallenge, RM also separated from 60 dpi; however, the extent of that
587 difference (MD=3.50) was less than between naïve and 5 dpi (MD=5.37) and 8 dpi (MD=6.67)
588 indicating that the memory response was more succinct (**Figure 7H**). Comparing primary infection

589 timepoints with peak memory response, each primary infection timepoint was similarly distinct
590 from 2 dprc, suggesting that prior infection rewired the RM response to IAV infection (**Figure 7I**).
591 Summarizing the primary and secondary responses to infection described here, we present a
592 timeline of the key immune and epithelial cell responses during IAV infection and rechallenge
593 illustrating that many of the stepwise changes seen in primary infection occur in a more
594 coordinated and accelerated fashion (**Figure 7J**).

595

596 **DISCUSSION**

597 Here, we present a longitudinal, multi-region, scRNA-seq atlas of the murine nasal
598 mucosa during primary and secondary IAV infection. Cataloguing the distribution and temporal
599 dynamics of the diverse cell types, subsets, and states present, we develop and apply a
600 compositional framework to understand tissue-scale changes occurring throughout primary and
601 memory responses to viral infection. Neutrophil activation responses following infection precede
602 broader IFN-stimulated responses in epithelial, myeloid, and lymphoid cells. By 8 dpi, effector
603 CD8 and CD4 T cell subsets accumulate alongside recently differentiated MDMs. Following viral
604 clearance at 14 dpi, T_{RM} -like cells and IgG+/IgA+ plasma cells appear in the nasal mucosa, which
605 has achieved distinct cellular composition from the naïve state with these adaptive immune
606 subsets being sustained until 60 dpi. Careful investigation of the epithelial cell compartment also
607 revealed rare, previously undescribed subsets, including KNIIFE cells. We validate and localize
608 the presence of these cells, provide evidence for their interaction with *Cxcr6*-expressing
609 lymphocytes, and show co-expression of *Krt13*, *Cd274* (PD-L1), and *Cxcl16* on the nasal floor
610 following viral clearance. Even using the same viral strain, which was effectively controlled to limit
611 almost any detectable viral replication, our use case of the primary infection atlas to understand
612 secondary infection shows that rechallenge induces surprisingly widespread yet coordinated and
613 accelerated changes to cellular composition. In particular, we identify accelerated neutrophil,
614 macrophage, and T cell responses in memory with a reduced burden on epithelial cells to express
615 the joint interferon and proliferative response programs of primary infection.

616 Comprehensively understanding airway mucosal immunity has become an urgent unmet
617 need in the face of emerging and recurring respiratory pathogens (Lavelle and Ward, 2022;
618 Morens et al., 2023; Roth et al., 2018; Russell et al., 2020). In particular, the nasal mucosa is at
619 the forefront of mammalian host responses to airborne pathogens and functions as both an entry
620 site and the primary barrier for infections of the respiratory tract. Consequently, the nasal mucosa
621 is thought to be the site of initial engagement of respiratory viruses to generate both local T cell
622 memory (Pizzolla et al., 2017) and neutralizing antibodies (Liew et al., 2023; Sterlin et al., 2021;

623 Wellford et al., 2022; Weltzin et al., 1996). Determining how these responses occur following
624 primary infection, and how immune and non-immune cells in the nasal mucosa contribute to viral
625 clearance and subsequent memory, is critical to inform the design of next-generation nasal
626 vaccines and therapeutics.

627 Although live-attenuated IAV mucosal vaccines work in children (Costa-Martins et al.,
628 2021; Johnson Jr. et al., 1985), recent attempts to administer new vaccine formulations i.n. in
629 both children and adults have had mixed results (Madhavan et al., 2022; Nouën et al., 2022; Vaca
630 et al., 2023). New approaches utilizing “prime-and-pull” strategies (Mao et al., 2022) and mucosa-
631 targeting delivery platforms (Hartwell et al., 2022) support the promise of i.n. vaccines. A better
632 understanding of natural mucosal immune memory may inform a more comprehensive
633 assessment of the efficacy of these and other immunization approaches and potentially reveal
634 avenues for further improvement. The present atlas of murine nasal mucosa comprehensively
635 catalogues the tissue-scale response following primary and secondary IAV infection, highlighting
636 the dynamic and cooperative cell subsets and states contributing to viral resolution and memory
637 recall.

638 One focus of the present work is the multi-faceted epithelial makeup of the nasal mucosa
639 and its response to IAV infection. Basal cells in the nasal mucosa give rise to epithelial cells
640 reminiscent of pseudostratified epithelium found in the trachea (Davis and Wypych, 2021), but we
641 and others have also captured several additional epithelial cell subsets not found in other parts of
642 the airway. Our atlas validates recent work in mouse describing sustentacular cells, ionocytes,
643 nasal tuft cells, and serous cells (Brann et al., 2020; Ualiyeva et al., 2022). Moreover, we describe
644 for the first time several clusters of epithelial cells with undetermined function: (1) *Scgb-*
645 *b27+Cck+*, (2) *Meg3+MHC-II+*, (3) *Klk1+Fxyc2+*, and (4) KNIIFE cells. Except for the *Scgb-*
646 *b27+Cck+* cluster, the remaining previously undescribed clusters all exist at low frequencies (<
647 1% of all epithelial cells) in naïve mice and may have been missed in experiments without
648 sufficient cell numbers or utilized cell sorting.

649 The viral signaling and proliferative capacities of epithelial cells associate with COVID-19
650 disease trajectory (Sposito et al., 2021; Ziegler et al., 2021). Our data confirm that transient IFN-
651 responsive epithelial cell subsets, including cycling basal cells, arise in the nasal mucosa during
652 IAV infection. During the peak response, nasal basal cells co-expressed cell cycle and IFN-
653 response programs, which have been previously described as non-compatible in lungs (Broggi et
654 al., 2020; Major et al., 2020). Given the diverse roles of nasal epithelial cells and the need to
655 protect olfactory sensory neurons (Dumm et al., 2020), nasal basal cells may be more tolerant of
656 IFN-response signaling during proliferation than basal cells in the lower airways. Notably,

657 epithelial IFN-induced responses were significantly reduced upon rechallenge. This difference
658 could reflect several non-exclusive mechanisms during recall, including an overall reduction or
659 shortening in IFN production or signaling, lower viral load, or a potential tolerized basal cell state.
660 Airway basal cells can develop transcriptional memory in vitro (Adamson et al., 2022), but whether
661 primary infection can confer durable memory to viral immunity, as has been seen for allergic
662 inflammation (Ordovas-Montanes et al., 2018), requires further investigation.

663 In addition to epithelial responses, IAV infection also precipitated a highly dynamic,
664 stepwise response by immune cells that was initially dominated by myeloid subsets. Specifically,
665 we observed a substantial early influx of neutrophils followed by monocytes that then
666 differentiated into MDMs concurrent with the arrival of effector T cells. The evidence for both
667 resident (Yao et al., 2018) and recruited (Aegerter et al., 2020) macrophages in the lungs to
668 engage in memory responses suggests that a similar phenomenon may occur in the nasal
669 mucosa. After depleting circulating monocytes during acute infection, MDM formation was
670 markedly reduced, indicating that the majority of nasal MDMs at 8 dpi differentiated from newly
671 recruited monocytes. Interestingly, during a memory response MDMs, but not monocytes,
672 increased in abundance 2 dprc even though overall myeloid frequencies remained unchanged,
673 indicating that either recruited MDMs replaced local myeloid cells or MDMs already present in the
674 tissue expanded to exert antiviral effector functions. If the latter, understanding the mechanisms
675 by which enhanced myeloid function is maintained and recalled in the nasal mucosa could yield
676 a new avenue for designing improved mucosal vaccines.

677 The role of adaptive immune responses to IAV infection have been well described in the
678 lower respiratory tract (Chapman and Topham, 2010; Krammer, 2019; McMaster et al., 2015;
679 Onodera et al., 2012; Slütter et al., 2013; Wein et al., 2019), but their dynamics and quality in the
680 nasal mucosa are less understood. Antibody-mediated immunity following primary and secondary
681 IAV infection has been described (Chen et al., 2018) and falls outside the scope of the present
682 study. Capturing substantial bone marrow resident cells in the OM samples during primary
683 infection, we noted a marked increase in this region of granulocyte and B cell progenitors 5 dpi.
684 Systemic and circulating cytokine responses are documented to induce hematopoiesis during
685 infection (Zaretsky et al., 2014), so it follows that local type I inflammation in the nasal mucosa
686 alongside high levels of IFNs could induce rapid granulo- and lymphopoiesis. Antibody-producing
687 B cell response dynamics, however, were variable in our model with sizeable frequencies of
688 plasma cells detected in 1- or 2-of-3 mice at 14 dpi, 60 dpi, and 2 dprc. Wellford et al., recently
689 showed in an influenza B model that the OM requires mucosa resident plasma cells to prevent
690 transmission to the brain; the RM, alternatively, can receive neutralizing antibodies from both

691 serum and local plasma cells (Wellford et al., 2022). To what extent local nasal plasma cell derived
692 IgG and IgA play roles in stymying infection during rechallenge, and whether non-neutralizing
693 antibody functions help activate other immune subsets (e.g., Fc receptor mediated signaling),
694 must be further explored.

695 IAV infection of the nasal mucosa resulted in classical T cell responses with both antiviral
696 effector CD8 T cells expressing cytotoxic genes and Th1 CD4 T cells expressing *Irfng* and *Tnfrsf4*
697 (OX40) arising at 8 dpi. Proportionality analysis revealed their coordination with an influx of IFN-
698 Stim MDMs expressing *Cxcl9* and *Cxcl16*, and NICHES predicted several modes of
699 communication between all three clusters, suggesting MDMs may provide activation signals for T
700 cells in the nasal mucosa. While infectious titers waned between 2 and 8 dpi, effector T cell
701 responses likely played a critical role in completely extinguishing IAV infection by 14 dpi. Finding
702 upward of ~50% of all T and NK cells by 14 dpi belonged to the T_{RM}-like cluster in the RM tissue,
703 we validate their presence and phenotype in the nasal cavity following IAV infection (Pizzolla et
704 al., 2017; Wiley et al., 2001). Unlike in the lung where T_{RM} cells quickly wane following infection
705 (Slütter et al., 2017), our data demonstrate robust frequencies out to 60 dpi that are further
706 amplified during rechallenge; moreover, in addition to the RM, we find T_{RM} in OM and LNG tissue,
707 where virus is only detected at low levels or not at all. While T_{RM} contribute to an effective memory
708 response upon rechallenge (Ariotti et al., 2014; McMaster et al., 2015; Schenkel et al., 2014;
709 Steinbach et al., 2016), differential expression across timepoints of the *Cd103*⁺ CD8 T cell cluster
710 in our dataset did show strong gene expression differences between these cells at 2 dprc and
711 following primary infection; moreover, their relative proportion only increased by ~2x over levels
712 at 60 dpi. Given recent work highlighting the importance of T_{RM} in mitigating nasal viral infections
713 (Mao et al., 2022; Pizzolla et al., 2017), understanding which cell subsets and signals establish
714 and maintain the T_{RM} niche could help guide mucosal vaccine strategies with heterotypic
715 protection.

716 Following viral clearance, several unique subsets of epithelial cells with potential immune
717 signaling and inflammatory regulation capacity substantially increased in abundance. In addition
718 to a large cluster of goblet/secretory cells with predicted DC/neutrophil communication ability, we
719 also discovered a subset of epithelial cells uniquely expressing *Krt13* and *Krt6a* in the nasal
720 mucosa, hereto named ***Krt13*⁺ nasal immune-interacting floor epithelial (KNIIFE)** cells.
721 Phenotypically, KNIIFE cells were reminiscent of the recently described “hillock” cells in the
722 trachea expressing *Krt13*, *Ecm1*, and *Lgals3* (Montoro et al., 2018); however, KNIIFE cells
723 additionally expressed several genes often found in macrophages including *Cd274* (PD-L1), *Il1a*,
724 *Tnf*, and *Cxcl16*. This cluster was present at low levels throughout infection until expanding 14

725 dpi and remained stable during rechallenge. At 14 dpi, we measured *Krt13* and *Cxcl16* co-
726 expression in situ nearby *Cxcr6* expressing cells, especially along the nasal floor. These results
727 raise the possibility that KNIIFE cells, by providing a source for CXCL16 beyond that expressed
728 by myeloid cells, may contribute to the establishment of the resident memory T cell pool in the
729 nasal mucosa, as has been suggested for this chemokine pathway in other tissues (Clark et al.,
730 2006; Morgan et al., 2008; Tse et al., 2014; Wein et al., 2019). The enrichment of KNIIFE cells
731 along nasal floor and below the vomeronasal organ prompts the question of whether these cells
732 interact with particles or irritants just entering or settling in the nose and play a regulatory role in
733 tissue tolerance and/or immunity.

734 Compositional scRNA-seq analyses are becoming more common to discern differences
735 between disease trajectories (Ordovas-Montanes et al., 2018; Smillie et al., 2019; Zheng et al.,
736 2021), treatment groups (Darrah et al., 2020; Zhang et al., 2022b), and/or species (Chen et al.,
737 2022; Li et al., 2022). Current tools focus on identifying specific clusters or gene programs that
738 are compositionally distinct between groups (Büttner et al., 2021; Cao et al., 2019; Dann et al.,
739 2022). However, the power of compositional scRNA-seq data lies in its structure; namely, singular
740 changes in composition cannot be independent and must correspond with mutual changes in
741 other clusters/programs. Leveraging the biological replicates and multiple timepoints present in
742 our atlas, we utilized straightforward tools for compositional analysis adapted from microbiome
743 research (Gloor et al., 2017; Lin and Peddada, 2020; Quinn et al., 2018) to understand tissue-
744 scale changes within the nasal mucosa throughout IAV infection. PCA of cell cluster abundances
745 across sample replicates separated nasal regions and depicted structured stepwise changes in
746 epithelial and immune cell subsets throughout infection trajectory. Proportionality analysis, which
747 avoids the spurious associations present in Pearson correlation applied to compositional data
748 (Lovell et al., 2015), revealed pairs and groups of clusters with significantly similar compositional
749 trajectories (e.g., IFN-stimulated MDMs and effector CD4 and CD8 T cells) and can be readily
750 applied to discover similarities across various metadata. Finally, metrics like Aitchison distance
751 (Aitchison et al., 2000) capture holistic changes in tissue-scale cellular composition and support
752 standard tests for differences between group means (e.g., Welch's ANOVA) to assess global
753 similarity and compositional distance traveled by a tissue. Applied to our datasets, the RM
754 "travels" less during the memory response to IAV than during primary infection, suggesting prior
755 infection induces a coordination of responses that were previously unsynchronized. We propose
756 that these approaches for analyzing scRNA-seq data constitute a new framework for
757 understanding and summarizing whole tissue- and biopsy-scale changes in cellular composition
758 at high resolution in health, disease, and/or under perturbation.

759 Collectively, our murine nasal mucosa atlas of primary IAV infection longitudinally
760 catalogues the cell types, subsets, and states present throughout distinct nasal regions. We
761 demonstrate the utility of our dataset to serve as an annotation reference for newly generated
762 scRNA-seq datasets and apply it to understand how the response to infection in the RM differs
763 during a memory recall following IAV rechallenge. These findings will help contextualize studies
764 of the nose in humans and highlight key immune and epithelial cell responses to recapitulate in
765 future nasal vaccines and therapeutics to drive increased synchronicity in nasal memory
766 responses.

767

768 **Limitations of the study**

769 First, we acknowledge that cluster abundance-based compositional analyses are inherently
770 dependent on how clustering was performed, and thus implicitly incorporates, to some degree,
771 operator bias. While we believe our approach to be as impartial as possible through use of
772 iterative clustering, it will be imperative to implement robust, reproducible clustering analyses (Hu
773 et al., 2019; Patterson-Cross et al., 2021; Zheng et al., 2021) prior to compositional analysis
774 moving forward. Partial labeling of cells by hashing antibodies may also have obscured changes
775 in composition over time. Second, detection of IAV transcripts by scRNA-seq was limited. Other
776 studies have included spike-in primers to facilitate additional capture of viral nucleic acids
777 (Ratnasiri et al., 2023); it is possible that we were not sufficiently sensitive to IAV transcripts
778 without these spike-in primers. Also, cells productively infected with virus may not be sufficiently
779 viable through our tissue processing pipeline, leading to artificially low numbers of cells containing
780 IAV reads. Third, to increase the relative proportion of non-epithelial cells in our scRNA-seq
781 dataset, we performed a partial EpCAM depletion using magnetic beads. This decision was made
782 following preliminary experiments comparing this approach to un-depleted RM tissue in naïve
783 mice and 2 dpi; we found that depletion similarly reduced all epithelial cell clusters without bias
784 and did not result in the loss of IAV+ cells. Thus, the cellular compositions throughout the study
785 represent the nasal mucosa tissue after both dissociation and epithelial cell depletion and,
786 therefore, do not reflect the true frequencies of cell types within intact nasal mucosa.
787 Nevertheless, our atlas can still be used to assign cell cluster labels to new datasets where
788 epithelial cells have not been depleted and could inform spatial transcriptomics approaches to
789 derive more accurate cell abundances in vivo. Indeed, spatial transcriptomics and/or multiplexed
790 immunofluorescence approaches will help validate the spatial organization and quantification of
791 cell clusters defined here; however, given the complexity of the nasal mucosa and difficulty in
792 sectioning through the nasal bone, further work will need to be done to validate, adapt and refine

793 imaging protocols for this unique tissue. Additional experiments to test how various influenza
794 strains, other respiratory pathogens, and vaccination strategies impact the composition and timing
795 of responses in the nasal mucosa to IAV challenge are warranted (Rutigliano et al., 2010).

796

797 ***Acknowledgements***

798 We would like to thank members of the Ordovas-Montanes and von Andrian labs for insightful
799 discussions and advice. S.W.K. was supported by the Cancer Research Institute's Irvington
800 Postdoctoral Fellowship. J.O.M. is a New York Stem Cell Foundation – Robertson Investigator.
801 J.O.M. was supported by the AbbVie-Harvard Medical School Alliance, the Richard and Susan
802 Smith Family Foundation, the AGA Research Foundation's AGA-Takeda Pharmaceuticals
803 Research Scholar Award in IBD – AGA2020-13-01, the HDDC Pilot and Feasibility P30
804 DK034854, the Leona M. and Harry B. Helmsley Charitable Trust, The Pew Charitable Trusts
805 Biomedical Scholars, The Broad Next Generation Award, The Chan Zuckerberg Initiative
806 Pediatric Networks, The Mathers Foundation, The New York Stem Cell Foundation, NIH R01
807 HL162642, NIH R01 DE031928 and The Manton Foundation Cell Discovery Network at Boston
808 Children's Hospital. This work was supported by the AbbVie–HMS Alliance Program. Sequencing
809 of the scRNA-seq libraries was performed with AbbVie Inc. at the Genomics Research Center
810 and Immunoprofiling Center in collaboration with Steven Leonardo (former AbbVie employee),
811 Abel Suarez-Fueyo, Neha Chaudhary, Jozsef Karman, Aridaman Pandit, and Amlan Biswas.
812 Imaging was performed with MicRoN and HMS Center for Immune Imaging at Harvard Medical
813 School. Anti-CCR2 antibody MC-21 was generously provided by Prof. Matthias Mack (Universität
814 Regensburg). Training for the RNAscope experiments was facilitated by Anoohya N. Muppirala
815 and Meenakshi Rao at Boston Children's Hospital. Daniel Lingwood (Ragon Institute of Mass
816 General, MIT, and Harvard), Alex Shalek (MIT), Paolo Cadinu and Jeffrey Moffitt (BCH), Colin
817 Bingle (Sheffield) provided helpful feedback and discussion on experimental design and
818 interpretation of the results. Additionally, we would like to thank Susan Westmoreland for insightful
819 discussions as well as Shankar Subramanian, Michelle Cordoba Gunter, Isabel Chico-Calero,
820 Jochen Salfeld, and Mark Namchuk for supporting the AbbVie–HMS Alliance Program Area 1
821 which enabled the scope of this work.

822

823 ***Author contributions***

824 Conceptualization, S.W.K., C.M., U.H.vA., and J.O-M.;

825 Methodology, S.W.K. and C.M.;

826 Software, S.W.K., E.M.L., and T.J.L.;

827 Formal Analysis, S.W.K., C.M., E.M.L., and T.J.L.;

828 Investigation, S.W.K., C.M., E.M.L., J.M., K.N., E.O., and J.O-M.;

829 Data Curation, S.W.K.;

830 Writing – Original Draft, S.W.K and C.M.;

831 Writing – Review & Editing, S.W.K., C.M., E.M.L., U.H.vA., and J.O-M.;

832 Supervision, U.H.vA. and J.O-M.;

833 Funding Acquisition, S.W.K., U.H.vA., and J.O-M.

834

835 ***Declaration of Interests***

836 S.W.K. reports compensation for consulting services with Monopteros Therapeutics, Flagship

837 Pioneering, and Radera Biosciences. J.O.M. reports compensation for consulting services with

838 Cellarity, Tessel Biosciences, and Radera Biotherapeutics. U.H.v.A. is a paid consultant with

839 financial interests in Avenge Bio, Beam Therapeutics, Bluesphere Bio, Curon, DNAlite, Gate

840 Biosciences, Gentibio, Intergalactic, intrECate Biotherapeutics, Interon, Mallinckrodt

841 Pharmaceuticals, Moderna, Monopteros Biotherapeutics, Morpnic Therapeutics, Rubius, Selecta

842 and SQZ.

843

844

845 **METHODS**

846 **Resource availability**

847 **Lead contact**

848 Further information and requests for resources and reagents should be directed to and
849 will be fulfilled by the lead contact Jose Ordovas-Montanes ([jose.ordovas-
850 montanes@childrens.harvard.edu](mailto:jose.ordovas-montanes@childrens.harvard.edu)).

851

852 **Material availability**

853 All the mouse lines used in this study are available from Jackson Laboratories. The anti-
854 CCR2 antibody MC-21 was provided as a gift by Prof. Matthias Mack. This study did not generate
855 new unique reagents.

856

857 **Data and code availability**

858 All sequencing data reported in this paper will be available in FASTQ read format and
859 cellbender corrected gene expression matrix format at Gene Expression Omnibus upon
860 publication as we plan to submit this work for pre-print. The annotated data can also be explored
861 at the Broad Institute Single Cell Portal under study numbers SCP2216 and SCP2221. All the
862 code generated and used to analyze the data reported in this paper will be available on GitHub
863 in the jo-m-lab/IAV-nasal-sc-atlas repository.

864

865 **Experimental model and subject details**

866 **Mice**

867 All experiments were approved by the Harvard University Institutional Animal Care and
868 Use Committee and run following NIH guidelines. C57BL/6J (B6) mice 6 to 8 weeks old were
869 purchased from The Jackson Laboratory and experiments commenced 1 to 3 weeks following
870 their arrival. Mice were infected with 10^4 pfu PR8 in a 10 μ L volume that was administered by
871 pipette dropwise to the nares to allow each drop to be inhaled. Mice were restrained during this
872 administration but not anesthetized, to maintain the virus in the upper respiratory tract. All mice
873 were housed in a BSL-2+ facility with specific pathogen free conditions.

874

875 **Method details**

876 **Virus growth, quantification, and mouse infections**

877 IAV strain A/Puerto Rico/8/1934 (PR8) and Madin-Darby canine kidney (MDCK) cells were
878 generously provided by Dr. Daniel Lingwood and Dr. Maya Sangesland of the Ragon Institute of

879 Mass General, MIT, and Harvard. Virus was propagated and quantified in MDCK cells. MDCK
880 cells were grown at 37°C with 5% CO₂ in cell growth media: Dulbecco's modified eagle's medium
881 (DMEM) (Corning, #10-017-CV), 10% fetal bovine serum (FBS; Gemini #100-106), 1X
882 Penicillin:Streptomycin (Gemini, 100X stock: 400109). PR8 was grown in MDCK cells in influenza
883 growth media: Iscove's DMEM (Corning, # 10-016-CV), 0.2% bovine serum albumin (BSA; EMD
884 Millipore, EM-2960), 1Xm Penicillin:Streptomycin, and 2µg/mL TPCK treated Trypsin (Sigma,
885 T1426).

886 For viral load quantification experiments, mice were sacrificed in CO₂ and lungs and heads
887 were separated. For the nasal cavity, fur and skin were removed and the lower jaws cut off. The
888 entire nasal cavity or lungs were collected into 1mL PBS with 2.3mm Zirconia/Silica beads
889 (Biospec Products, 11079125z) and stored on ice. The tissue was homogenized in an OMNI Bead
890 Ruptor Elite at 3m/s for 30 seconds twice, centrifuged 500g for 5 minutes, and supernatant was
891 collected and stored at -80°C until thawed for plaque assays. Virus titers were measured by
892 plaque assays in confluent MDCK cells in 6-well plates. MDCK cells were grown in cell growth
893 media, washed with sterile phosphate-buffered saline (PBS), then washed with influenza growth
894 media. Media was removed and serial dilutions of viral supernatant in influenza growth media
895 were added to each well in a 400µL volume, incubated for 1 hour at 37°C, then overlaid with
896 0.3% agarose in influenza growth media. Infected cells were incubated for three days at 37°C,
897 fixed with 4% paraformaldehyde, stained with crystal violet, washed, and plaques were counted.

898

899 **Tissue harvesting, single-cell suspension preparation, and hashtag labeling**

900 Three separate regions of the nasal tissue were harvested independently: (1) the
901 respiratory mucosa (RM), (2) the olfactory mucosa (OM), and (3) the lateral nasal gland (LNG).
902 The nasal tissue was collected by removing the skin and connective tissue from around the head,
903 cutting off the lower jaw, and opening the nasal cavity by peeling away the nasal bone from the
904 rest of the skull. Tissue separation and collection was performed using a dissection scope with a
905 4x objective. All nasal tissue surrounding the nasoturbinates, maxillary turbinates, and septum,
906 including the mucosa that runs along the nasal lateral walls between the nasoturbinates and
907 maxillary turbinate, and the mucosal tissue under the nasal bone that connects the nasoturbinates
908 and septum, were collected together and constitute the RM. After removal of the RM the ethmoid
909 turbinates were collected including both the mucosal tissue and the bone and cartilage of the
910 turbinates, but not the surrounding skull, constituting the OM. After removal of the OM, the LNG
911 was exposed and could be collected without any bone or cartilage. The nasal-associated
912 lymphoid tissue (NALT) was not collected in any of the three regions.

913 Each nasal tissue region was collected into 750µL Wash Media (RPMI 1640, 2% FBS, 10
914 mM HEPES, and 100U/ml penicillin G, 100µg/ml streptomycin) and stored on ice. Tissues were
915 chopped with scissors then 750µL Digestion Media (Wash Media with 100µg/mL Liberase (Sigma,
916 #5401127001) and 100µg/mL of DNase I (Roche, #10104159001)) was added. Tissues were
917 incubated at 37°C with end-over-end rotation, 30 minutes for RM and OM, 20 minutes for LNG.
918 13.3µL EDTA (0.5M) was added to each sample and then cells were washed with HBSS Media
919 (HBSS (Ca, Mg Free, 500 mL), 10mM EDTA, 10mM HEPES, 2% FBS) and filtered through a
920 70µm nylon cell strainer. Cells were pelleted by centrifugation 500g for 10 minutes, resuspended
921 with ACK (Ammonium-Chloride-Potassium) lysis buffer for 1 minute on ice, and then diluted with
922 9mL HBSS Media and centrifuged 500g for 5 minutes twice. Cells were then resuspended in 1mL
923 Isolation Buffer (PBS, 0.1% BSA, 2mM EDTA) pre-mixed with 25µL anti-EpCAM-biotin-
924 Dynabeads (anti-EpCAM-biotin antibody (G8.8, Biolegend) bound to Dynabeads Biotin Binder
925 (ThermoFisher)) for a light epithelial cell depletion, incubated for 15 minutes on ice, washed with
926 Isolation Buffer and placed on a Dynamag for 2 minutes. Supernatants were collected, centrifuged
927 500g for 5 minutes, resuspended in 100µL Staining Buffer (PBS, 1% BSA, 0.01% Tween) and
928 10µL Fc block, and incubated on ice for 10 minutes. Next, 0.5µg Biolegend TotalSeq Hashing
929 antibodies B0301, B0302, or B0303 were added so that each mouse had all three nasal regions
930 (RM, OM, and LNG) stained with one of the three antibodies, and incubated on ice for 20 minutes.
931 Cells were then washed extensively to remove excess antibody with 10mL Staining Buffer and
932 centrifugation at 500g for 5 minutes twice. Cells were resuspended in Loading Buffer (PBS and
933 0.04% BSA), counted, and pooled equally (13,500 cells/sample) between three mice for each
934 region. Finally, each set of pooled cells were centrifuged 500g for 5 minutes and resuspended in
935 42µL Loading Buffer for downstream scRNA-seq processing.

936

937 **Single-cell RNA-seq**

938 Pooled samples from each nasal region (RM, OM, and LNG) were processed using the
939 10x Genomics Chromium Next GEM Single Cell 3' Kit v3.1 and Feature Barcoding Kit with dual
940 indices per the manufacturer's instructions. Approximately 40,000 cells per pooled reaction were
941 loaded on the 10x Genomics Chromium Controller. Library quality was evaluated using the Agilent
942 TapeStation 4200 (Agilent). Prior to sequencing, the gene expression and hashtag libraries were
943 pooled 20:1. Sequencing was performed on either the NovaSeq 6000 or NextSeq 2000 (Illumina)
944 with an average RNA read depth of 16,000 reads/cell and hashtag read depth of 500 reads/cell.

945

946 **Immunofluorescence Microscopy**

947 Mice were euthanized in CO₂ and their heads following skin, fur, and lower jaw removal
948 were placed in 4% paraformaldehyde for 1-4 hours on ice for fixation. Heads were transferred to
949 0.5M EDTA for 2-3 days at 4°C for bone decalcification. Heads were transferred to 30% sucrose
950 in PBS for cryoprotection for 2 days at 4°C then rapidly frozen in NEG-50 using dry ice. Frozen
951 heads were stored at -20°C until cryostat sectioning. Mouse nasal tissues were cut into 50-100µm
952 sections, permeabilized with 0.3% Tween in PBS (PBST) for 1 hour, then incubated overnight at
953 4°C with antibodies, DAPI, and Fc block at a 1:200 dilution in PBST. Antibodies used: anti-
954 Influenza A virus NS1 (PA5-32243, ThermoFisher), anti-acetyl- α -tubulin (Ly640, D20G3, Cell
955 Signaling Technology), anti-CD45 (30-F11, Biologend), anti-EpCAM (G8.8, Biologend), anti-Krt13
956 (EPR3671, Abcam), anti-PD-L1 (10F.9G2, Biologend), and anti-IgA (mA-6E1, ThermoFisher).
957 Samples were then washed 3 times with PBST in 15-minute intervals at room temperature,
958 mounted on glass slides with Prolong Gold, and visualized with an Olympus FLUOVIEW FV3000
959 confocal laser scanning microscope.

960

961 **qPCR**

962 RM tissue was collected as described above from mice and lysed in Buffer RLT (Qiagen)
963 + 1% beta-mercaptoethanol (Sigma) via gentleMACS Octo Dissociator in M-Tubes (Miltenyi
964 Biotec). RNA was extracted from tissue lysate by RNeasy Mini column purification (Qiagen)
965 following the manufacturer's instructions. cDNA was then generated following the SmartSeq II
966 protocol as previously described (Trombetta et al., 2014). qPCR was performed using TaqMan
967 reagents and probes (ThermoFisher) on a CFX384 Real-Time PCR System.

968

969 **Antibody-based depletion**

970 Naïve or PR8 infected B6 mice were administered daily 20µg anti-CCR2 depleting
971 antibodies (MC-21 generously provided by Prof. Matthias Mack, Universität Regensburg) or rat
972 IgG2b, κ isotype control (Biologend, #400644) intraperitoneally (i.p.). 24h following one
973 administration, blood was collected from naïve mice by tail vein bleed into FACS buffer (PBS,
974 0.5% BSA, 2mM EDTA) and stored on ice before processing for flow cytometry.

975 PR8 infected mice were administered antibodies 3, 4, and 5 dpi in 24h intervals. For this
976 experiment, mice were euthanized at 8 dpi.

977

978 **Flow cytometry**

979 Blood was processed for flow cytometry by pelleting cells by centrifugation and
980 resuspending with ACK lysis buffer to remove RBCs. Cells were then washed with FACS buffer

981 and stained in 50 μ L for flow cytometry using the following antibodies: anti-CCR2 (475301, R&D
982 Systems), anti-CD11b (M1/70, Biolegend), anti-CD19 (6D5, Biolegend), anti-CD3e (145-2C11,
983 Biolegend), anti-CD45 (30-F11, Biologend), anti-Ly6C (HK1.4, Biolegend), anti-Ly6G (1A8,
984 Biolegend), and anti-NK1.1 (PK136, Biolegend). Cells were analyzed using the Beckman Coulter
985 CytoFLEX.

986 For RM tissue, mice were anesthetized i.p. with ketamine (100 mg/kg body weight) and
987 xylazine (10 mg/kg body weight) prior to euthanasia and administered 1 μ g anti-CD45 antibody
988 (30-F11, Biologend) by retroorbital intravascular injection to label CD45+ cells in circulation. Mice
989 were then euthanized 3 minutes later in CO₂. RM tissue was processed as described above for
990 tissue harvesting and single-cell suspension preparation through ACK lysis and dilution. Cells
991 were then centrifuged and resuspended in 100 μ L FACS buffer LIVE/DEAD Fixable Aqua Dead
992 Cell Stain (ThermoFisher #L34966) per manufacturer's instructions. Cells were then washed and
993 stained for 30min at 4°C in the dark with Fc block diluted 1:200 and the following antibodies: anti-
994 CD11b (M1/70, Biolegend), anti-CD11c (HL3, BD Biosciences), anti-CD19 (6D5, Biolegend), anti-
995 CD3e (145-2C11, Biolegend), anti-CD45 (30-F11, Biologend), anti-CD64 (X54-5/7.1, Biolegend),
996 anti-Ly6C (HK1.4, Biolegend), anti-Ly6G (1A8, Biolegend), anti-F4/80 (BM8, Biolegend), anti-
997 MHC-II (M5/114.15.2, Biolegend), and anti-NK1.1 (PK136, Biolegend). Following staining, cells
998 were washed in FACS buffer, and analyzed. To determine cell counts, AccuCheck Counting
999 Beads (ThermoFisher #PCB100) were added to every sample.

1000

1001 **RNAscope Microscopy**

1002 RNA *in situ* hybridization was performed according to manufacturer's instructions for the
1003 RNAscope Multiplex Fluorescent Reagent Kit v2 (Advanced Cell Diagnostics ACD, 323270) on
1004 20 μ m thin sections of fixed-frozen murine nasal mucosa tissue collected 14 dpi. We implemented
1005 the following modifications to preserve tissue integrity: 1) 5 min PBS wash preceding initial baking
1006 of slides was removed; 2) slides were baked for 30 min at 60°C following EtOH dehydration; 3)
1007 target retrieval time was reduced to 5 min; 4) slides were baked for 60 min at 60°C following target
1008 retrieval; and 5) tissue sections were incubated in Protease Plus instead of Protease III for milder
1009 protease digestion. Probes used included Mm-Krt13 (ACD, 575341), Mm-Cxcr6-C2 (ACD,
1010 871991-C2), Mm-Cxcl16-C3 (ACD, 466681-C3), and Mm-Cd274-C3 (ACD, 420501-C3).
1011 Following signal amplification, Opal 520 (Akoya Biosciences, FP1487001KT), Opal 570 (Akoya
1012 Biosciences, FP1488001KT), and Opal 690 (Akoya Biosciences, FP1497001KT) dyes were used,
1013 diluted 1:1000 in TSA buffer (ACD, 322809). Nuclei were stained with DAPI and slides were

1014 mounted with VECTASHIELD PLUS (Vector Laboratories, H-1900). Confocal images were
1015 collected using an Olympus FLUOVIEW FV3000 confocal laser scanning microscope.

1016

1017 **Quantification and statistical analysis**

1018 **Single-cell RNA-seq alignment, cleanup, and pre-processing**

1019 To detect reads originating from IAV, we built a combined genome of mm10 (GRCm39)
1020 and the sequences for PR8 (NCBI Taxonomy ID #211044). The eight PR8 genomic viral segment
1021 sequences (NC_002023.1, NC_002022.1, NC_002021.1, NC_002020.1, NC_00219.1,
1022 NC_2018.1, NC_002017.1, and NC_002016.1) and associated IAV gene annotations were added
1023 to the GRCm39 FASTA and GTF files and processed using the CellRanger's built in "mkref"
1024 function. Sequences were then aligned and quantified using this combined genome with the
1025 CellRanger toolkit (v6.0.1) via Cumulus tools (Li et al., 2020)
1026 (<https://cumulus.readthedocs.io/en/stable/>). Cell sample identity was assigned from the
1027 measurement of TotalSeqB aligned counts using the cumulus demultiplexing tool for feature
1028 barcoding, calling identity for any cell with at least 100 barcodes. To correct for transcript spill-
1029 over, cellbender (Fleming et al., 2022) was applied to the raw output UMI matrices from
1030 CellRanger with the following parameters: *expected_cells=30000*, *fpr=0.01*,
1031 *total_droplets_included=50000*. Cellbender corrected cells were then filtered based on Unique
1032 Molecular Identifiers (UMI) count (>750 & <10000), number of detected genes (>500), and
1033 percentage of mitochondrial genes (<15%). Finally, cells labeled as doublets by demultiplexing
1034 were removed.

1035

1036 **Iterative clustering, cell cluster annotation, and IAV+ cell calling**

1037 Downstream analysis was performed using Seurat (v.4.2.1) (Hao et al., 2021). Briefly, the
1038 entire primary infection dataset underwent normalization using the *scTransform* function followed
1039 by principal component analysis (PCA), shared nearest neighbors (SNN) graph generation,
1040 Louvain clustering, and UMAP embedding. Clustering was performed at multiple resolutions to
1041 help annotate similar and dissimilar clusters. Using clustering *resolution = 0.6*, cluster
1042 specific/enriched markers were calculated. Each cluster was labeled by major cell type based on
1043 the expression of known lineage markers (e.g., *Omp*, *Epcam*, *Ptprc*, *Flt1*, etc.). Doublet clusters
1044 were also annotated based on the lack of unique markers and/or the presence of multiple mutually
1045 exclusive lineage markers (e.g., *Omp+Ptprc+* cells). Following annotation, doublet clusters were
1046 removed, and the normalization/clustering/doublet removal process was repeated twice more
1047 (total of three times) until no doublet clusters were discernable.

1048 The dataset was then divided into separate objects by cell type label for further
1049 subclustering. Following the same routine applied to the full dataset, clusters for each cell type
1050 were annotated with subset/state labels based on prior knowledge and previously published
1051 scRNAseq datasets of the nasal mucosa (Brann et al., 2020; Ualiyeva et al., 2022; Ziegler et al.,
1052 2021). After the first set of annotations in every cell type object, it was apparent that there were
1053 still intra-sample doublets present: mostly contaminating cell types, but also within cell type
1054 doublets (e.g., ionocyte/sustentacular doublets). These clusters were iteratively removed like in
1055 the analysis of the full dataset, for a total of three rounds in each cell type, yielding a total of 127
1056 clusters across the whole dataset. To visualize these clusters' relationships and distribution
1057 across nasal regions, we built a cell cluster "phylogenetic tree" using ARBOL (Zheng et al., 2021),
1058 where the first tier encodes major cell type, the second tier encodes defined subtypes, and the
1059 third tier encodes cluster identity (**Figure S1F**).

1060 Since IAV transcript capture was sparse, we classified IAV+ cells as any cell with 2 or
1061 more UMIs aligned to any IAV PR8 gene.

1062

1063 **Compositional analyses**

1064 After removing multiplets, immune (>97.5%) and endothelial cells (89%) had nearly all
1065 cells assigned a sample replicate while neurons (30.7%), epithelial cells (65.9%), fibroblasts
1066 (52.4%), and other stromal cells (56.4%) had lower sample annotation rates. We note that cells
1067 without a sample replicate assignment were excluded from all compositional analyses. Within cell
1068 type frequencies were calculated on a per replicate basis by counting the number of cells within
1069 each cluster label and dividing by the total number of cells for that cell type captured in that
1070 replicate. For tissue- and region-level compositional analyses, cell cluster abundances were
1071 calculated by deriving cell cluster frequencies over all labeled cells in each sample replicate,
1072 scaling to 3,000 cells per replicate, and log transforming. Subsequent PCAs were calculated from
1073 these log-transformed cell cluster abundances.

1074 Proportionality analysis was performed using the propr package (v4.2.6) (Quinn et al.,
1075 2017) on non-log-transformed cell cluster abundances across all RM sample replicates. We
1076 compared the proportionality statistic ρ to standard Pearson correlation across all pairwise
1077 comparisons and found ρ to be more stringent for significance cutoffs (FDR<0.05) generated by
1078 permutating testing (**Figure S8A**). We built a network using Cytoscape (v3.9.1) comprised of all
1079 significantly proportional cell cluster pairs to assess groups of cell clusters with similar cell
1080 abundance trajectories throughout the infection time course.

1081 RM sample replicate distances were calculated using the Aitchison distance (Aitchison et
1082 al., 2000). Cell cluster abundances were first normalized using the center-log-ratio (clr). Euclidean
1083 distance was then calculated between all pairs of RM sample replicates, yielding three distances
1084 within a timepoint and nine distances between two timepoints. Statistics on Aitchison distances
1085 were performed using a one-sided non-parametric Welch's ANOVA and Dunnett's T3 test for
1086 multiple comparisons in Prism.

1087

1088 **Neutrophil pseudotime analysis**

1089 The neutrophil pseudotime analysis was performed using diffusion mapping as previously
1090 described (Grieshaber-Bouyer et al., 2021). A principal component analysis was run on all cells
1091 assigned to granulocyte clusters, excluding mast cells. The first 20 principal components were
1092 used to compute a cell-to-cell distance matrix using $1 - \text{Pearson correlation coefficient}$ as the
1093 distance metric. Using the destiny package in R (Angerer et al., 2016), we computed a diffusion
1094 map with standard parameters with density normalization and rotate enabled. We manually
1095 selected "Progenitor" cells as the root of the trajectory and used the DPT function to calculate the
1096 pseudotime values, manually scaling the values from 0 to 1.

1097

1098 **Cell-cell signaling analysis**

1099 Three cell networks (IFN-stimulated MDMs : *Gzmk*+ CD8 T cells : *Ifng*+*Cd200*+ CD4 T
1100 cells; *Cd103*+ DCs : *Dusp2*+*Icam1*+ mature neutrophils : *Gp2*+*Lyz2*+ goblet/secretory cells;
1101 *Krt13*+*Il1a*+ epithelial cells : *Cd103*+ CD8 T cells : CD4 T cells) were selected based on high
1102 proportionality throughout the primary infection time-course or specific biological interest to the
1103 authors. Data for the clusters of interest in each network were then subset to RM and timepoint
1104 of interest to best capture individual cells with sufficient spatial and temporal proximity to plausibly
1105 interact, and re-normalized with Seurat's *NormalizeData* function. Since NICHES calculates the
1106 multiplicative expression of ligand-receptor pairs from a random sampling of cells from each cell
1107 type to predict cell-cell communication, Adaptively thresholded Low-Rank Approximation (ALRA)
1108 imputation was applied to each cell network to reduce the impact of technical zeros due to
1109 potential dropout events (Linderman et al., 2022). NICHES was then run on each cell network
1110 individually, drawing from the OmniPath database of ligand-receptor pairs (Türei et al., 2016) to
1111 generate a cell interaction object whereby rows are ligand-receptor pairs and columns are cell
1112 type pairs (Raredon et al., 2023). These objects were then scaled and passed through principal
1113 component analysis and UMAP dimensionality reduction to generate low-dimensional
1114 embeddings of cell interactions. Differentially expressed interactions were identified using the

1115 Seurat *FindAllMarkers* function, and highly differentially expressed interactions of interest were
1116 selected for display as heatmaps.

1117

1118 **Cluster annotation in memory samples**

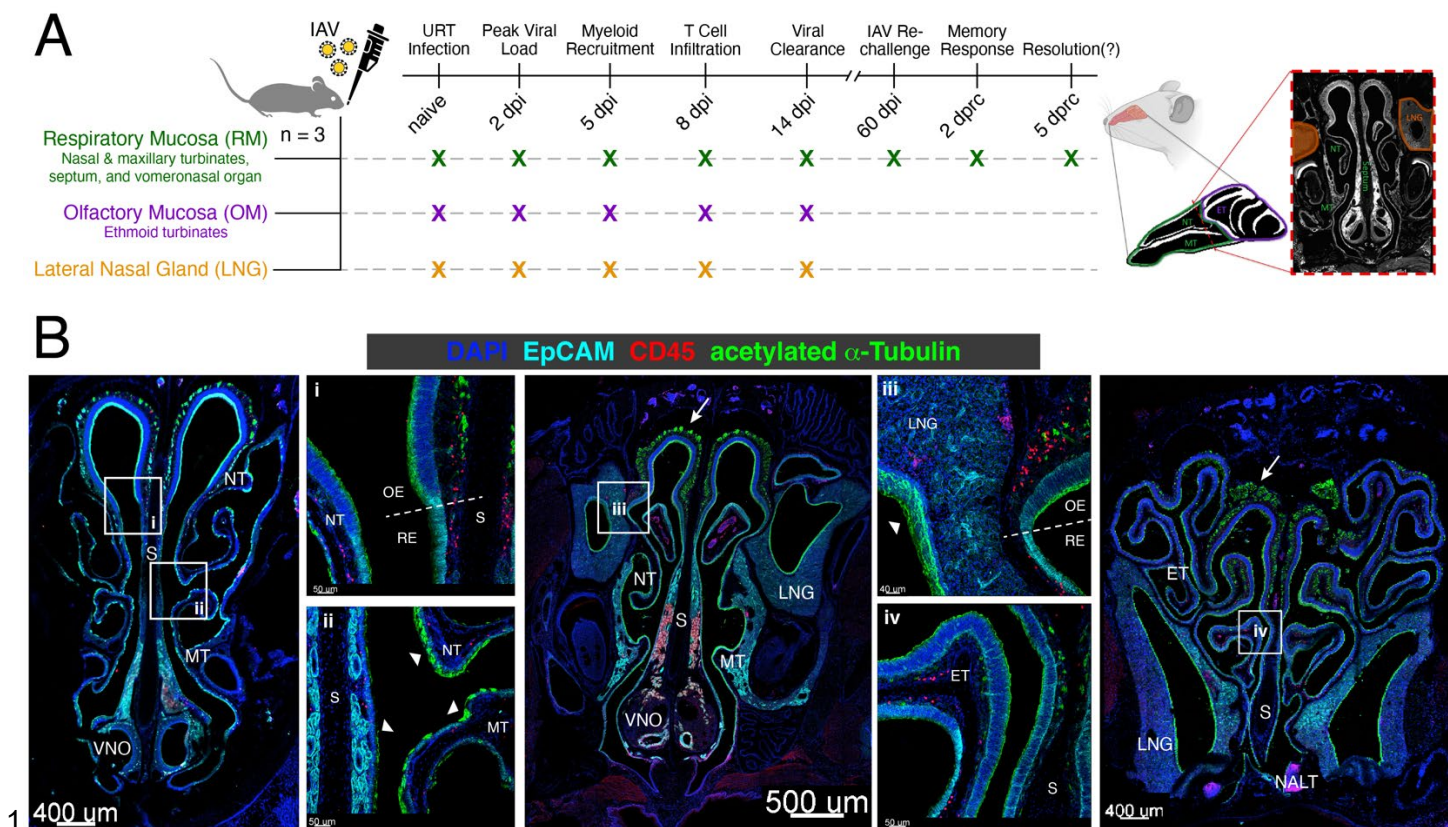
1119 To assign cluster labels to new scRNA-seq datasets generated from the nasal mucosa,
1120 we leveraged the structure of our data to test the label transfer methods provided in Seurat (Hao
1121 et al., 2021) and scANVI (Xu et al., 2021). We separated the cells from one RM replicate from
1122 each time point as a query dataset, using the remaining cells as the reference. With Seurat, we
1123 implemented the *FindTransferAnchors* function on the scTransformed data, using the first 40 PCs
1124 from the PCA as the reference. Labels were then assigned with the *TransferData* function using
1125 either cell cluster or cell type identities. With scANVI, we first built a scVI model on the reference
1126 data, and then a scANVI model using either cell cluster or cell type identities as labels. The
1127 reference scANVI model was then used to train a model on the query data. We calculated the
1128 percentage of correctly called cell labels using each method for both sets of labels and found
1129 calling to be superior on the cell type level. Thus, we next repeated each procedure within each
1130 cell type to learn cell cluster labels and found Seurat to perform better across all cell types (**Figure**
1131 **S9C**). To further validate, we calculated cell cluster abundances using the predicted cell cluster
1132 labels for the query replicates and projected into the PCA calculated across the RM samples.

1133 We next applied the two-step label transfer approach using Seurat to new data generated
1134 from RM 60 dpi and 2 and 5 dprc. Before performing label transfer, we removed all hashtag
1135 annotated cell doublets from the new dataset and applied the same filtering criteria as above. We
1136 next performed *scTransform* and PCA on the new dataset. We then predicted cell type labels
1137 using all cells from RM samples in the primary infection dataset for reference. We next removed
1138 any cells from subsequent analysis that had a maximum assignment score < 0.8 (i.e., 80% is the
1139 greatest confidence in label prediction), making up 5% of the total dataset. Given our loading
1140 strategy and number of intrasample doublets found in the primary infection dataset, we chose a
1141 more stringent cutoff following cell type label prediction. Separating into each cell type and using
1142 the processed data from the matching cell type in the primary infection dataset as reference, we
1143 performed the same procedure. Here, we were more liberal, keeping all cells with a maximum
1144 assignment score ≥ 0.4 since very similar clusters within cell types could receive almost equal
1145 prediction probability (e.g., Resting Basal and Abi3bp Resting Basal). With cell cluster labels
1146 assigned, we then calculated cell cluster abundances as above and performed downstream
1147 differential expression analysis.

1148

1149 **MAIN TEXT FIGURES**

Figure 1



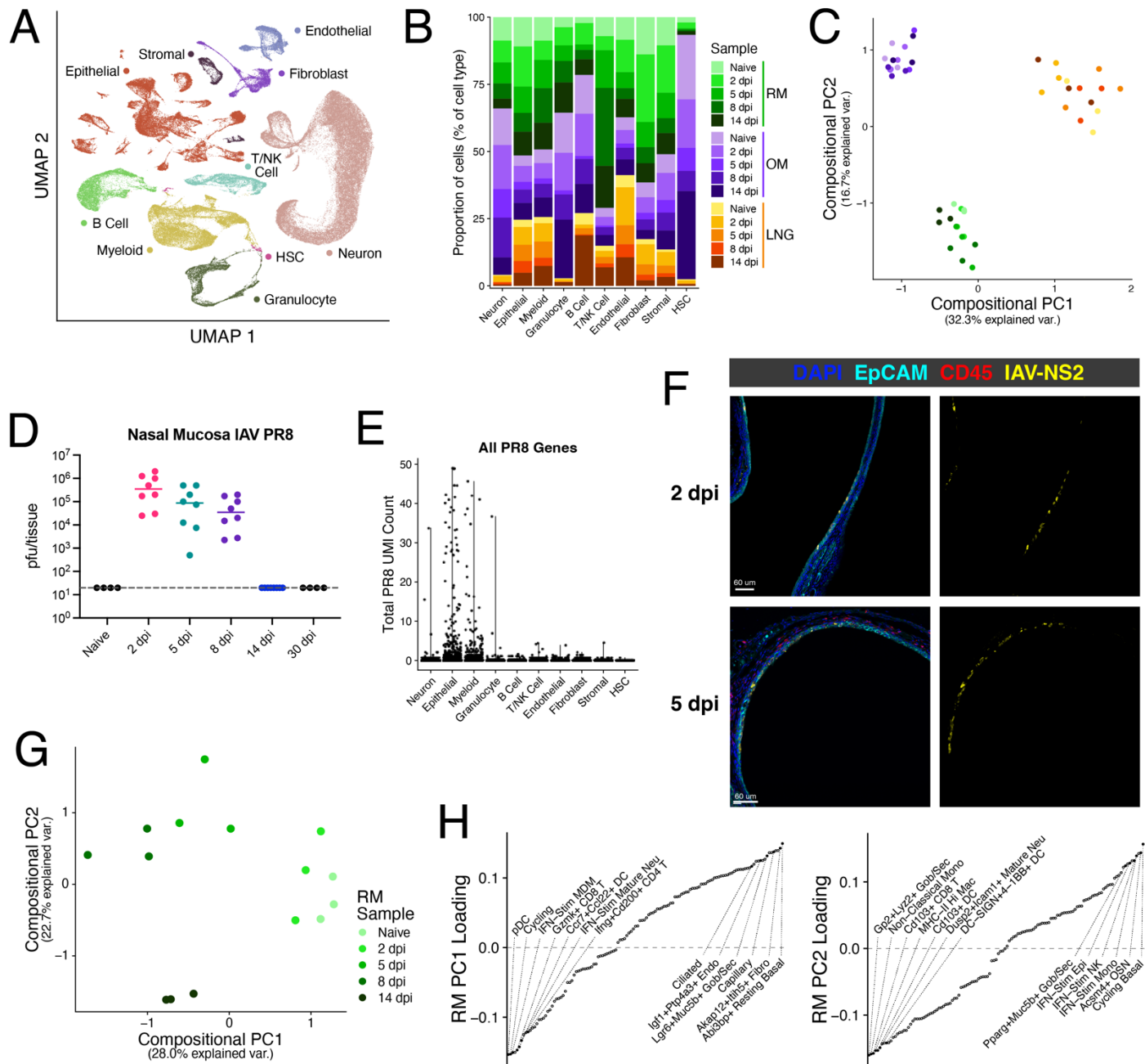
1151 **Figure 1: Experimental design and the structure of the murine nasal mucosa**

1152 (A) Schema depicting the sampling scheme and three tissue regions collected and processed
 1153 for scRNA-seq: respiratory mucosa (RM), olfactory mucosa (OM), and lateral nasal gland
 1154 (LNG). For both primary infection and rechallenge, 10^4 pfu Influenza A Virus (IAV) PR8 was
 1155 administered intranasally ($5\mu\text{l}$ /nostril). dpi = days post infection; dpic = days post rechallenge.

1156 (B) Representative immunofluorescence images of coronal slices of the nasal mucosa from a
 1157 naïve mouse moving from anterior (left) to dorsal (right) staining for epithelial cells (EpCAM,
 1158 teal), immune cells (CD45, red), and ciliated cells/neurons (α -acetylated tubulin, green).
 1159 Distinct regions of the mucosa are labeled. Labeled white boxes outline higher resolution
 1160 images below. White arrows point to olfactory sensory nerve bundles; white arrowheads point
 1161 to cilia. The olfactory epithelium (OE) and respiratory epithelium (RE) both reside within the
 1162 collected RM tissue and are differentiated by morphology and the presence of olfactory
 1163 sensory neurons. NT = nasoturbinate; S = septum; MT = maxillary turbinate; VNO =
 1164 vomeronasal organ; LNG = lateral nasal gland; ET = ethmoid turbinate; NALT = nasal-
 1165 associated lymphoid tissue.

1166

Figure 2

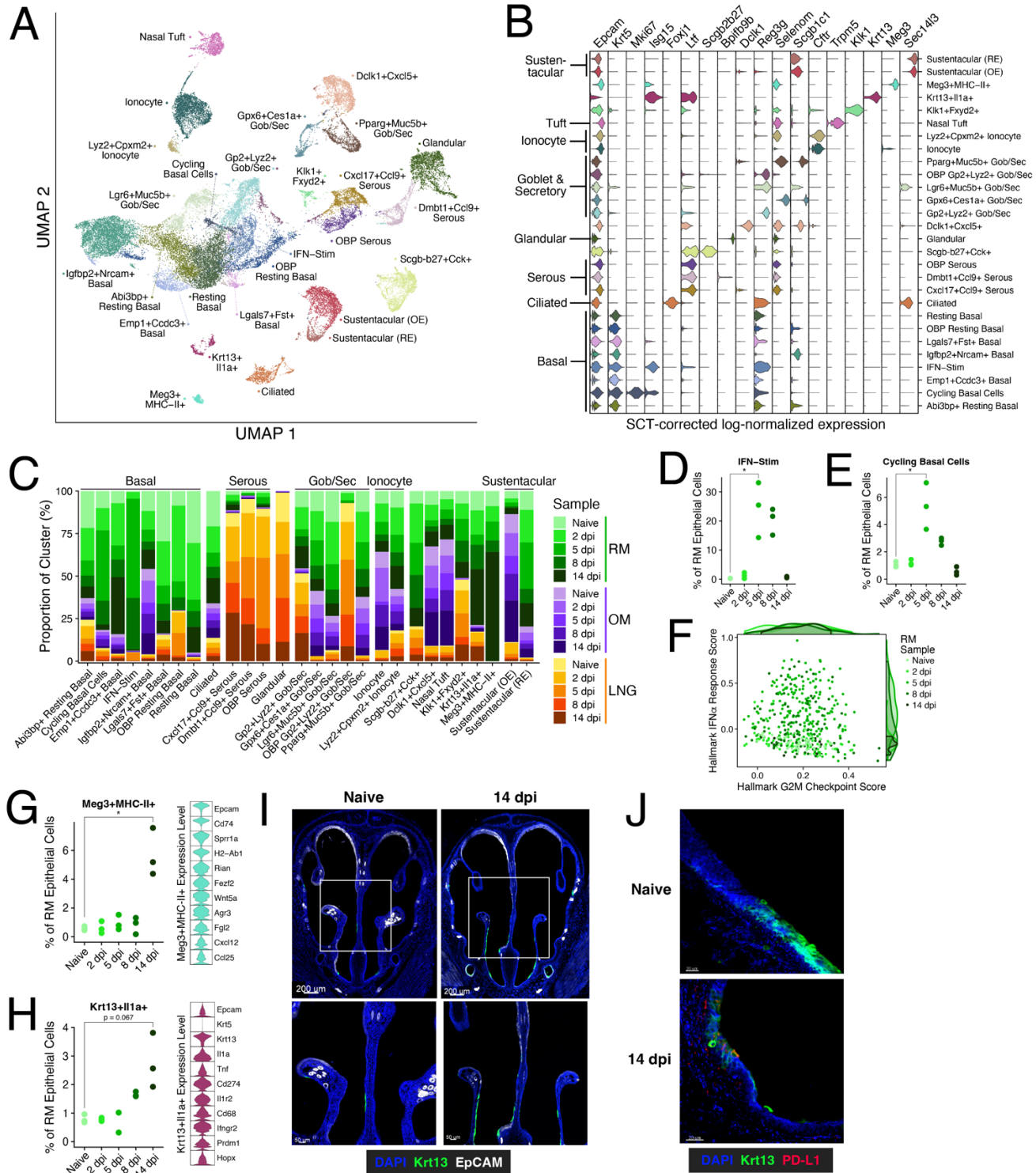


1

1168 **Figure 2: Single-cell atlas of the nasal mucosa during primary IAV infection**
 1169 (A) UMAP embedding of 156,572 nasal cells across three tissue regions and five time points
 1170 (n=3 per region/timepoint) colored by cell type. HSC = hematopoietic stem cell.
 1171 (B) Stacked bar chart depicting the relative proportions of cells annotated for each cell type by
 1172 region and time point.

- 1173 (C) Compositional principal component analysis (PCA) of all acute infection sample replicates.
1174 Each point represents a sample replicate and distance reflects variation in cell cluster
1175 abundance (scaled cell counts). Dots are colored by region and time point as in **B**.
- 1176 (D) Infectious IAV PR8 quantification in plaque forming units (pfu) of the entire nasal mucosa.
- 1177 (E) Summative scTransform-corrected UMI counts per cell across all IAV PR8 genes split by cell
1178 type.
- 1179 (F) Representative images of IAV infection in RM taken from mice 2 dpi (top) and 5 dpi (bottom).
1180 Staining for EpCAM (teal), CD45 (red), and IAV-NS2 (yellow). Images on the right depict only
1181 the signal in the IAV-NS2 channel.
- 1182 (G) Compositional PCA of all cell clusters from only RM samples.
- 1183 (H) Cell cluster abundance loadings for PC1 (left) and PC2 (right) from (G). Cell cluster names
1184 for several of the most negative and most positive weights for each PC are depicted.
1185

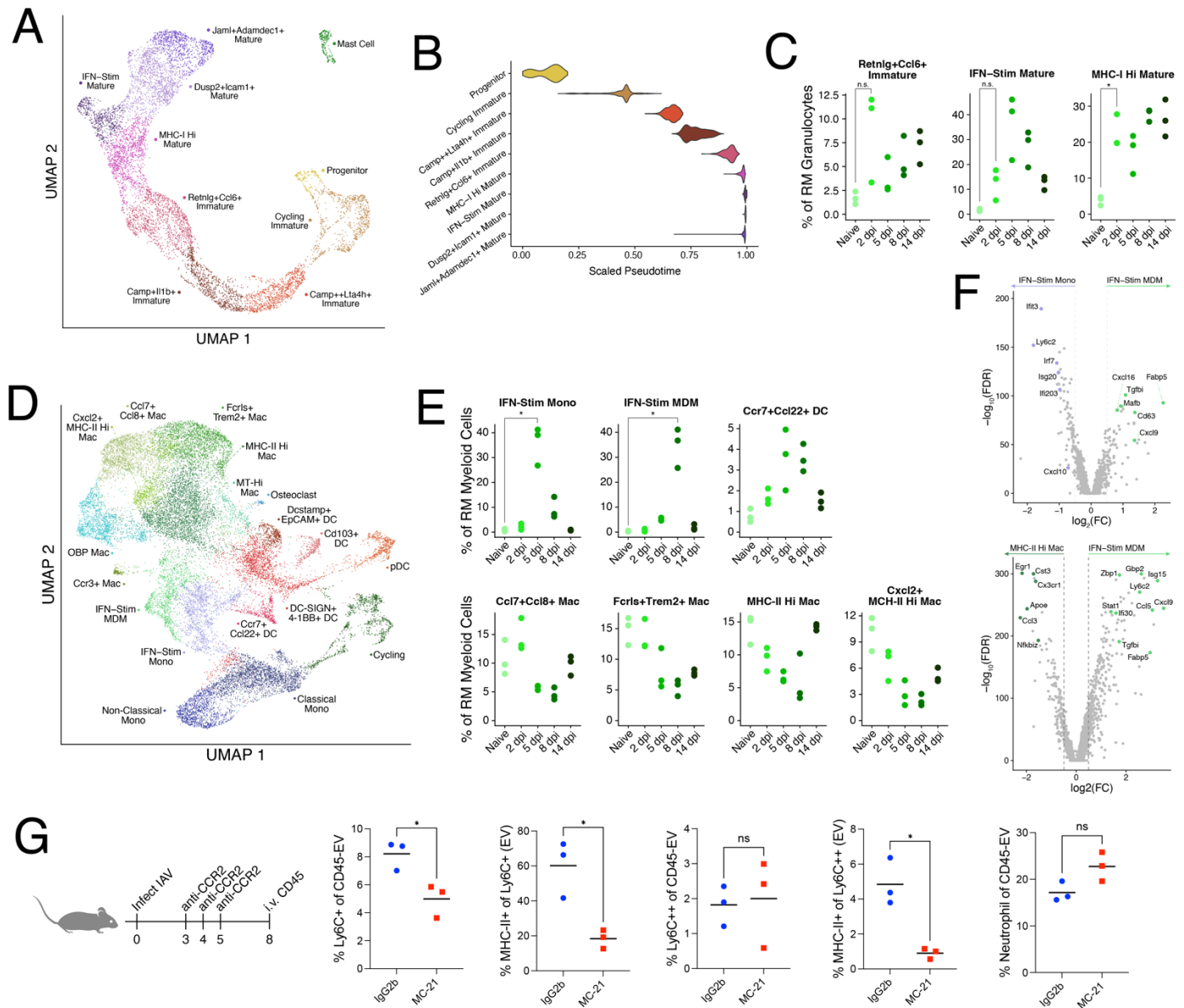
Figure 3



1
 1187 **Figure 3: Epithelial cell subclustering reveals diverse subsets including transient IFN-**
 1188 **responsive/cycling cells and rare cells with immune-interaction potential arising 14 dpi**
 1189 (A) UMAP embedding of 38,367 epithelial cells across 27 clusters.

- 1190 (B) Violin plot depicting epithelial lineage and subset marker expression levels (scTransform-
1191 corrected log-normalized UMI counts) across all discovered clusters (see **Supplementary**
1192 **Table 1**).
- 1193 (C) Stacked bar chart depicting the relative proportions of cells annotated for each cluster by
1194 region and time point.
- 1195 (D & E) Relative frequencies of cells clustered as IFN-Stim (D) and Cycling Basal (E) as a
1196 proportion of all epithelial cells per replicate RM sample. Only cells with assigned hash calls
1197 are included. Welch's t test, * $p < 0.05$.
- 1198 (F) Scatter plot of gene module scores for the Hallmark IFN α Response and Hallmark G2M
1199 Checkpoint gene lists (MsigDB v7.5.1) in cycling basal cells. Density plots represent the
1200 scatter plot data.
- 1201 (G & H) Relative frequency plots of *Meg3*+MHC-II+ (G) and *Krt13*+*Il1a*+ (KNIIFE cells) (H) clusters
1202 (left) as a proportion of all epithelial cells per replicate RM sample. Violin plots of select cluster
1203 specific/enriched genes, except for *Krt5* (FDR corrected p-values $\leq 10^{-242}$ by 1-vs-rest
1204 Wilcoxon Rank Sum Test) (right).
- 1205 (I) Representative immunofluorescence images of the very anterior nasal mucosa in naïve mice
1206 (left) and 14 dpi (right) staining for Krt13 (green) and EpCAM (white).
- 1207 (J) Representative images within the region shown in (I) in naïve mice (top) and 14 dpi (bottom)
1208 staining for Krt13 (green) and PD-L1 (red). Welch's t test, * $p < 0.05$.
1209

Figure 4



1

1211 **Figure 4: Immediate neutrophil responses are bolstered by recruited antiviral monocytes**
 1212 **that differentiate into antiviral monocyte-derived macrophages**

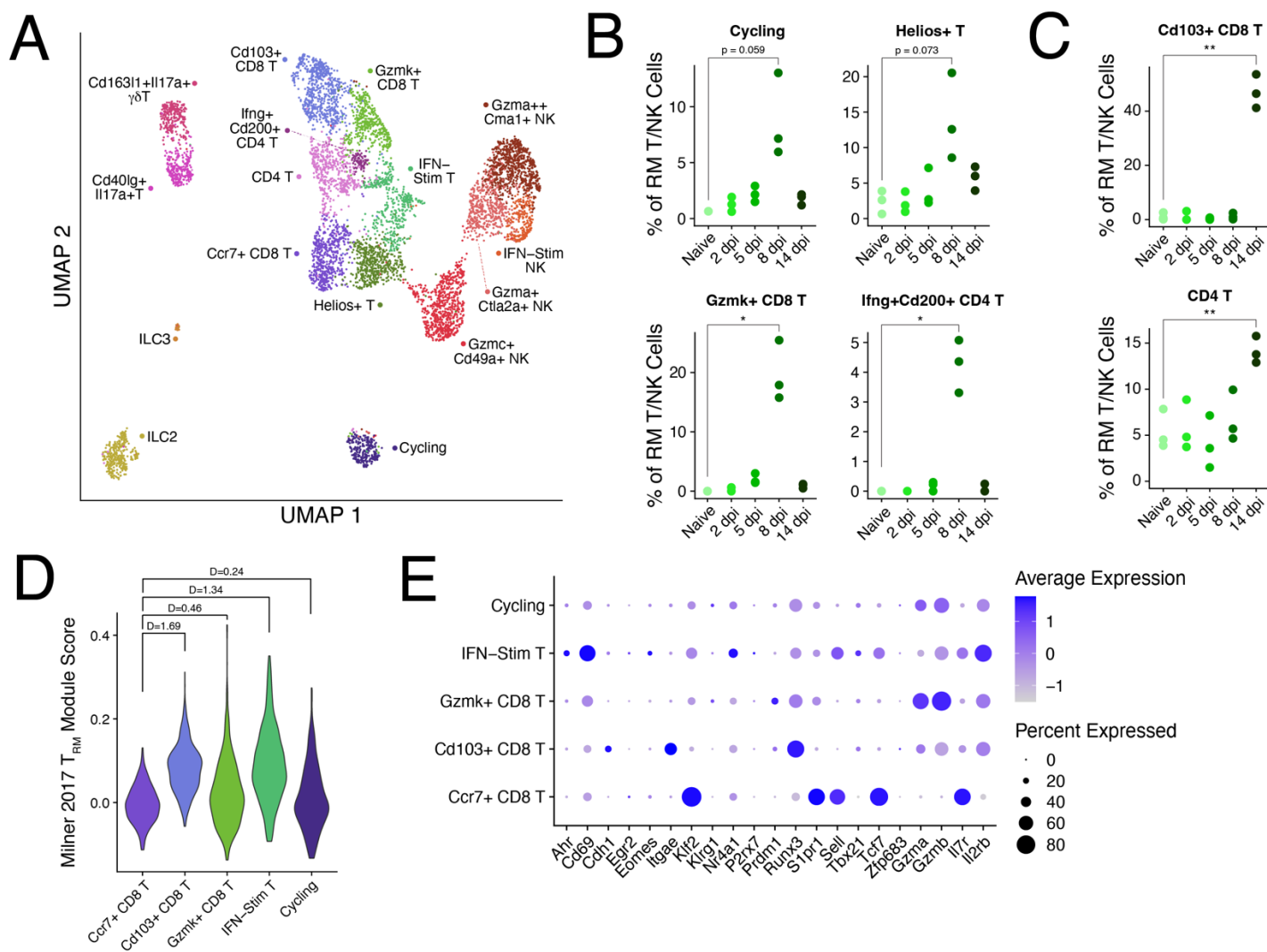
1213 (A) UMAP embedding of 7,987 granulocytes across 10 clusters.

1214 (B) Violin plot of assigned pseudotime values to all granulocytes (except mast cells) split by
 1215 cluster identity.

1216 (C) Relative frequencies of various neutrophil clusters as a proportion of all granulocytes per
 1217 replicate RM sample. Only cells with assigned hash calls are included. Welch's t test, *p <
 1218 0.05.

- 1219 (D) UMAP embedding of 22,654 macrophages, monocytes, and dendritic cells (DCs) across 17
1220 clusters.
- 1221 (E) Relative frequencies of various myeloid cell clusters as a proportion of all macrophages,
1222 monocytes, and DCs per replicate RM sample. Welch's t test, *p < 0.05.
- 1223 (F) Volcano plots depicting differentially expressed genes ($|\log_2FC| \geq 0.5$; FDR < 0.01) between
1224 IFN-Stim MDMs and IFN-Stim Mono (top) and between IFN-Stim MDMs and MHC-II-Hi Macs
1225 (bottom). Only cells from RM were used in the differential expression analysis. Genes of
1226 interest are labeled.
- 1227 (G) Mice were infected with 10^4 pfu IAV PR8 and then treated 3, 4, and 5 dpi with either MC-21
1228 (anti-CCR2; n=3) or IgG2b (isotype control; n=3). At 8 dpi mice received anti-CD45
1229 intravascularly immediately prior to euthanasia to distinguish cells in the tissue
1230 (extravascular, EV) from those in circulation (IV). Flow cytometry statistics are gated on
1231 CD45-EV+ cells; Welch's t test, *p < 0.05.
1232

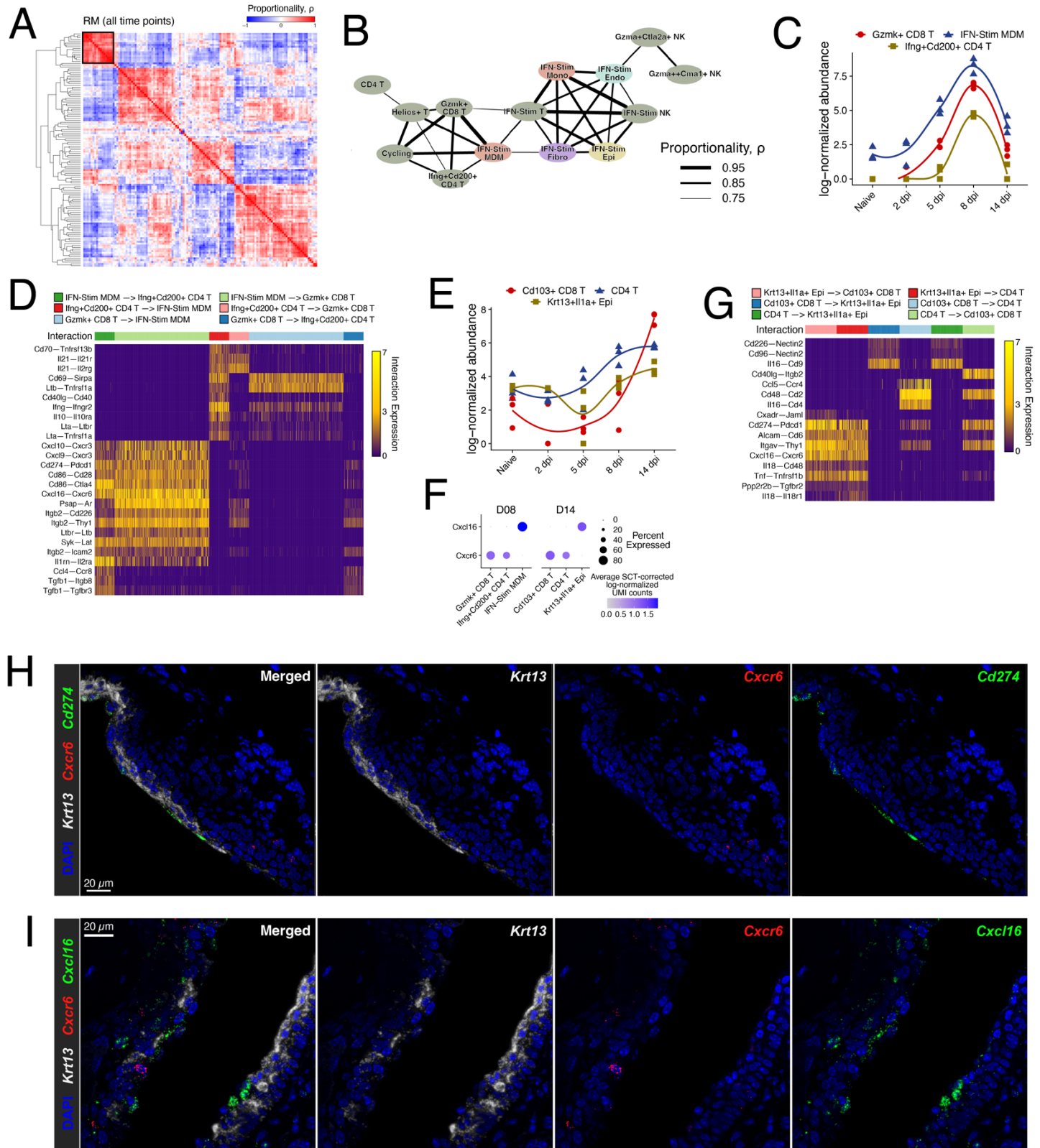
Figure 5



1
 1234 **Figure 5: Effector CD4 and CD8 T cells 8 dpi are replaced by T_{RM} cells following viral**
 1235 **clearance**
 1236 (A) UMAP embedding of 6,573 T, NK, and innate lymphoid cells across 16 clusters.
 1237 (B & C) Relative frequencies of various T cell clusters as a proportion of all T and NK cells per
 1238 replicate RM sample. Only cells with assigned hash calls are included.
 1239 (D) Violin plot depicting a gene module score derived from the universal T_{RM} signature as
 1240 published in (Milner et al., 2017) across all CD8 T cell clusters for cells collected from RM.
 1241 Cohen's D for effect size is reported between Ccr7+ CD8 T cells and each other cluster.
 1242 Welch's t test, *p < 0.05, **p < 0.01.

1243 (E) Dot plot of genes encoding for canonical surface markers, proteases, and transcription
1244 factors enriched or absent in T_{RM} cells from circulating memory and naïve CD8 T cells. Gene
1245 list derived from (Crowl et al., 2022).
1246

Figure 6



1...

1248 **Figure 6: Proportionality and cell-cell communication analyses highlight the CXCL16–**
1249 **CXCR6 signaling pathway in T cell:MDM and T cell:KNIIFE cell interactions**

1250 (A) Hierarchically clustered similarity heatmap of sample replicate proportionality calculated
1251 across all RM primary infection time points. Black box surrounds the proportionality results
1252 for the cell clusters depicted in (B).

1253 (B) Network of significantly proportional (FDR<0.01) cell clusters as in (A). Nodes are colored by
1254 cell type and edge weight is representative of proportionality.

1255 (C) Abundance plot of *Gzmk*+ CD8 T cells, IFN-Stim MDMs, and *Ifng*+*Cd200*+ CD4 T cells in
1256 replicate RM samples. Smoothed lines are calculated using local polynomial regression
1257 fitting.

1258 (D) Heatmap depicting a subset of differentially expressed receptor-ligand interaction pairs
1259 between single-cell pairs identified by NICHES (Raredon et al., 2023) for the clusters
1260 depicted in (C); see **Supplementary Table 2**. Interaction expression is the multiplicative
1261 expression of receptor and ligand gene expression for each member of a single-cell pair. See
1262 for all receptor-ligand interaction pairs.

1263 (E) Abundance plot of *Cd103*+ CD8 T cells, CD4 T cells, and *Krt13*+*Il1a*+ epithelial (KNIIFE)
1264 cells in replicate RM samples.

1265 (F) Dot plot of scTransform-corrected log-normalized *Cxcl16* and *Cxcr6* expression 8 dpi (left) in
1266 the clusters depicted in (C) and 14 dpi (right) in the clusters depicted in (E).

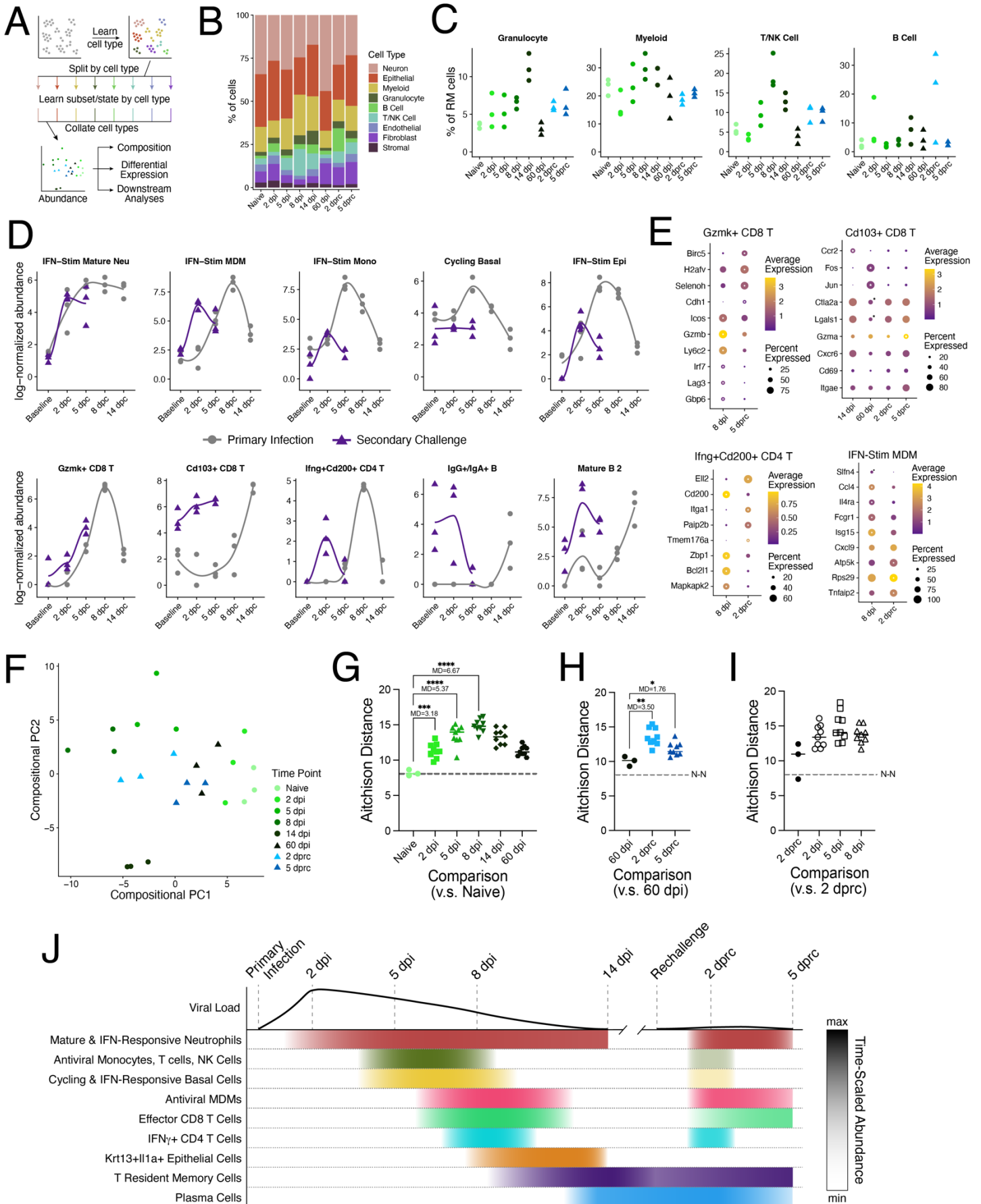
1267 (G) Heatmap like (D) for the clusters shown in (E).

1268 (H) Representative RNAscope in situ staining for *Krt13* (gray), *Cxcr6* (red), and *Cd274* (i.e., PD-
1269 L1; green) of the nasal floor 14 dpi. Images depict a maximal intensity projection across 5
1270 μm (10 slices) in the z-plane.

1271 (I) RNAscope as in (H) staining with *Krt13* (gray), *Cxcl6* (red), and *Cxcl16* (green). Here,
1272 maximal intensity projection is across 3 μm (6 slices) in the z-plane.

1273

Figure 7



1275 **Figure 7: IAV rechallenge induces accelerated and coordinated memory immune**
1276 **responses**

1277 (A) Analysis scheme applied to RM samples collected 60 dpi and 2 and 5 days post IAV
1278 rechallenge (dprc) to learn cell cluster identity.

1279 (B) Stacked bar chart depicting the relative proportions of cells annotated for each cell type
1280 by time point. Cells from RM samples only.

1281 (C) Relative frequencies of immune cell types as a proportion of all sequenced cells per RM
1282 replicate sample in primary infection and following rechallenge.

1283 (D) Abundance plots of various clusters showing overlaid primary infection (gray) and
1284 rechallenge (purple) responses. Baseline refers to samples from naïve mice in primary
1285 infection and to samples from 60 dpi in rechallenge. dpc = days post challenge. Smoothed
1286 lines are calculated using local polynomial regression fitting.

1287 (E) Dot plots depicting select cluster-specific and differentially expressed genes between
1288 primary infection and rechallenge time points in *Gzmk*⁺ CD8 T cells (top left), *Cd103*⁺
1289 CD8 T cells (top right), *Ifng*⁺*Cd200*⁺ CD4 T cells (bottom left), and IFN-Stim MDMs
1290 (bottom right). Time points were chosen from peak responses in each challenge.
1291 Significantly enriched (white star) or decreased (black star) genes are labeled at each
1292 timepoint (FDR<0.01). See **Supplementary Table 3** for all differentially expressed genes
1293 in each comparison.

1294 (F) Compositional PCA of both primary infection and secondary challenge RM sample
1295 replicates. Here, secondary challenge samples were projected into the PC space
1296 calculated across only primary infection samples (see **Figure 2F**).

1297 (G, H, & I) Euclidean distances calculated between center log ratio transformed abundance
1298 values (Aitchison distance). The farther the Aitchison distance between two sample
1299 replicates, the less similar their compositions. (G) All pairs of naïve replicates and primary
1300 infection + 60 dpi replicates. (H) All pairs of 60 dpi replicates and rechallenge replicates.
1301 (I) Pairs of replicates between 2 dprc and 2, 5, and 8 dpi. Dotted line plotted at the median
1302 naïve-naïve Aitchison distance (N-N). P values reported for multiple hypothesis corrected
1303 Welch's ANOVA. MD = mean difference; *p<0.05; **p<0.01; ***p<0.001, ****p< 0.0001.

1304 (K) Timeline schematic of primary IAV infection and rechallenge depicting viral load trajectory
1305 and immune and epithelial cell cluster response timing and duration.

1306

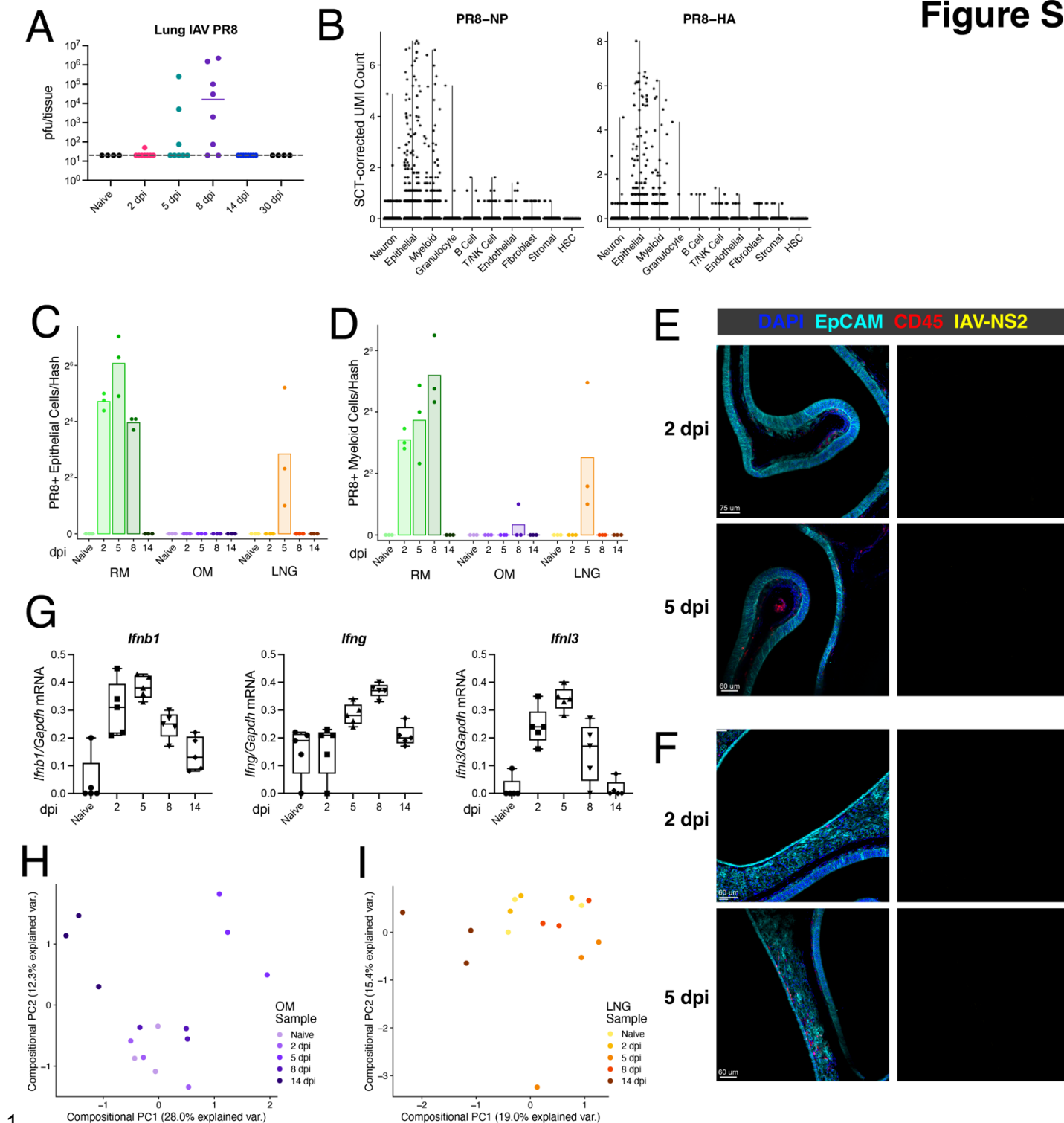
1307 ***SUPPLEMENTARY MATERIAL***

1309 **Figure S1: Clustering and sample replicate assignment across nasal mucosa regions and**
1310 **cell types**

- 1311 (A) Violin plots of representative genes used to assign cell type identity to clusters.
1312 (B) Numbers of cells classified as each cell type across all samples, including cells that did not
1313 receive a hash call.
1314 (C) UMAP embedding as in **Figure 2A** colored by region and time point.
1315 (D) UMAP as in (D) colored by hash call assignment. There are 45 sample replicates across the
1316 dataset in addition to cells without definitive hash identities (“Unassigned”).
1317 (E) Stacked bar chart depicting the relative proportion of cells with assigned sample replicate
1318 identity (i.e., hash call) by cell type. Singlet = single sample replicate call; unknown = too few
1319 barcodes measured to assign a sample replicate identity.
1320 (F) Cell lineage tree generated with ARBOL (Zheng et al., 2021) depicting all 127 clusters found
1321 in the dataset through cell type subclustering. Branches are colored by cell type. Pie charts
1322 at each branching point depict the relative proportion of cells from each nasal mucosa region.
1323 Dot size at each end node is proportional to the number of cells assigned to that cluster. See
1324 **Supplementary Table 1** for all differentially expressed markers across clusters within each
1325 cell type.
1326 (G) Cell cluster abundance loadings from the PCA shown in **Figure 2C** for PC1 (left) and PC2
1327 (right) from (F). Cell cluster names for several of the most negative and most positive weights
1328 for each PC are depicted.

1329

Figure S2



1331 **Figure S2: Viral transcript capture, global antiviral responses, and changes in OM and LNG**
 1332 **composition**

1333 (A) Infectious IAV PR8 quantification in plaque forming units (pfu) of the entire lung.

1334 (B) scTransform-corrected UMI counts for the IAV PR8 genes encoding NP (left) and HA (right)
1335 by cell type.

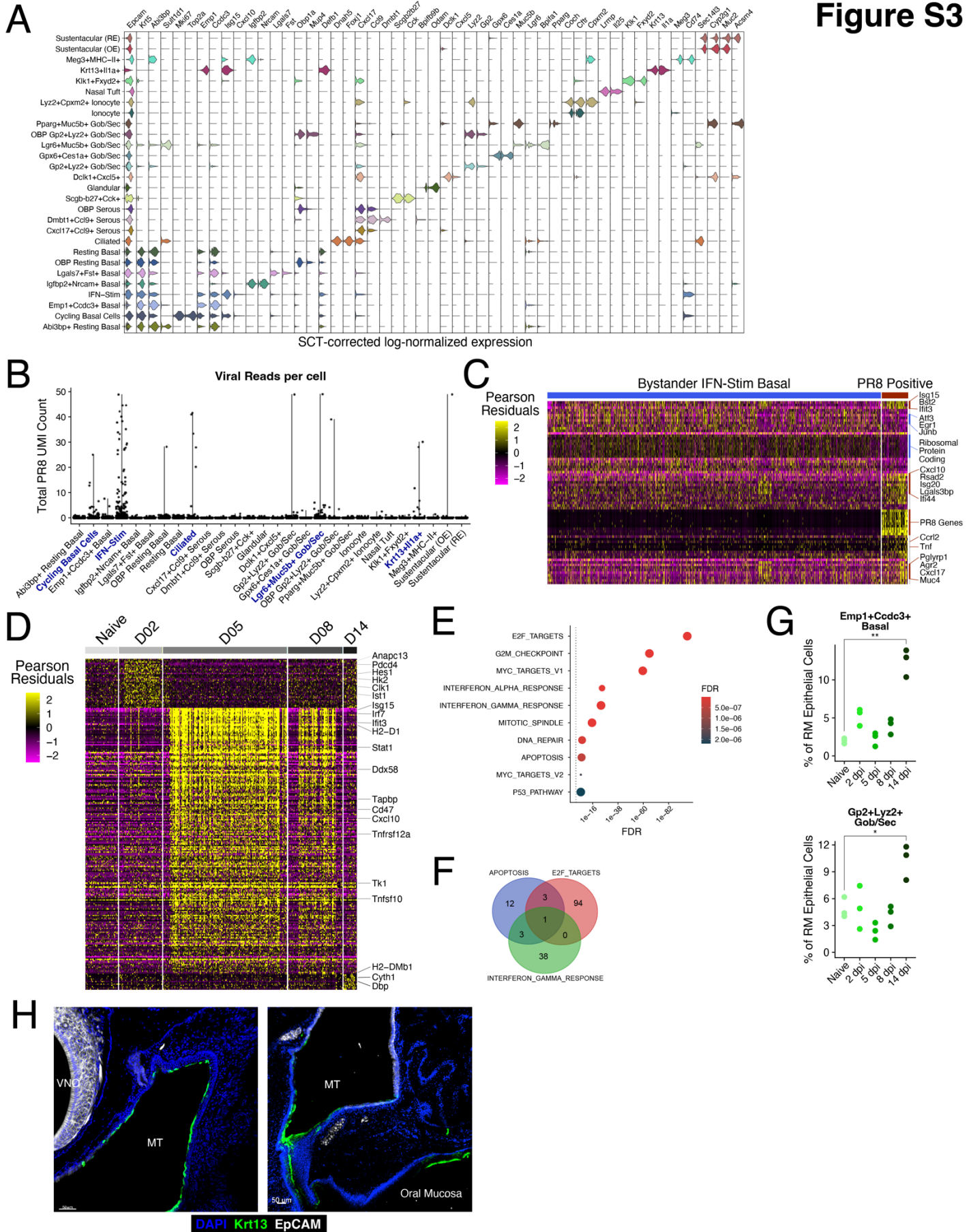
1336 (C & D) Number of PR8+ epithelial cells (D) and myeloid cells (E) by time point and region. PR8+
1337 cells are classified by having at least 2 UMI aligning to PR8 genes.

1338 (E & F) Representative images of IAV infection in OM (E) and LNG (F) taken from mice 2 dpi (top)
1339 and 5 dpi (bottom). Staining for EpCAM (teal), CD45 (red), and IAV-NS2 (yellow). Images on
1340 the right depict only the signal in the IAV-NS2 channel.

1341 (G) qPCR of *Ifnb1* (left), *Ifng* (center), and *Ifnl3* from RNA extracted from RM tissue. C_q ratios are
1342 normalized by *Gapdh* C_q. n = 5 per time point.

1343 (H & I) Compositional PCA of only OM samples (H) and only LNG samples (I).
1344

Figure S3

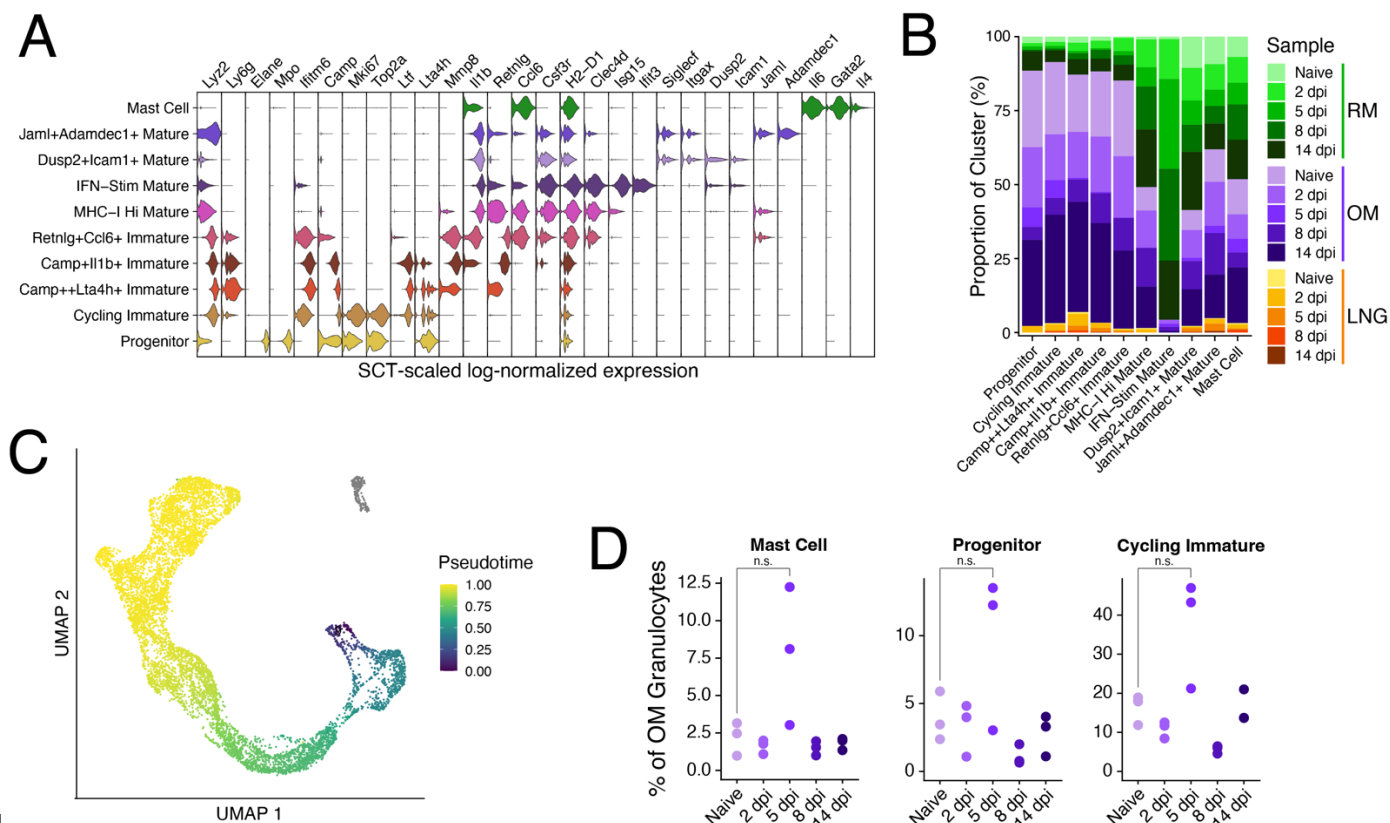


1346 **Figure S3: Epithelial cell heterogeneity and response cluster dynamics**

- 1347 (A) Violin plots depicting differentially expressed marker genes (FDR<0.01) across all 28
1348 epithelial clusters (see **Supplementary Table 1**).
- 1349 (B) Summative scTransform-corrected UMI counts across all 8 IAV genes by epithelial cell
1350 cluster. Clusters with ≥ 5 cells with more than 2 PR8 UMIs have their cluster names bolded
1351 in blue.
- 1352 (C) Heatmap depicting all differentially expressed genes between PR8 positive (≥ 2 PR8 UMIs)
1353 and bystander IFN-Stim epithelial cells from RM 5 and 8 dpi. Scaled Pearson residuals from
1354 scTransform are plotted.
- 1355 (D) Heatmap depicting all differentially expressed genes (FDR<0.01) in Cycling Basal cells from
1356 RM between timepoints. Scaled Pearson residuals from scTransform are plotted.
- 1357 (E) Gene set analysis (hypergeometric test) of all differentially enriched genes in Cycling Basal
1358 cells compared to all other epithelial cell clusters (FDR<0.01). The Hallmark pathways from
1359 MsigDB (v7.5.1) were used.
- 1360 (F) Venn diagram showing the number genes used in (E) that are within the Hallmark Apoptosis,
1361 E2F Targets, and Interferon Gamma Response pathways.
- 1362 (G) Relative frequencies of *Emp1+Ccdc3+* basal cells (top) and *Gp2+Lyz2+* Gob/Sec cells
1363 (bottom) as a proportion of all epithelial cells per replicate RM sample. Only cells with
1364 assigned hash calls are included. Welch's t test, *p < 0.05, **p < 0.01.
- 1365 (H) Representative immunofluorescence images of the nasal mucosa 14 dpi taken more
1366 posterior than **Figure 3H** where the nasal mucosa connects to the oral cavity.

1367

Figure S4



1

1369 **Figure S4: Granulocyte heterogeneity**

1370 (A) Violin plots depicting differentially expressed marker genes (FDR<0.01) across all 10
1371 granulocyte clusters (see **Supplementary Table 1**).

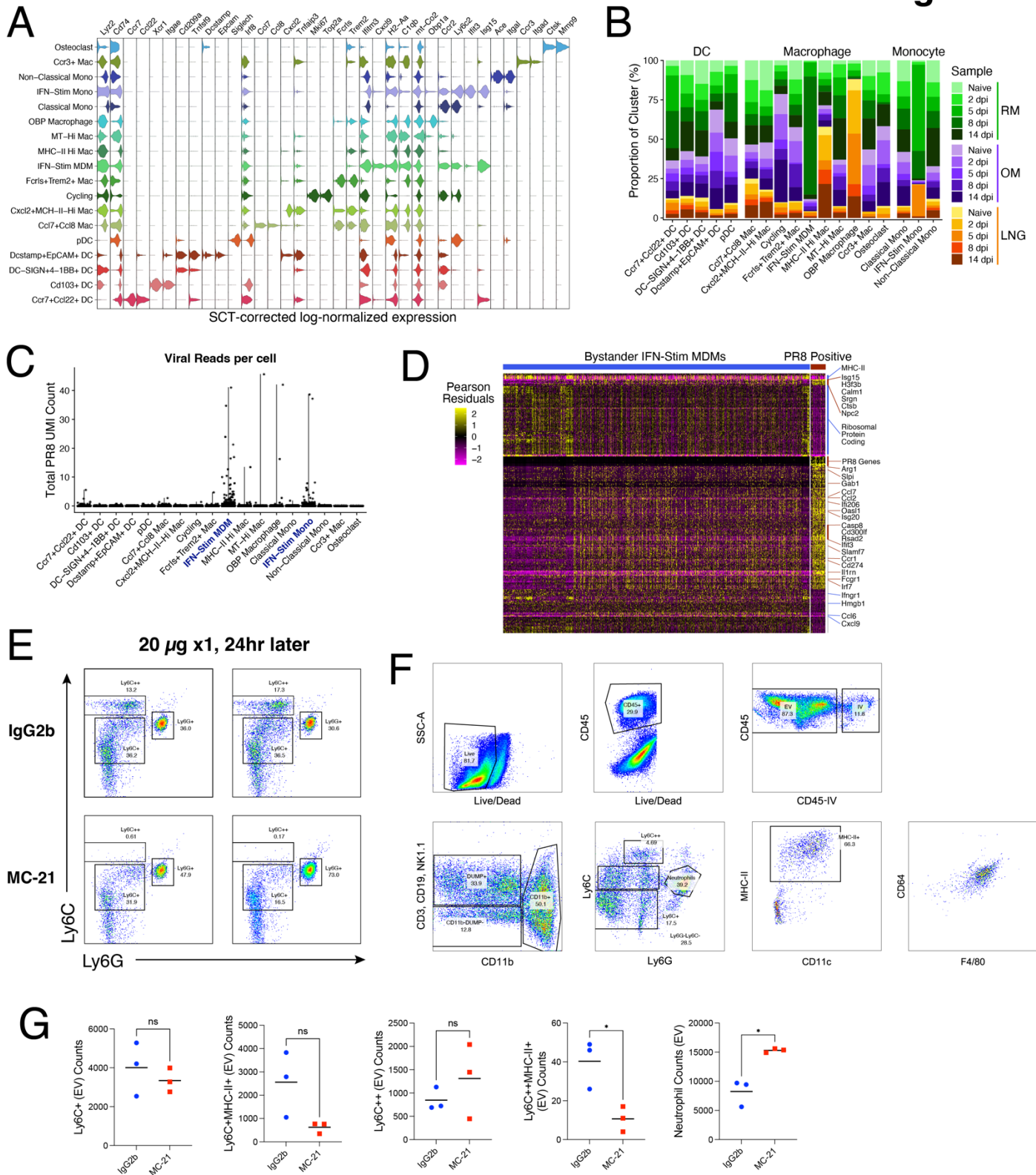
1372 (B) Stacked bar chart depicting the relative proportions of cells annotated for each granulocyte
1373 cluster by region and time point.

1374 (C) UMAP of granulocytes colored by pseudotime. Mast Cells were not included in the
1375 pseudotime analysis and are colored gray.

1376 (D) Relative frequencies of Mast cells (left), progenitors (center), and cycling immature (right) as
1377 a proportion of all granulocytes per replicate OM sample.

1378

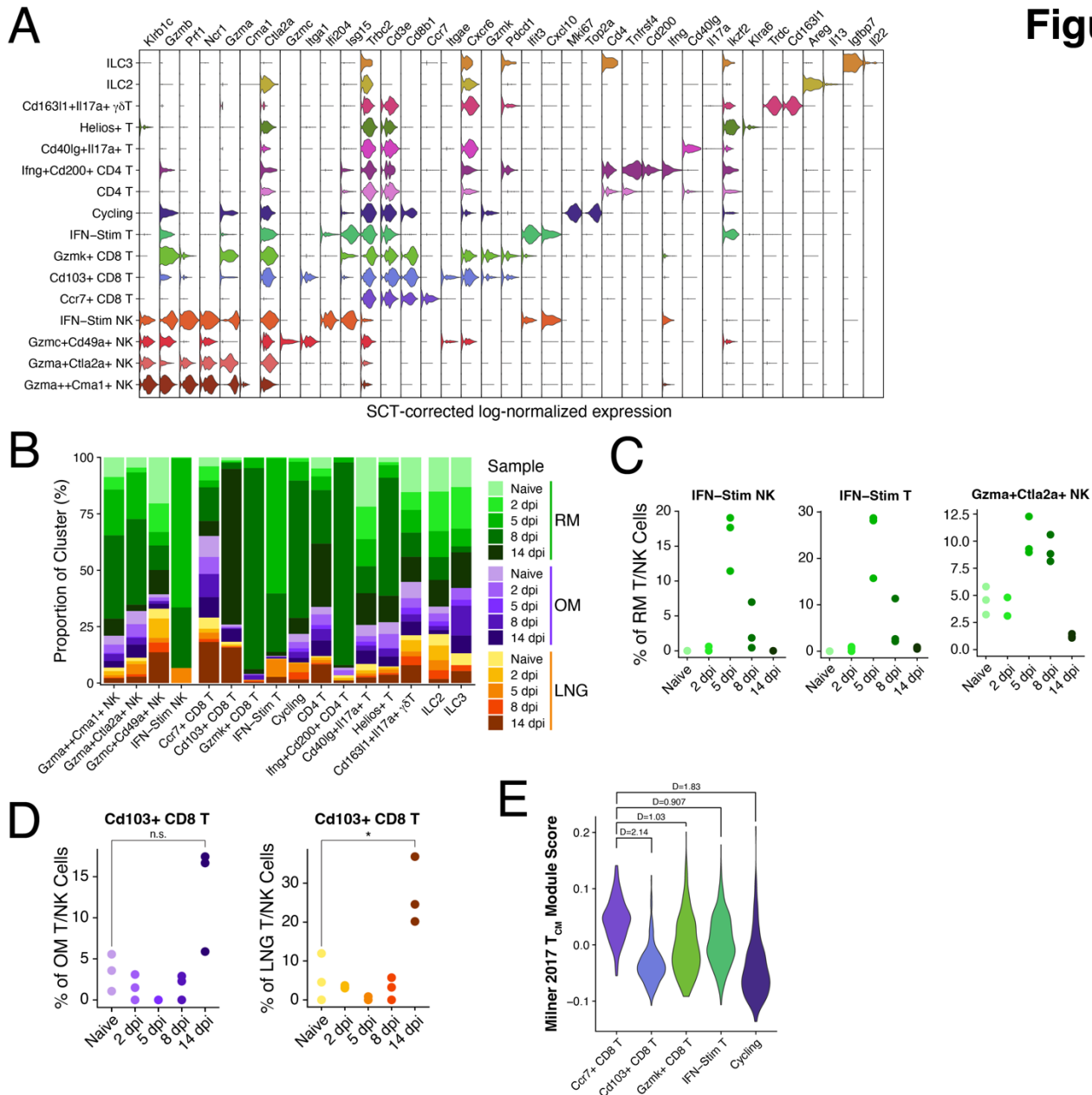
Figure S5



1381 **Figure S5: Myeloid heterogeneity, viral+ cells, and monocyte depletion**

- 1382 (A) Violin plots depicting differentially expressed marker genes (FDR<0.01) across all 18
1383 macrophage, monocyte, and DC clusters (see **Supplementary Table 1**).
- 1384 (B) Stacked bar chart depicting the relative proportions of cells annotated for each myeloid
1385 cluster by region and time point.
- 1386 (C) Summative scTransform-corrected UMI counts across all 8 IAV genes by myeloid cell cluster.
1387 Clusters with ≥ 5 cells with more than 2 PR8 UMIs have their cluster names bolded in blue.
- 1388 (D) Heatmap depicting all differentially expressed genes between PR8 positive (≥ 2 PR8 UMIs)
1389 and bystander IFN-Stim MDMs from RM 8 dpi. Scaled Pearson residuals from scTransform
1390 are plotted.
- 1391 (E) Mice (n = 4) were treated i.p. with control antibody (top) or anti-CCR2 antibody (bottom) and
1392 blood was collected 24 hours later for flow cytometry. Pre-gated on Dead-CD45+CD3-
1393 CD19-CD11b+.
- 1394 (F) Representative gating scheme for Ly6C+ and Ly6C++ monocytes in the nasal mucosa.
- 1395 (G) Cell counts for the experiment performed in **Figure 4G**; Welch's t test, *p < 0.05.
1396

Figure S6



1

1398 **Figure S6: T cell, NK cell, and innate lymphocyte heterogeneity and T_{RM} responses**

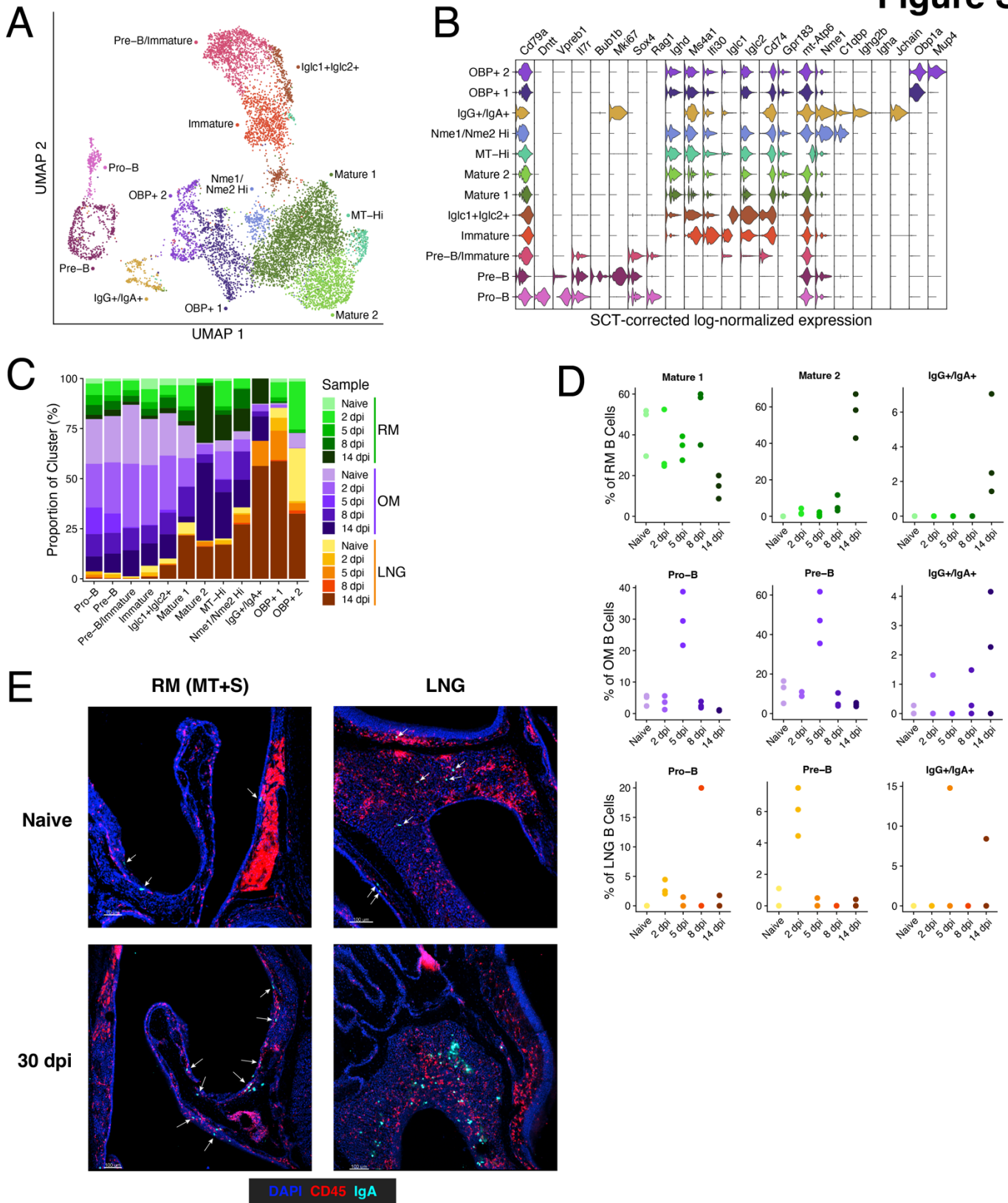
1399 (A) Violin plots depicting differentially expressed marker genes (FDR<0.01) across all 16 T cell,
1400 NK cell, and innate lymphocyte cell clusters (see **Supplementary Table 1**).

1401 (B) Stacked bar chart depicting the relative proportions of cells annotated for each myeloid
1402 cluster by region and time point.

1403 (C) Relative frequencies of IFN-Stim NK cells (left), IFN-Stim T cells (middle), and
1404 *Gzma+Ctla2a+* NK cells (right) as a proportion of all T cells, NK cells, and innate lymphocytes
1405 per RM replicate sample.

1406 (D) Relative frequencies of *Cd103*+ CD8 T cells as a proportion of all T cells, NK cells, and innate
1407 lymphocytes per OM replicate sample (left) and LNG replicate sample (right).
1408 (E) Violin plot depicting a gene module score derived from the universal T circulating memory
1409 (T_{CM}) cell signature as published in (Milner et al., 2017) across all CD8 T cell clusters.
1410 Cohen's D for effect size is reported between *Ccr7*+ CD8 T cells and each other cluster.
1411

Figure S7



1413 **Figure S7: B cell heterogeneity and cluster dynamics**

1414 (A) UMAP embedding of 10,167 B cells across 12 clusters.

1415 (B) Violin plots depicting differentially expressed marker genes (FDR<0.01) across all 12 B cell
1416 clusters (see **Supplementary Table 1**).

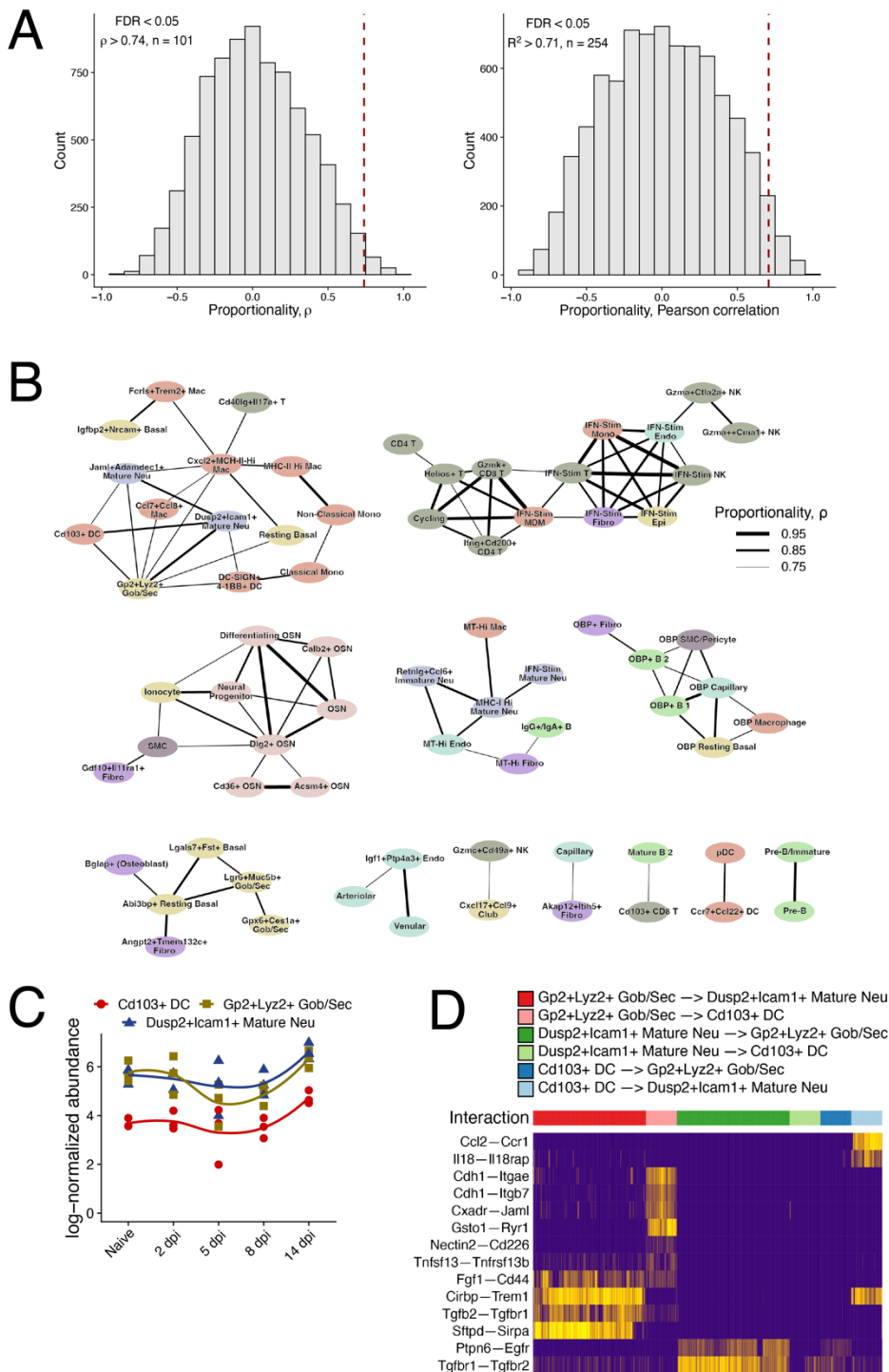
1417 (C) Stacked bar chart depicting the relative proportions of cells annotated for each B cell cluster
1418 by region and time point.

1419 (D) Relative frequencies of several B cell clusters as proportions of all B cells per RM replicate
1420 sample (top), OM replicate sample (middle), and LNG replicate sample (bottom).

1421 (E) Representative immunofluorescence images staining for IgA producing cells in the RM (left)
1422 and LNG (right) in naïve mice (top) and 30 dpi (bottom). White arrows point to IgA+ cells in
1423 the sparser images.

1424

Figure S8

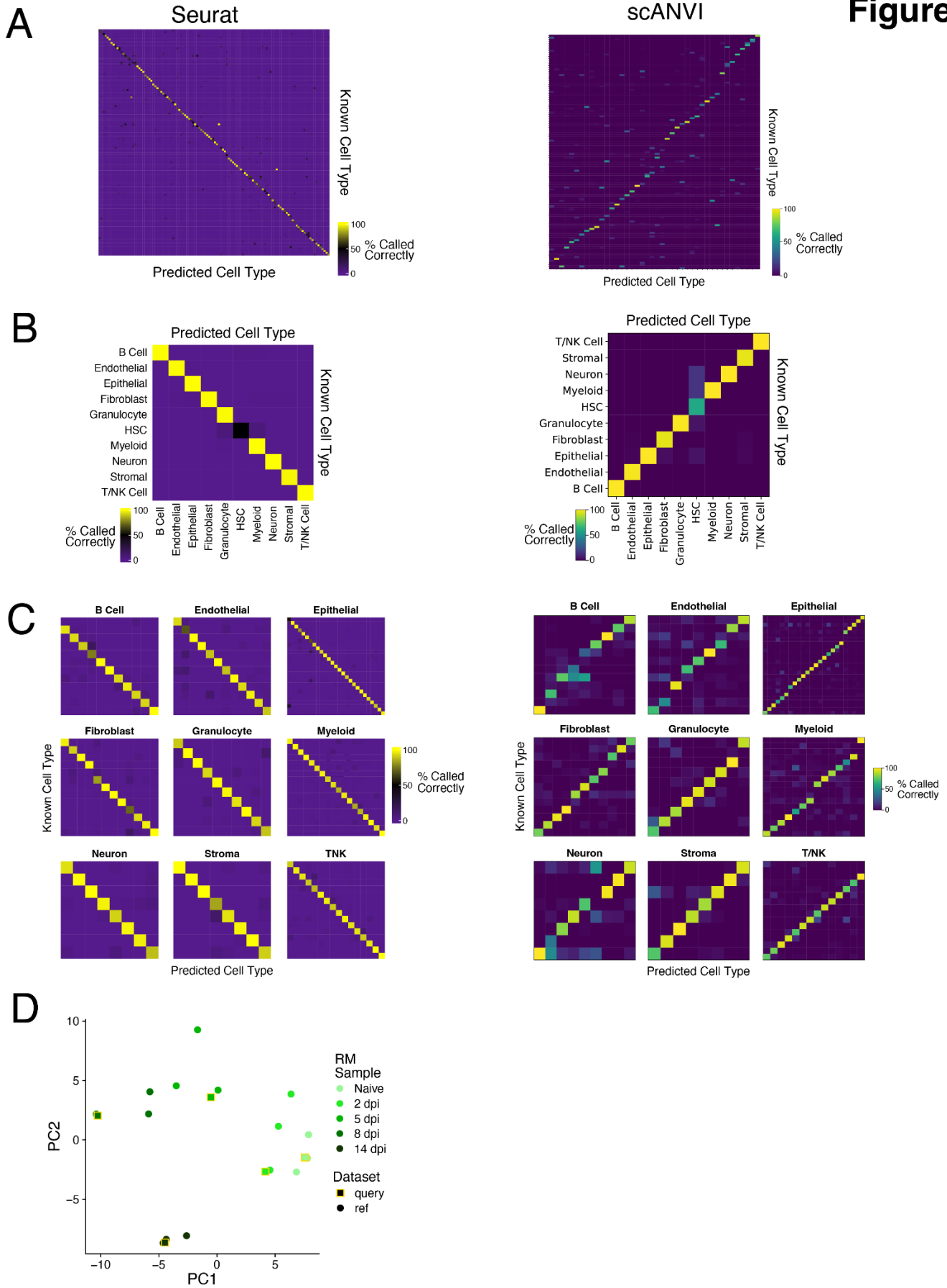


1. **Figure S8: Proportionality and cell-cell communication analysis**

1426 (A) Histograms of calculated proportionality (left) and Pearson correlation (right) statistics across
 1427 all RM sample replicates. The significance cutoff (FDR<0.05) for each statistic is marked by
 1428 the red dashed line and was calculated from a background of 1000 permutations of the data.
 1429

- 1430 (B) Network of all significantly proportional (FDR<0.01) cell clusters across all RM replicate
1431 samples. Nodes are colored by cell type and edge weight is representative of proportionality.
- 1432 (C) Abundance plot of *Cd103*⁺ DCs, *Gp2+Lyz2*⁺ Gob/Sec cells, and *Dusp2+Icam1*⁺ Mature
1433 Neutrophils in replicate RM samples. Smoothed lines are calculated using local polynomial
1434 regression fitting.
- 1435 (D) Heatmap depicting a subset of differentially expressed receptor-ligand interaction pairs
1436 between single-cell pairs identified by NICHES (Raredon et al., 2023) for the clusters
1437 depicted in (C); ; see **Supplementary Table 2**. Interaction expression is the multiplicative
1438 expression of receptor and ligand gene expression for each member of a single-cell pair.
1439

Figure S9



1441 **Figure S9: Validating label transfer methods to assign cell cluster identities to new nasal**
1442 **mucosa samples**

1443 One sample replicate per timepoint was separated from the RM dataset to be used as a query
1444 trained using a reference made from the remaining sample replicates and unclassified cells.

1445 The left and right side depict results from Seurat and scANVI respectively.

1446 (A) Heatmaps depicting the per-cluster on-target prediction frequency when calculated across
1447 all 127 cluster labels.

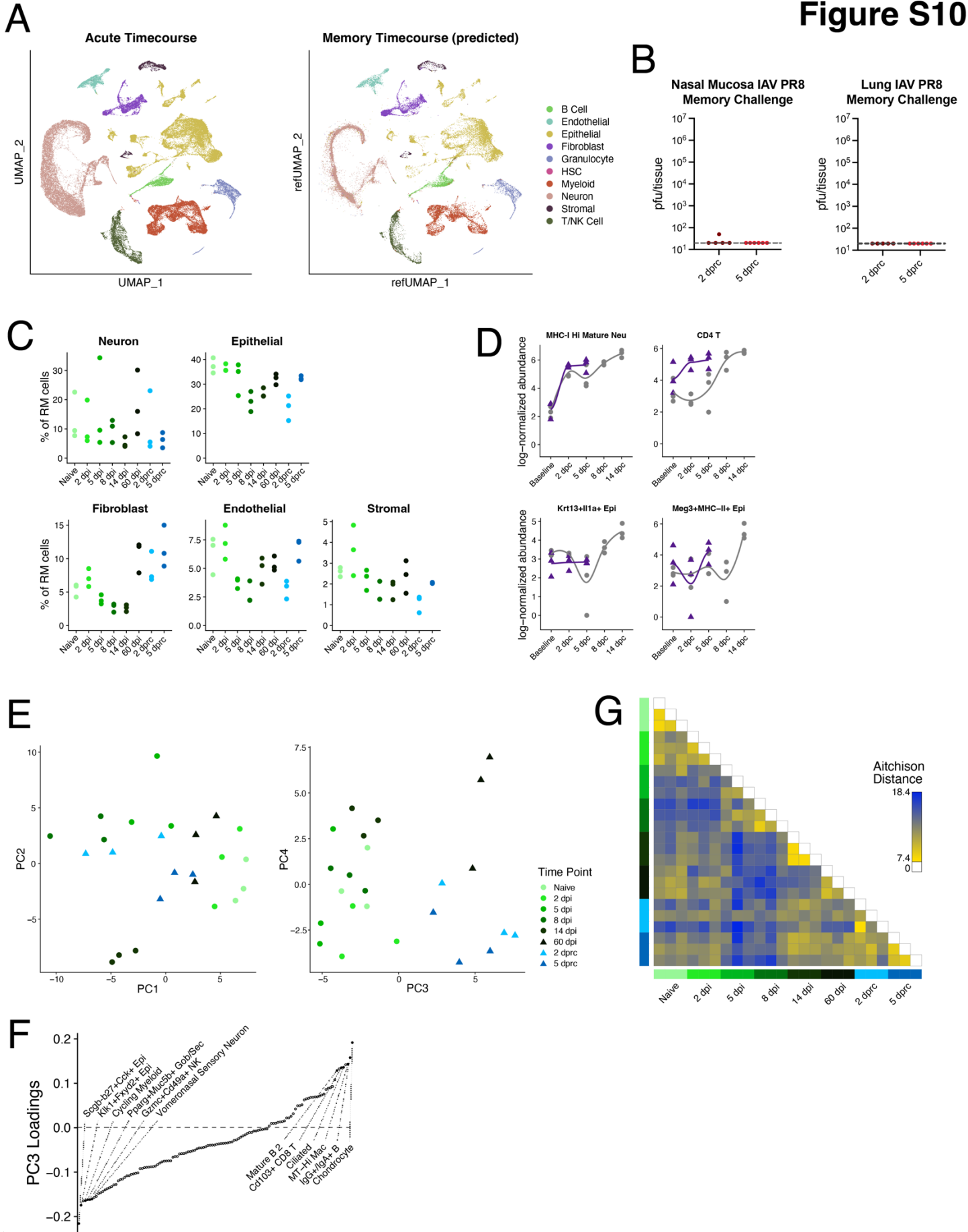
1448 (B) Heatmaps depicting the per-cell-type on-target prediction frequency when calculated across
1449 the 9 cell type labels.

1450 (C) After predicting cell type labels, new query and reference pairs were generated within each
1451 cell type and label transfer was performed within each. Heatmaps depicting the per-cluster
1452 on-target prediction frequency when calculated within all clusters within each respective cell
1453 type.

1454 (D) Compositional PCA from **Figure 2F** where the query sample replicates were projected using
1455 the predicted cell cluster labels.

1456

Figure S10



1458 **Figure S10: Changes in RM composition following secondary challenge**

1459 (A) UMAP of all RM cells from the primary infection dataset (left) and the projected UMAP of all
1460 cells in the rechallenge dataset (right) colored by cell type.

1461 (B) Infectious IAV PR8 quantification in pfu of the entire nasal mucosa (left) and lung (right)
1462 during IAV rechallenge.

1463 (C) Relative frequencies of non-immune cell types as a proportion of all sequenced cells per RM
1464 replicate sample in primary infection and following rechallenge.

1465 (D) Abundance plots of various clusters showing overlaid primary infection (gray) and
1466 rechallenge (purple) responses. Baseline refers to samples from naïve mice in primary
1467 infection and to samples from 60 dpi in rechallenge. dpc = days post challenge. Smoothed
1468 lines are calculated using local polynomial regression fitting.

1469 (E) Compositional PCA recalculated using both primary infection and secondary challenge RM
1470 sample replicates. PCs 1-2 (left) and 3-4 (right).

1471 (F) Cell cluster abundance loadings for PC3 (E). Cell cluster names for several of the most
1472 negative and most positive weights for each PC are depicted.

1473 (G) Heatmap depicting all pairwise Aitchison distances between all RM sample replicates.

1474

1475 **Supplementary Table 1: Differentially expressed genes across clusters within each cell**
1476 **type.** Differential expression analysis was performed across cells from all samples within each
1477 cell type using the Wilcoxon Rank Sum test.

1478

1479 **Supplementary Table 2: Differentially expressed receptor-ligand pairs identified by**
1480 **NICHES.** Within each NICHES analysis, differential expression was performed across all cell-
1481 pairs at the specific timepoint of interest using the ROC test built into Seurat. See **Figure 6**.

1482

1483 **Supplementary Table 3: Differentially expressed genes between primary infection and**
1484 **secondary challenge.** Differential expression analysis (“bidomal” test) was performed between
1485 timepoints using cells from RM only within the specified clusters in **Figure 7E**.

1486

1487 **REFERENCES**

- 1488 Adamson, M. S., Nesic, S., Bunes, A., Bayrak, K., Schmitz, S., Soler, S., Zillinger, T., Marx, S.,
1489 Lambing, S., Andryka-Cegielski, K., et al. (2022). RIG-I activation primes and trains
1490 innate antiviral immune memory. 2022.10.27.514004.
- 1491 Aegerter, H., Kulikauskaite, J., Crotta, S., Patel, H., Kelly, G., Hessel, E. M., Mack, M., Beinke,
1492 S. and Wack, A. (2020). Influenza-induced monocyte-derived alveolar macrophages
1493 confer prolonged antibacterial protection. *Nat Immunol* 21, 145–157.
- 1494 Aitchison, J., Barceló-Vidal, C., Martín-Fernández, J. A. and Pawlowsky-Glahn, V. (2000).
1495 Logratio Analysis and Compositional Distance. *Mathematical Geology* 32, 271–275.
- 1496 Angerer, P., Haghverdi, L., Büttner, M., Theis, F. J., Marr, C. and Buettner, F. (2016). destiny:
1497 diffusion maps for large-scale single-cell data in R. *Bioinformatics* 32, 1241–1243.
- 1498 Ariotti, S., Hogenbirk, M. A., Dijkgraaf, F. E., Visser, L. L., Hoekstra, M. E., Song, J.-Y., Jacobs,
1499 H., Haanen, J. B. and Schumacher, T. N. (2014). Skin-resident memory CD8+ T cells
1500 trigger a state of tissue-wide pathogen alert. *Science* 346, 101–105.
- 1501 Bastard, P., Rosen, L. B., Zhang, Q., Michailidis, E., Hoffmann, H.-H., Zhang, Y., Dorgham, K.,
1502 Philippot, Q., Rosain, J., Béziat, V., et al. (2020). Autoantibodies against type I IFNs in
1503 patients with life-threatening COVID-19. *Science* 370,.
- 1504 Bastard, P., Zhang, Q., Zhang, S.-Y., Jouanguy, E. and Casanova, J.-L. (2022). Type I
1505 interferons and SARS-CoV-2: from cells to organisms. *Current Opinion in Immunology*
1506 74, 172–182.
- 1507 Bosch, A. A. T. M., Biesbroek, G., Trzcinski, K., Sanders, E. A. M. and Bogaert, D. (2013). Viral
1508 and Bacterial Interactions in the Upper Respiratory Tract. *PLOS Pathogens* 9,
1509 e1003057.
- 1510 Bosch-Camós, L., Alonso, U., Esteve-Codina, A., Chang, C.-Y., Martín-Mur, B., Accensi, F.,
1511 Muñoz, M., Navas, M. J., Dabad, M., Vidal, E., et al. (2022). Cross-protection against
1512 African swine fever virus upon intranasal vaccination is associated with an adaptive-
1513 innate immune crosstalk. *PLOS Pathogens* 18, e1010931.
- 1514 Boudreau, C. M. and Alter, G. (2019). Extra-Neutralizing FcR-Mediated Antibody Functions for a
1515 Universal Influenza Vaccine. *Frontiers in Immunology* 10,.
- 1516 Bouvier, N. M. and Lowen, A. C. (2010). Animal Models for Influenza Virus Pathogenesis and
1517 Transmission. *Viruses* 2, 1530–1563.
- 1518 Boyd, D. F., Allen, E. K., Randolph, A. G., Guo, X. J., Weng, Y., Sanders, C. J., Bajracharya, R.,
1519 Lee, N. K., Guy, C. S., Vogel, P., et al. (2020). Exuberant fibroblast activity compromises
1520 lung function via ADAMTS4. *Nature* 587, 466–471.
- 1521 Brandes, M., Klauschen, F., Kuchen, S. and Germain, R. N. (2013). A Systems Analysis
1522 Identifies a Feedforward Inflammatory Circuit Leading to Lethal Influenza Infection. *Cell*
1523 154, 197–212.

- 1524 Brann, D. H., Tsukahara, T., Weinreb, C., Lipovsek, M., Van den Berge, K., Gong, B., Chance,
1525 R., Macaulay, I. C., Chou, H.-J., Fletcher, R. B., et al. (2020). Non-neuronal expression
1526 of SARS-CoV-2 entry genes in the olfactory system suggests mechanisms underlying
1527 COVID-19-associated anosmia. *Science Advances* 6, eabc5801.
- 1528 Broggi, A., Ghosh, S., Sposito, B., Spreafico, R., Balzarini, F., Cascio, A. L., Clementi, N.,
1529 Santis, M. D., Mancini, N., Granucci, F., et al. (2020). Type III interferons disrupt the lung
1530 epithelial barrier upon viral recognition. *Science* 369, 706–712.
- 1531 Büttner, M., Ostner, J., Müller, C. L., Theis, F. J. and Schubert, B. (2021). scCODA is a
1532 Bayesian model for compositional single-cell data analysis. *Nat Commun* 12, 6876.
- 1533 Cao, Y., Lin, Y., Ormerod, J. T., Yang, P., Yang, J. Y. H. and Lo, K. K. (2019). scDC: single cell
1534 differential composition analysis. *BMC Bioinformatics* 20, 721.
- 1535 Chapman, T. J. and Topham, D. J. (2010). Identification of a Unique Population of Tissue-
1536 Memory CD4+ T Cells in the Airways after Influenza Infection That Is Dependent on the
1537 Integrin VLA-1. *The Journal of Immunology* 184, 3841–3849.
- 1538 Chen, X., Liu, S., Goraya, M. U., Maarouf, M., Huang, S. and Chen, J.-L. (2018). Host Immune
1539 Response to Influenza A Virus Infection. *Front Immunol* 9, 320.
- 1540 Chen, K., Zhang, J., Huang, Y., Tian, X., Yang, Y. and Dong, A. (2022). Single-cell RNA-seq
1541 transcriptomic landscape of human and mouse islets and pathological alterations of
1542 diabetes. *iScience* 25, 105366.
- 1543 Clark, S. E. (2020). Commensal bacteria in the upper respiratory tract regulate susceptibility to
1544 infection. *Current Opinion in Immunology* 66, 42–49.
- 1545 Clark, R. A., Chong, B., Mirchandani, N., Brinster, N. K., Yamanaka, K., Dowgiert, R. K. and
1546 Kupper, T. S. (2006). The Vast Majority of CLA+ T Cells Are Resident in Normal Skin1.
1547 *The Journal of Immunology* 176, 4431–4439.
- 1548 Costa-Martins, A. G., Mane, K., Lindsey, B. B., Ogawa, R. L. T., Castro, Í., Jagne, Y. J., Sallah,
1549 H. J., Armitage, E. P., Jarju, S., Ahadzie, B., et al. (2021). Prior upregulation of interferon
1550 pathways in the nasopharynx impacts viral shedding following live attenuated influenza
1551 vaccine challenge in children. *Cell Reports Medicine* 2, 100465.
- 1552 Crowl, J. T., Heeg, M., Ferry, A., Milner, J. J., Omilusik, K. D., Toma, C., He, Z., Chang, J. T.
1553 and Goldrath, A. W. (2022). Tissue-resident memory CD8+ T cells possess unique
1554 transcriptional, epigenetic and functional adaptations to different tissue environments.
1555 *Nat Immunol* 23, 1121–1131.
- 1556 Dann, E., Henderson, N. C., Teichmann, S. A., Morgan, M. D. and Marioni, J. C. (2022).
1557 Differential abundance testing on single-cell data using k-nearest neighbor graphs. *Nat*
1558 *Biotechnol* 40, 245–253.
- 1559 Darrah, P. A., Zeppa, J. J., Maiello, P., Hackney, J. A., Wadsworth, M. H., Hughes, T. K.,
1560 Pokkali, S., Swanson, P. A., Grant, N. L., Rodgers, M. A., et al. (2020). Prevention of
1561 tuberculosis in macaques after intravenous BCG immunization. *Nature* 577, 95–102.

- 1562 Davis, J. D. and Wypych, T. P. (2021). Cellular and functional heterogeneity of the airway
1563 epithelium. *Mucosal Immunol* 14, 978–990.
- 1564 Denning, N.-L., Aziz, M., Murao, A., Gurien, S. D., Ochani, M., Prince, J. M. and Wang, P.
1565 (2020). Extracellular CIRP as an endogenous TREM-1 ligand to fuel inflammation in
1566 sepsis. *JCI Insight* 5,.
- 1567 Dumm, R. E., Wellford, S. A., Moseman, E. A. and Heaton, N. S. (2020). Heterogeneity of
1568 Antiviral Responses in the Upper Respiratory Tract Mediates Differential Non-lytic
1569 Clearance of Influenza Viruses. *Cell Reports* 32,.
- 1570 Fleming, S. J., Chaffin, M. D., Arduini, A., Akkad, A.-D., Banks, E., Marioni, J. C., Philippakis, A.
1571 A., Ellinor, P. T. and Babadi, M. (2022). Unsupervised removal of systematic background
1572 noise from droplet-based single-cell experiments using CellBender. 791699.
- 1573 Gardai, S. J., Xiao, Y.-Q., Dickinson, M., Nick, J. A., Voelker, D. R., Greene, K. E. and Henson,
1574 P. M. (2003). By Binding SIRP α or Calreticulin/CD91, Lung Collectins Act as Dual
1575 Function Surveillance Molecules to Suppress or Enhance Inflammation. *Cell* 115, 13–23.
- 1576 Gloor, G. B., Macklaim, J. M., Pawlowsky-Glahn, V. and Egozcue, J. J. (2017). Microbiome
1577 Datasets Are Compositional: And This Is Not Optional. *Frontiers in Microbiology* 8,.
- 1578 Grieshaber-Bouyer, R., Radtke, F. A., Cunin, P., Stifano, G., Levescot, A., Vijaykumar, B.,
1579 Nelson-Maney, N., Blaustein, R. B., Monach, P. A. and Nigrovic, P. A. (2021). The
1580 neutrotime transcriptional signature defines a single continuum of neutrophils across
1581 biological compartments. *Nat Commun* 12, 2856.
- 1582 Habibi, M. S., Thwaites, R. S., Chang, M., Jozwik, A., Paras, A., Kirsebom, F., Varese, A.,
1583 Owen, A., Cuthbertson, L., James, P., et al. (2020). Neutrophilic inflammation in the
1584 respiratory mucosa predisposes to RSV infection. *Science* 370,.
- 1585 Hao, Y., Hao, S., Andersen-Nissen, E., Mauck, W. M., Zheng, S., Butler, A., Lee, M. J., Wilk, A.
1586 J., Darby, C., Zager, M., et al. (2021). Integrated analysis of multimodal single-cell data.
1587 *Cell* 184, 3573-3587.e29.
- 1588 Harkema, J. R., Carey, S. A. and Wagner, J. G. (2006). The Nose Revisited: A Brief Review of
1589 the Comparative Structure, Function, and Toxicologic Pathology of the Nasal Epithelium.
1590 *Toxicol Pathol* 34, 252–269.
- 1591 Hartwell, B. L., Melo, M. B., Xiao, P., Lemnios, A. A., Li, N., Chang, J. Y. H., Yu, J., Gebre, M.
1592 S., Chang, A., Maiorino, L., et al. (2022). Intranasal vaccination with lipid-conjugated
1593 immunogens promotes antigen transmucosal uptake to drive mucosal and systemic
1594 immunity. *Science Translational Medicine* 14, eabn1413.
- 1595 Hu, M.-W., Kim, D. W., Liu, S., Zack, D. J., Blackshaw, S. and Qian, J. (2019). PanoView: An
1596 iterative clustering method for single-cell RNA sequencing data. *PLOS Computational*
1597 *Biology* 15, e1007040.
- 1598 Hufford, M. M., Kim, T. S., Sun, J. and Braciale, T. J. (2015). The Effector T Cell Response to
1599 Influenza Infection. In *Influenza Pathogenesis and Control - Volume II* (ed. Oldstone, M.
1600 B. A.) and Compans, R. W.), pp. 423–455. Cham: Springer International Publishing.

- 1601 Ibricevic, A., Pekosz, A., Walter, M. J., Newby, C., Battaile, J. T., Brown, E. G., Holtzman, M. J.
1602 and Brody, S. L. (2006). Influenza Virus Receptor Specificity and Cell Tropism in Mouse
1603 and Human Airway Epithelial Cells. *Journal of Virology* 80, 7469–7480.
- 1604 Iuliano, A. D., Roguski, K. M., Chang, H. H., Muscatello, D. J., Palekar, R., Tempia, S., Cohen,
1605 C., Gran, J. M., Schanzer, D., Cowling, B. J., et al. (2018). Estimates of global seasonal
1606 influenza-associated respiratory mortality: a modelling study. *Lancet* 391, 1285–1300.
- 1607 Iwasaki, A. and Medzhitov, R. (2015). Control of adaptive immunity by the innate immune
1608 system. *Nat. Immunol.* 16, 343–353.
- 1609 Jiang, X., Clark, R. A., Liu, L., Wagers, A. J., Fuhlbrigge, R. C. and Kupper, T. S. (2012). Skin
1610 infection generates non-migratory memory CD8+ TRM cells providing global skin
1611 immunity. *Nature* 483, 227–231.
- 1612 Johansson, C. and Kirsebom, F. C. M. (2021). Neutrophils in respiratory viral infections.
1613 *Mucosal Immunol* 14, 815–827.
- 1614 Johnson, P. R., Feldman, S., Thompson, J. M., Mahoney, J. D. and Wright, P. F. (1986).
1615 Immunity to Influenza A Virus Infection in Young Children: A Comparison of Natural
1616 Infection, Live Cold-Adapted Vaccine, and Inactivated Vaccine. *The Journal of Infectious
1617 Diseases* 154, 121–127.
- 1618 Johnson Jr., P. R., Feldman, S., Thompson, J. M., Mahoney, J. D. and Wright, P. F. (1985).
1619 Comparison of long-term systemic and secretory antibody responses in children given
1620 live, attenuated, or inactivated influenza A vaccine. *Journal of Medical Virology* 17, 325–
1621 335.
- 1622 Jung, S.-H., Hwang, B.-H., Shin, S., Park, E.-H., Park, S.-H., Kim, C. W., Kim, E., Choo, E.,
1623 Choi, I. J., Swirski, F. K., et al. (2022). Spatiotemporal dynamics of macrophage
1624 heterogeneity and a potential function of Trem2hi macrophages in infarcted hearts. *Nat
1625 Commun* 13, 4580.
- 1626 Kadoki, M., Patil, A., Thaïss, C. C., Brooks, D. J., Pandey, S., Deep, D., Alvarez, D., Andrian, U.
1627 H. von, Wagers, A. J., Nakai, K., et al. (2017). Organism-Level Analysis of Vaccination
1628 Reveals Networks of Protection across Tissues. *Cell* 171, 398-413.e21.
- 1629 Kaufmann, E., Sanz, J., Dunn, J. L., Khan, N., Mendonça, L. E., Pacis, A., Tzelepis, F., Pernet,
1630 E., Dumaine, A., Grenier, J.-C., et al. (2018). BCG Educates Hematopoietic Stem Cells
1631 to Generate Protective Innate Immunity against Tuberculosis. *Cell* 172, 176-190.e19.
- 1632 Kim, Y.-M. and Shin, E.-C. (2021). Type I and III interferon responses in SARS-CoV-2 infection.
1633 *Exp Mol Med* 53, 750–760.
- 1634 Klinkhammer, J., Schnepf, D., Ye, L., Schwaderlapp, M., Gad, H. H., Hartmann, R., Garcin, D.,
1635 Mahlaköiv, T. and Staeheli, P. (2018). IFN- λ prevents influenza virus spread from the
1636 upper airways to the lungs and limits virus transmission. *eLife* 7, e33354.
- 1637 Kochs, G., García-Sastre, A. and Martínez-Sobrido, L. (2007). Multiple Anti-Interferon Actions of
1638 the Influenza A Virus NS1 Protein. *J Virol* 81, 7011–7021.

- 1639 Krammer, F. (2019). The human antibody response to influenza A virus infection and
1640 vaccination. *Nat Rev Immunol* 19, 383–397.
- 1641 Lavelle, E. C. and Ward, R. W. (2022). Mucosal vaccines — fortifying the frontiers. *Nat Rev*
1642 *Immunol* 22, 236–250.
- 1643 Li, B., Gould, J., Yang, Y., Sarkizova, S., Tabaka, M., Ashenberg, O., Rosen, Y., Slyper, M.,
1644 Kowalczyk, M. S., Villani, A.-C., et al. (2020). Cumulus provides cloud-based data
1645 analysis for large-scale single-cell and single-nucleus RNA-seq. *Nat Methods* 17, 793–
1646 798.
- 1647 Li, H., Wang, X., Wang, Y., Zhang, M., Hong, F., Wang, H., Cui, A., Zhao, J., Ji, W. and Chen,
1648 Y.-G. (2022). Cross-species single-cell transcriptomic analysis reveals divergence of cell
1649 composition and functions in mammalian ileum epithelium. *Cell Regeneration* 11, 19.
- 1650 Liew, F., Talwar, S., Cross, A., Willett, B. J., Scott, S., Logan, N., Siggins, M. K., Swieboda, D.,
1651 Sidhu, J. K., Efstathiou, C., et al. (2023). SARS-CoV-2-specific nasal IgA wanes 9
1652 months after hospitalisation with COVID-19 and is not induced by subsequent
1653 vaccination. *eBioMedicine* 87,.
- 1654 Lin, H. and Peddada, S. D. (2020). Analysis of microbial compositions: a review of normalization
1655 and differential abundance analysis. *npj Biofilms Microbiomes* 6, 1–13.
- 1656 Linderman, G. C., Zhao, J., Roulis, M., Bielecki, P., Flavell, R. A., Nadler, B. and Kluger, Y.
1657 (2022). Zero-preserving imputation of single-cell RNA-seq data. *Nat Commun* 13, 192.
- 1658 Lovell, D., Pawlowsky-Glahn, V., Egozcue, J. J., Marguerat, S. and Bähler, J. (2015).
1659 Proportionality: A Valid Alternative to Correlation for Relative Data. *PLOS Computational*
1660 *Biology* 11, e1004075.
- 1661 Mack, M., Cihak, J., Simonis, C., Luckow, B., Proudfoot, A. E. I., Plachý, J., Brühl, H., Frink, M.,
1662 Anders, H.-J., Vielhauer, V., et al. (2001). Expression and Characterization of the
1663 Chemokine Receptors CCR2 and CCR5 in Mice¹. *The Journal of Immunology* 166,
1664 4697–4704.
- 1665 MacLean, A. J., Richmond, N., Koneva, L., Attar, M., Medina, C. A. P., Thornton, E. E., Gomes,
1666 A. C., El-Turabi, A., Bachmann, M. F., Rijal, P., et al. (2022). Secondary influenza
1667 challenge triggers resident memory B cell migration and rapid relocation to boost
1668 antibody secretion at infected sites. *Immunity* 55, 718-733.e8.
- 1669 Madhavan, M., Ritchie, A. J., Aboagye, J., Jenkin, D., Provstgaard-Morys, S., Tarbet, I., Woods,
1670 D., Davies, S., Baker, M., Platt, A., et al. (2022). Tolerability and immunogenicity of an
1671 intranasally-administered adenovirus-vectored COVID-19 vaccine: An open-label
1672 partially-randomised ascending dose phase I trial. *eBioMedicine* 85,.
- 1673 Major, J., Crotta, S., Llorian, M., McCabe, T. M., Gad, H. H., Priestnall, S. L., Hartmann, R. and
1674 Wack, A. (2020). Type I and III interferons disrupt lung epithelial repair during recovery
1675 from viral infection. *Science* 369, 712–717.

- 1676 Manicassamy, B., Manicassamy, S., Belicha-Villanueva, A., Pisanelli, G., Pulendran, B. and
1677 García-Sastre, A. (2010). Analysis of in vivo dynamics of influenza virus infection in mice
1678 using a GFP reporter virus. *PNAS* 107, 11531–11536.
- 1679 Mao, T., Israelow, B., Peña-Hernández, M. A., Suberi, A., Zhou, L., Luyten, S., Reschke, M.,
1680 Dong, H., Homer, R. J., Saltzman, W. M., et al. (2022). Unadjuvanted intranasal spike
1681 vaccine elicits protective mucosal immunity against sarbecoviruses. *Science* 378,
1682 eabo2523.
- 1683 Matsuoka, Y., Lamirande, E. W. and Subbarao, K. (2009). The mouse model for influenza. *Curr*
1684 *Protoc Microbiol* Chapter 15, Unit 15G.3.
- 1685 McMaster, S. R., Wilson, J. J., Wang, H. and Kohlmeier, J. E. (2015). Airway-Resident Memory
1686 CD8 T Cells Provide Antigen-Specific Protection against Respiratory Virus Challenge
1687 through Rapid IFN- γ Production. *The Journal of Immunology* 195, 203–209.
- 1688 Milner, J. J., Toma, C., Yu, B., Zhang, K., Omilusik, K., Phan, A. T., Wang, D., Getzler, A. J.,
1689 Nguyen, T., Crotty, S., et al. (2017). Runx3 programs CD8⁺ T cell residency in non-
1690 lymphoid tissues and tumours. *Nature* 552, 253–257.
- 1691 Montoro, D. T., Haber, A. L., Biton, M., Vinarsky, V., Lin, B., Birket, S. E., Yuan, F., Chen, S.,
1692 Leung, H. M., Villoria, J., et al. (2018). A revised airway epithelial hierarchy includes
1693 CFTR-expressing ionocytes. *Nature* 560, 319–324.
- 1694 Morens, D. M., Taubenberger, J. K. and Fauci, A. S. (2023). Rethinking next-generation
1695 vaccines for coronaviruses, influenzaviruses, and other respiratory viruses. *Cell Host &*
1696 *Microbe* 31, 146–157.
- 1697 Morgan, A. J., Guillen, C., Symon, F. A., Birring, S. S., Campbell, J. J. and Wardlaw, A. J.
1698 (2008). CXCR6 identifies a putative population of retained human lung T cells
1699 characterised by co-expression of activation markers. *Immunobiology* 213, 599–608.
- 1700 Moriyama, M., Chen, I.-Y., Kawaguchi, A., Koshiba, T., Nagata, K., Takeyama, H., Hasegawa,
1701 H. and Ichinohe, T. (2016). The RNA- and TRIM25-Binding Domains of Influenza Virus
1702 NS1 Protein Are Essential for Suppression of NLRP3 Inflammasome-Mediated
1703 Interleukin-1 β Secretion. *Journal of Virology* 90, 4105–4114.
- 1704 Nouën, C. L., Nelson, C. E., Liu, X., Park, H.-S., Matsuoka, Y., Luongo, C., Santos, C., Yang, L.,
1705 Herbert, R., Castens, A., et al. (2022). Intranasal pediatric parainfluenza virus-vectored
1706 SARS-CoV-2 vaccine is protective in monkeys. *Cell* 185, 4811-4825.e17.
- 1707 Ols, S., Yang, L., Thompson, E. A., Tran, K., Liang, F., Lin, A., Eriksson, B., Hedestam, G. B.
1708 K., Wyatt, R. T. and Loré, K. (2020). Route of Vaccine Administration Alters Antigen
1709 Trafficking but Not Innate or Adaptive Immunity. *Cell Reports* 30, 3964-3971.e7.
- 1710 Onodera, T., Takahashi, Y., Yokoi, Y., Ato, M., Kodama, Y., Hachimura, S., Kurosaki, T. and
1711 Kobayashi, K. (2012). Memory B cells in the lung participate in protective humoral
1712 immune responses to pulmonary influenza virus reinfection. *Proceedings of the National*
1713 *Academy of Sciences* 109, 2485–2490.

- 1714 Ordovas-Montanes, J., Dwyer, D. F., Nyquist, S. K., Buchheit, K. M., Vukovic, M., Deb, C.,
1715 Wadsworth, M. H., Hughes, T. K., Kazer, S. W., Yoshimoto, E., et al. (2018). Allergic
1716 inflammatory memory in human respiratory epithelial progenitor cells. *Nature* 560, 649.
- 1717 Ordovas-Montanes, J., Beyaz, S., Rakoff-Nahoum, S. and Shalek, A. K. (2020). Distribution and
1718 storage of inflammatory memory in barrier tissues. *Nat Rev Immunol* 1–13.
- 1719 Park, A. and Iwasaki, A. (2020). Type I and Type III Interferons – Induction, Signaling, Evasion,
1720 and Application to Combat COVID-19. *Cell Host Microbe* 27, 870–878.
- 1721 Patterson-Cross, R. B., Levine, A. J. and Menon, V. (2021). Selecting single cell clustering
1722 parameter values using subsampling-based robustness metrics. *BMC Bioinformatics* 22,
1723 39.
- 1724 Pizzolla, A., Nguyen, T. H. O., Smith, J. M., Brooks, A. G., Kedzierska, K., Heath, W. R.,
1725 Reading, P. C. and Wakim, L. M. (2017). Resident memory CD8+ T cells in the upper
1726 respiratory tract prevent pulmonary influenza virus infection. *Science Immunology* 2,.
- 1727 Quinn, T. P., Richardson, M. F., Lovell, D. and Crowley, T. M. (2017). propr: An R-package for
1728 Identifying Proportionally Abundant Features Using Compositional Data Analysis. *Sci*
1729 *Rep* 7, 16252.
- 1730 Quinn, T. P., Erb, I., Richardson, M. F. and Crowley, T. M. (2018). Understanding sequencing
1731 data as compositions: an outlook and review. *Bioinformatics* 34, 2870–2878.
- 1732 Raredon, M. S. B., Yang, J., Kothapalli, N., Lewis, W., Kaminski, N., Niklason, L. E. and Kluger,
1733 Y. (2023). Comprehensive visualization of cell–cell interactions in single-cell and spatial
1734 transcriptomics with NICHES. *Bioinformatics* 39, btac775.
- 1735 Ratnasiri, K., Wilk, A. J., Lee, M. J., Khatri, P. and Blish, C. A. (2023). Single-cell RNA-seq
1736 methods to interrogate virus-host interactions. *Semin Immunopathol* 45, 71–89.
- 1737 Rossen, R. D., Butler, W. T., Waldman, R. H., Alford, R. H., Hornick, R. B., Togo, Y. and Kasel,
1738 J. A. (1970). The Proteins in Nasal Secretion: II. A Longitudinal Study of IgA and
1739 Neutralizing Antibody Levels in Nasal Washings From Men Infected With Influenza
1740 Virus. *JAMA* 211, 1157–1161.
- 1741 Roth, G. A., Abate, D., Abate, K. H., Abay, S. M., Abbafati, C., Abbasi, N., Abbastabar, H., Abd-
1742 Allah, F., Abdela, J., Abdelalim, A., et al. (2018). Global, regional, and national age-sex-
1743 specific mortality for 282 causes of death in 195 countries and territories, 1980–2017: a
1744 systematic analysis for the Global Burden of Disease Study 2017. *The Lancet* 392,
1745 1736–1788.
- 1746 Russell, M. W., Moldoveanu, Z., Ogra, P. L. and Mestecky, J. (2020). Mucosal Immunity in
1747 COVID-19: A Neglected but Critical Aspect of SARS-CoV-2 Infection. *Frontiers in*
1748 *Immunology* 11,.
- 1749 Rutigliano, J. A., Morris, M. Y., Yue, W., Keating, R., Webby, R. J., Thomas, P. G. and Doherty,
1750 P. C. (2010). Protective Memory Responses Are Modulated by Priming Events prior to
1751 Challenge. *J Virol* 84, 1047–1056.

- 1752 Schenkel, J. M., Fraser, K. A., Beura, L. K., Pauken, K. E., Vezys, V. and Masopust, D. (2014).
1753 Resident memory CD8 T cells trigger protective innate and adaptive immune responses.
1754 *Science* 346, 98–101.
- 1755 Shinya, K., Ebina, M., Yamada, S., Ono, M., Kasai, N. and Kawaoka, Y. (2006). Influenza virus
1756 receptors in the human airway. *Nature* 440, 435–436.
- 1757 Slütter, B., Pewe, L. L., Kaech, S. M. and Harty, J. T. (2013). Lung Airway-Surveilling CXCR3hi
1758 Memory CD8+ T Cells Are Critical for Protection against Influenza A Virus. *Immunity* 39,
1759 939–948.
- 1760 Slütter, B., Van Braeckel-Budimir, N., Abboud, G., Varga, S. M., Salek-Ardakani, S. and Harty,
1761 J. T. (2017). Dynamics of influenza-induced lung-resident memory T cells underlie
1762 waning heterosubtypic immunity. *Science Immunology* 2, eaag2031.
- 1763 Smillie, C. S., Biton, M., Ordovas-Montanes, J., Sullivan, K. M., Burgin, G., Graham, D. B.,
1764 Herbst, R. H., Rogel, N., Slyper, M., Waldman, J., et al. (2019). Intra- and Inter-cellular
1765 Rewiring of the Human Colon during Ulcerative Colitis. *Cell* 178, 714-730.e22.
- 1766 Sposito, B., Broggi, A., Pandolfi, L., Crotta, S., Clementi, N., Ferrarese, R., Sisti, S., Criscuolo,
1767 E., Spreafico, R., Long, J. M., et al. (2021). The interferon landscape along the
1768 respiratory tract impacts the severity of COVID-19. *Cell* 184, 4953-4968.e16.
- 1769 Strydom, G., Olive, A., Radovic-Moreno, A. F., Gondek, D., Alvarez, D., Basto, P. A., Perro, M.,
1770 Vrbancic, V. D., Tager, A. M., Shi, J., et al. (2015). VACCINES. A mucosal vaccine
1771 against *Chlamydia trachomatis* generates two waves of protective memory T cells.
1772 *Science* 348, aaa8205.
- 1773 Steinbach, K., Vincenti, I., Kreutzfeldt, M., Page, N., Muschaweckh, A., Wagner, I., Drexler, I.,
1774 Pinschewer, D., Korn, T. and Merkler, D. (2016). Brain-resident memory T cells
1775 represent an autonomous cytotoxic barrier to viral infection. *Journal of Experimental*
1776 *Medicine* 213, 1571–1587.
- 1777 Sterlin, D., Mathian, A., Miyara, M., Mohr, A., Anna, F., Claër, L., Quentric, P., Fadlallah, J.,
1778 Devilliers, H., Ghillani, P., et al. (2021). IgA dominates the early neutralizing antibody
1779 response to SARS-CoV-2. *Science Translational Medicine* 13, eabd2223.
- 1780 Steuerman, Y., Cohen, M., Peshes-Yaloz, N., Valadarsky, L., Cohn, O., David, E., Frishberg, A.,
1781 Mayo, L., Bacharach, E., Amit, I., et al. (2018). Dissection of Influenza Infection In Vivo
1782 by Single-Cell RNA Sequencing. *Cell Syst* 6, 679-691.e4.
- 1783 Takaba, H., Morishita, Y., Tomofuji, Y., Danks, L., Nitta, T., Komatsu, N., Kodama, T. and
1784 Takayanagi, H. (2015). Fezf2 Orchestrates a Thymic Program of Self-Antigen
1785 Expression for Immune Tolerance. *Cell* 163, 975–987.
- 1786 Tang, B. M., Shojaei, M., Teoh, S., Meyers, A., Ho, J., Ball, T. B., Keynan, Y., Pisipati, A.,
1787 Kumar, A., Eisen, D. P., et al. (2019). Neutrophils-related host factors associated with
1788 severe disease and fatality in patients with influenza infection. *Nat Commun* 10, 3422.

- 1789 Trombetta, J. J., Gennert, D., Lu, D., Satija, R., Shalek, A. K. and Regev, A. (2014). Preparation
1790 of Single-Cell RNA-Seq Libraries for Next Generation Sequencing. *Current Protocols in*
1791 *Molecular Biology* 107,.
- 1792 Tse, S.-W., Radtke, A. J., Espinosa, D. A., Cockburn, I. A. and Zavala, F. (2014). The
1793 Chemokine Receptor CXCR6 Is Required for the Maintenance of Liver Memory CD8+ T
1794 Cells Specific for Infectious Pathogens. *The Journal of Infectious Diseases* 210, 1508–
1795 1516.
- 1796 Türei, D., Korcsmáros, T. and Saez-Rodriguez, J. (2016). OmniPath: guidelines and gateway for
1797 literature-curated signaling pathway resources. *Nat Methods* 13, 966–967.
- 1798 Ualiyeva, S., Lemire, E., Boyd, A., Wong, C., Avilés, E. C., Maxfield, A., Roditi, R., Matsumoto,
1799 I., Barrett, N. A., Buchheit, K. M., et al. (2022). Olfactory microvillar tuft cells direct
1800 neurogenesis during allergic inflammation. 2022.09.26.509561.
- 1801 Vaca, G. B., Meyer, M., Cadete, A., Hsiao, C. J., Golding, A., Jeon, A., Jacquinet, E., Azcue, E.,
1802 Guan, C. M., Sanchez-Felix, X., et al. (2023). Intranasal mRNA-LNP vaccination protects
1803 hamsters from SARS-CoV-2 infection. 2023.01.11.523616.
- 1804 Wein, A. N., McMaster, S. R., Takamura, S., Dunbar, P. R., Cartwright, E. K., Hayward, S. L.,
1805 McManus, D. T., Shimaoka, T., Ueha, S., Tsukui, T., et al. (2019). CXCR6 regulates
1806 localization of tissue-resident memory CD8 T cells to the airways. *Journal of*
1807 *Experimental Medicine* 216, 2748–2762.
- 1808 Weisberg, S. P., Ural, B. B. and Farber, D. L. (2021). Tissue-specific immunity for a changing
1809 world. *Cell* 184, 1517–1529.
- 1810 Wellford, S. A., Moseman, A. P., Dao, K., Wright, K. E., Chen, A., Plevin, J. E., Liao, T.-C.,
1811 Mehta, N. and Moseman, E. A. (2022). Mucosal plasma cells are required to protect the
1812 upper airway and brain from infection. *Immunity* 55, 2118-2134.e6.
- 1813 Weltzin, R., Traina-Dorge, V., Soike, K., Zhang, J.-Y., Mack, P., Soman, G., Drabik, G. and
1814 Monath, T. P. (1996). Intranasal Monoclonal IgA Antibody to Respiratory Syncytial Virus
1815 Protects Rhesus Monkeys against Upper and Lower Respiratory Tract Infection. *The*
1816 *Journal of Infectious Diseases* 174, 256–261.
- 1817 Wickenhagen, A., Sugrue, E., Lytras, S., Kuchi, S., Noerenberg, M., Turnbull, M. L., Loney, C.,
1818 Herder, V., Allan, J., Jarmson, I., et al. (2021). A prenylated dsRNA sensor protects
1819 against severe COVID-19. *Science* 374, eabj3624.
- 1820 Wiley, J. A., Hogan, R. J., Woodland, D. L. and Harmsen, A. G. (2001). Antigen-Specific CD8+
1821 T Cells Persist in the Upper Respiratory Tract Following Influenza Virus Infection. *J*
1822 *Immunol* 167, 3293–3299.
- 1823 Woof, J. M. and Mestecky, J. (2005). Mucosal immunoglobulins. *Immunological Reviews* 206,
1824 64–82.
- 1825 Xie, X., Shi, Q., Wu, P., Zhang, X., Kambara, H., Su, J., Yu, H., Park, S.-Y., Guo, R., Ren, Q., et
1826 al. (2020). Single-cell transcriptome profiling reveals neutrophil heterogeneity in
1827 homeostasis and infection. *Nat Immunol* 21, 1119–1133.

- 1828 Xu, C., Lopez, R., Mehlman, E., Regier, J., Jordan, M. I. and Yosef, N. (2021). Probabilistic
1829 harmonization and annotation of single-cell transcriptomics data with deep generative
1830 models. *Molecular Systems Biology* 17, e9620.
- 1831 Yao, Y., Jeyanathan, M., Haddadi, S., Barra, N. G., Vaseghi-Shanjani, M., Damjanovic, D., Lai,
1832 R., Afkhami, S., Chen, Y., Dvorkin-Gheva, A., et al. (2018). Induction of Autonomous
1833 Memory Alveolar Macrophages Requires T Cell Help and Is Critical to Trained Immunity.
1834 *Cell* 175, 1634-1650.e17.
- 1835 Zaretsky, A. G., Engiles, J. B. and Hunter, C. A. (2014). Infection-Induced Changes in
1836 Hematopoiesis. *The Journal of Immunology* 192, 27–33.
- 1837 Zhang, Q., Bastard, P., Liu, Z., Pen, J. L., Moncada-Velez, M., Chen, J., Ogishi, M., Sabli, I. K.
1838 D., Hodeib, S., Korol, C., et al. (2020). Inborn errors of type I IFN immunity in patients
1839 with life-threatening COVID-19. *Science* 370,.
- 1840 Zhang, H., Alford, T., Liu, S., Zhou, D. and Wang, J. (2022a). Influenza virus causes lung
1841 immunopathology through down-regulating PPAR γ activity in macrophages. *Frontiers in*
1842 *Immunology* 13,.
- 1843 Zhang, K., Erkan, E. P., Jamalzadeh, S., Dai, J., Andersson, N., Kaipio, K., Lamminen, T.,
1844 Mansuri, N., Huhtinen, K., Carpén, O., et al. (2022b). Longitudinal single-cell RNA-seq
1845 analysis reveals stress-promoted chemoresistance in metastatic ovarian cancer.
1846 *Science Advances* 8, eabm1831.
- 1847 Zheng, H. B., Doran, B. A., Kimler, K., Yu, A., Tkachev, V., Niederlova, V., Cribbin, K., Fleming,
1848 R., Bratrude, B., Betz, K., et al. (2021). A Treatment-Naïve Cellular Atlas of Pediatric
1849 Crohn's Disease Predicts Disease Severity and Therapeutic Response.
1850 2021.09.17.21263540.
- 1851 Ziegler, C. G. K., Miao, V. N., Owings, A. H., Navia, A. W., Tang, Y., Bromley, J. D., Lotfy, P.,
1852 Sloan, M., Laird, H., Williams, H. B., et al. (2021). Impaired local intrinsic immunity to
1853 SARS-CoV-2 infection in severe COVID-19. *Cell* 184, 4713-4733.e22.
- 1854